

Clemson University

TigerPrints

All Theses

Theses

5-2024

Analytical and Experimental Studies to Support Codification of Lightweight Grout for Masonry Design

Cooper Banks
crbanks@clemson.edu

Follow this and additional works at: https://tigerprints.clemson.edu/all_theses



Part of the [Civil Engineering Commons](#), and the [Structural Engineering Commons](#)

Recommended Citation

Banks, Cooper, "Analytical and Experimental Studies to Support Codification of Lightweight Grout for Masonry Design" (2024). *All Theses*. 4264.

https://tigerprints.clemson.edu/all_theses/4264

This Thesis is brought to you for free and open access by the Theses at TigerPrints. It has been accepted for inclusion in All Theses by an authorized administrator of TigerPrints. For more information, please contact kokeefe@clemson.edu.

ANALYTICAL AND EXPERIMENTAL STUDIES TO SUPPORT CODIFICATION OF
LIGHTWEIGHT GROUT FOR MASONRY DESIGN

A Thesis
Presented to
the Graduate School of
Clemson University

In Partial Fulfillment
of the Requirements for the Degree
Master of Science
Civil Engineering

by
Cooper Banks
May 2024

Accepted by:
Dr. Laura Redmond, Committee Chair
Dr. Thomas Cousins
Dr. Brandon Ross

ABSTRACT

Lightweight (LW) aggregates have many potential benefits in masonry construction including minimizing mass, improving thermal performance, and reducing the potential for shrinkage cracking via internal curing. The current masonry design standard, TMS 402/602-22, permits lightweight aggregate in the production of concrete masonry units (CMU), but there has been insufficient testing of masonry assemblies to permit designing with LW grout. Shrestha et al. characterized LW grouts bond to reinforcement, shear strength, tension and shear pullout behavior of anchors and proposed possible reduction factors for design. Hiner characterized the flexural bond strength LW grouted masonry assemblies and proposed possible reduction factors for design. In currently unpublished work Kessler worked to proposed reduction factors for the shear and cohesion behavior of masonry assemblies. This work confirms the studies of Kessler and expands on the testing conducted by Hiner. Along with that this work uses the proposed reduction factors of previous work and displays a cost analysis of NW versus LW design under seismic loading.

DEDICATION

This work is dedicated to my biggest supporters in life, Mom, Dad, and Charlie.

ACKNOWLEDGMENTS

I would like to thank my advisor, Dr. Laura Redmond for trusting me with this project. She has displayed great faith in my abilities, which has provided me with great confidence and has calmed my anxious mind many times.

I would also like to thank Rumi Shrestha, Ben Hiner, and Dylan Smith for the countless hours teaching and working with me in the lab.

TABLE OF CONTENTS

	Page
TITLE PAGE	i
ABSTRACT	ii
DEDICATION	iii
ACKNOWLEDGMENTS	iv
LIST OF TABLES	vii
LIST OF FIGURES	ix
CHAPTER	
I. INTRODUCTION	1
Motivation and Research Overview.....	1
Summary of Current Literature and Identified Gaps	1
Summary of Research Objectives	2
Outline of Thesis	2
II. LITERATURE REVIEW	4
III. FINITE ELEMENT MODELING	7
Introduction.....	7
Element Formulation	8
Material Calibration	19
Model Validation	29
Summary	43
IV. TRIPLET TESTS	45
Statement of Contribution.....	45
Introduction.....	45
Experimental Program	49
Results	58
Recommendations for Design.....	76
Conclusion	77
Acknowledgments.....	78

V.	BOND WRENCH TESTS	79
	Statement of Contribution.....	79
	Introduction.....	79
	Design of the Moment Couple Device.....	84
	Material Properties.....	90
	Preparation of the Masonry Prisms.....	94
	Test Procedure	96
	Test Results and Discussion.....	97
	Conclusion	108
	Acknowledgments.....	109
VI.	COST BENEFITS OF LIGHTWEIGHT GROUT	110
	Statement of Contribution.....	110
	Introduction.....	110
	Wall Design Procedure	110
	Cost Estimation Procedure.....	115
	Results.....	115
	Conclusion	118
VII.	SUMMARY AND CONCLUSIONS	119
	REFERENCES	121
	APPENDICES	127
	A: Cost Comparison Calculations.....	128

LIST OF TABLES

Table	Page
3.1 Stiffness variable references	26
3.2 Shear Modulus Comparison.....	43
3.3 Peak Load Comparison	43
4.1 Grout type, number of specimens tested, normal compression stress, and average shear strength of specimens from Hamid et al. [52]	47
4.2 Normal compression stress, number of specimens, and average shear strength of shear triplets tested by Redmond et al. [53].....	48
4.3 Density properties, specific gravity, absorption, and gradation of the EC coarse and fine aggregates and ES coarse and fine aggregates.....	50
4.4 The as-batched volume proportions, water-to-cement ratios by weight, and slumps of the three mix designs	52
4.5 Number of specimens tested, average 28-day grout compressive strength, and standard deviation for each mix design.....	53
4.6 Number of specimens tested, average 28-day mortar compressive strength, and standard deviation for each batch of mortar	54
4.7 Shear triplet specimens, their normal compression stress values, and their failure modes.	60
4.8 Normal stress vs. shear stress at failure and relevant specimen properties for each of the EC, ES-1, and ES-2 specimens	62
4.9 Element properties used in analysis.....	71

List of Tables (Continued)

Table	Page
4.10 Proposed reduction factors for shear strength of grouted masonry bed joints.	76
5.1 Masonry Self Weight (SW), Dimensions, and Other Dead Weight from Test Device.....	90
5.2 Aggregate Properties.....	91
5.3 Mix Design for Grout Batches.....	93
5.4 Compression Test Results.....	93
5.5 Results of Flexural Bond Strength Tests	99
5.6 Tested Strength vs. Predicted Strengths.....	101
5.7 Normal-Weight Grout Test Results	104
5.8 Values of λ for lightweight concrete based on equilibrium density from ACI 318-19	107
5.9 Lightweight Grout Equilibrium Densities	108
6.1 Design values for a single grout type and SDC	112
6.2 Reduction Factor Equations.....	114

LIST OF FIGURES

Figure	Page
3.1 An ungrouted wall (a), A partially grouted wall (b), and a fully grouted wall (c).....	8
3.2 Biaxial failure criterion	9
3.3 Compressive stress-strain diagram	10
3.4 Exponential crack opening law	11
3.5 Element orientation and size effect corrections	13
3.6 Interface element local axis	14
3.7 Interface element surface	14
3.8 (a) Shear stress versus displacement and (b) Tensile stress versus displacements	15
3.9 Maximum projected length of (a) quadrilateral and (b) triangular meshes.....	17
3.10 Element orientation effect of compression softening	18
3.11 Element orientation effect of tension softening.....	18
3.12 Element type schematic	22
3.13 (a) Modified C1072 test setup (b) ASTM E518 test setup	23
3.14 (a) Direct shear test and the (b) Triplet test setup.....	24
3.15 (a) Simplified stiffness model, (b) Prism modulus of elasticity test specimen, (c) Simplified.....	26
3.16 Example of the calibration process.	29
3.17 Equivalent uniaxial stress-strain diagram	30
3.18 Pure tension test cracking patterns.....	31

List of Figures (Continued)

Figure	Page
3.19 Pure tension test stress versus displacement curves*, **	31
3.20 Pure compression test crushing patterns	32
3.21 Pure compression test versus displacement curves*, **	33
3.22 Prism tension and compression behavior check	34
3.23 Shear modeling schemes	35
3.24 Interface failure envelopes	36
3.25 Diagonal tension test setup	36
3.26 Compression Calibration (a) Tension Calibration (b)	38
3.27 Grouted Bed Joint Calibration Curve	39
3.28 Mortar Interface Calibration Curve	40
3.29 Grouted Brick Calibration Curve.....	40
3.30 Cut Grouted Brick Calibration Curve	41
3.31 Model cracking pattern (a) and experimental cracking patterns (b)	42
4.1 Typical test setup per DIN EN 1052-3	55
4.2 Failure modes described by DIN EN 1052-3.....	56
4.3 Apparatus for testing masonry triplets under shear and normal compression loads.....	57
4.4 Mode 1 failure – combined joint and unit failure (a) before triplet blocks were separated and (b) after triplet blocks were separated.....	59
4.5 Mode 2 failure – longitudinal splitting and face shell spalling followed by grout failure (a) before triplet blocks were separated and (b) after triplet blocks were separated.	60

List of Figures (Continued)

Figure	Page
4.6 Lines of best fit, showing cohesion value and shear friction coefficients, for EC and ES aggregates plotted against normal weight (NW) experimental data and equation set 4-1 from TMS 402/602-22	64
4.7 Finite element modeling scheme and boundary conditions.....	66
4.8 Prism Compression stress versus strain curves.....	68
4.9 ATENA grouted bed joint failure envelopes.	70
4.10 Model normal stress and shear stress distributions at difference precompression loads.....	74
4.11 Model versus experimental peak loads.	75
4.12 Equation set 4-1 reduced by minimum reduction factors equation set 4-3 in comparison with the unreduced version and the EC and ES datasets.	77
5.1 Modified C 1390 Testing Apparatus [60].....	81
5.2 Hamid, A. et al. Test Set-Up [61]	82
5.3 ASTM C1072 Bond Wrench Testing Apparatus	84
5.4 Schematic of the test set up (a) and the physical test set up (b).....	85
5.5 Loading and Specimen Orientation	87
5.6 Demonstration of Specimen Placement and Connection from Masonry to the Loading Arm.....	87
5.7 Holes Drilled in Masonry.....	95
5.8 Masonry Specimen Preparation	96
5.9 String pot and Actuator Set Up.....	97
5.10 Typical Failures	97

List of Figures (Continued)

Figure		Page
5.11	$\frac{f_r}{\sqrt{f_g}}$ NW and LW batch comparison.....	106
5.12	$\frac{f_r}{f_{rp}}$ NW and LW batch comparison.....	106
6.1	General Shear Wall Design Dimensions.....	111
6.2	Proposed Design Reduction Factors for TMS 402/602	114
6.3	Light weight block design outcomes	117
6.4	Normal weight block design outcomes.....	117

CHAPTER ONE

INTRODUCTION

Motivation and Research Overview

Lightweight (LW) aggregates have many potential benefits in masonry construction including minimizing mass, improving thermal performance, and reducing the potential for shrinkage cracking via internal curing. The current masonry design standard, TMS 402/602-22, permits lightweight aggregate in the production of concrete masonry units (CMU), but there has been insufficient testing of masonry assemblies to permit designing with LW grout. A codified procedure must be developed so the benefits of LW aggregates can be fully utilized.

Summary of Current Literature and Identified Gaps

A minimal amount of work has been done to identify properties and possible reduction factors required for design using LW grout.

Current works in the literature include:

- Clarke, Silva, and Roufael et. al. [1, 2, 3] characterized increased thermal resistance of LW concrete.
- Ma et. al. [4] characterized LW concretes internal curing properties.
- Tanner, and Polanco [5, 6] characterized LW grout wet and cured properties.
- Shrestha et al. [7] characterized LW grouts bond to reinforcement and shear strength and proposed possible reduction factors for design.

- Petty et. al., Bane, and Shrestha et. al. [8, 9, 10] characterized tension and shear pullout behavior of anchors in LW grouted masonry assemblies.
- Hiner [11] characterized the flexural bond strength LW grouted masonry assemblies and proposed possible reduction factors for design.

Contributions from this work:

- Confirm the validity of reduction factors proposed by Kessler through finite element analysis of LW grout masonry assembly triplet tests.
- Expand the on the testing of Hiner [11] with an additional grout mix and compare the calculated reduction factors based on the density of the grout types.
- Complete a design study to highlight the possible financial benefit of using LW grout using an in-plane loading scenario of an ordinary masonry shear wall leveraging the proposed reduction factors for design from Shrestha and Hiner [7, 10, 11] and this work.

Summary of Research Objectives

The first study expands upon the data set of Hiner [11] to propose a relationship between grout density and the reduction factors for flexural bond strength. The second study validates reductions factors found by Kessler using the commercially available software ATENA. The final study presents the possible financial benefits of using LW grout masonry in design.

Outline of Thesis

The following thesis manuscript is organized into the following chapters:

- Chapter 1 discusses the motivation behind this work, overviews gaps in the previous literature, and summarizes the objectives and contributions of the studies presented hereafter.
- Chapter 2 provides a review of previous literature on LW grout in masonry.
- Chapter 3 outlines the modeling scheme used to validate the triplet test discussed in chapter 4.
- Chapter 4 outlines triplet test study conducted by Kessler and the additional analytical validation contributed from this work.
- Chapter 5 outlines the flexural bond wrench study started by Hiner, the additional grout mix tested through this work, and a newly proposed relationship for design reduction factors based on grout density.
- Chapter 6 outlines the ordinary masonry shear wall design, constraints, and cost estimation method and summarizes cases where using LW grout would result in significant economic savings.
- Chapter 7 summarizes the research's current contributions and future works that may be conducted based on results of this study.

CHAPTER TWO

LITERATURE REVIEW

LW aggregates have been used as a construction material for centuries and are still widely used in the construction industry today. LW grouts have been found to have excellent thermal insulation due to low thermal conductivity of the air trapped in the porous structures of LW aggregates [1]. LW concrete produced with EC or ES aggregates has a 30 to 60% lower coefficient of thermal conductivity than normal weight (NW) concrete [2]. LW aggregate can contribute to internal curing based on amount used, pretreatment, particle size and distribution in concrete. Prewetting the LW aggregate has been shown to result in more effective internal curing compared to dry LW aggregate [4]. LW aggregate concrete has shown lower permeability and thermal expansion coefficients as well as slower degradation of tensile strength as compared to NW concretes under thermal loads [1, 3].

The use of LW aggregates in concrete has been shown to affect the tensile strength [12], shear strength [13], splitting resistance [12, 14], and the bond between concrete and reinforcement [7, 14] compared to NW concrete with similar compressive strength. For this reason, the ACI 318-19 code [15] includes a Lambda factor that modifies the predicted strength of members constructed with LW concrete.

Self-compacting concrete (SCC) is extremely flowable and may be more analogous to grout behavior. LW aggregates in SCC have been shown to affect: the amount of superplasticizer required to achieve a target slump [16], the tensile strength [17], the flexural strength [16], and the durability properties [18] of the SCC, depending

on the percentage NW aggregate that is replaced with LW aggregate. LW aggregate in SCC have also been noted to have good frost resistance even with its decrease to tensile strength, but have increased water absorption, and corrosion risks [19].

There has been limited research on lightweight grout's wet and cured properties in isolation from its behavior within a masonry assembly. Petty et. al. [8] designed LW grouts using blast furnace steel slag aggregate whose axial tensile strength, compressive strength, and shrinkage performances were comparable to, if not better than NW grouts. Tanner [5] maintained that tests on grout containing expanded shale aggregate were within an acceptable range compared to masonry code and ASTM standards for slump, unit weight, air content and segregation. Polanco [6] also performed experiments on expanded shale grout and found it to comply with the requirements of ASTM C476 [20]. Bane [9] conducted tests to determine the hardened grout properties. The tests included: a modified ASTM C39 [21] (Compression Strength), ASTM E518 [22] (Modulus of Rupture), ASTM C469 [23] (Modulus of Elasticity), ASTM C496 [24] (Splitting Tensile Strength). These tests were conducted using crushed LW sand and natural sand as fines and pea gravel, limestone, and expanded slate as coarse aggregate.

There has also been limited work in the literature on the behavior of masonry assemblies containing lightweight grout. Shrestha et al. [7] completed diagonal tensile strength tests and lap splice tests. The strengths of the specimen were compared to the NW tests from past literature and predicted values using equations provided in TMS 402/602-16 for NW specimen. Shrestha et al. [7] concluded a reduction factor for the design value of diagonal tensile strength and lap splice strength for LW grout assemblies

is needed. Shrestha et al. [10] tested the tensile and shear breakout capacity of cast-in-place bent-bar anchors in masonry assemblies. The specimen strengths were compared to the predicted value given by TMS 402/602-16 equations for NW grout and previous results from NW assemblies in literature. It was determined a reduction factor was not required for bent-bar anchor bolts in LW masonry assemblies subjected to tension but required for bent-bar anchor bolts in LW masonry assemblies subjected to shear. However, the authors suggested that this conclusion be further validated with additional testing on different bar diameter anchors. Recent work, by Henderson et al. [25] has compared the strength and modulus of elasticity of masonry prisms constructed with LW and NW grout. They tested prisms between 2,000 psi (14 MPa) to 4,000 psi (28 MPa) in strength. They found a 20% reduction in the modulus of elasticity in the LW samples and suggested a LW reduction factor dependent on the prism strength of the samples [25]. The proposed research is an attempt to fill the gap in comparing NW and LW grout behavior for flexural bond strength, and shear strength under different levels of precompression.

CHAPTER THREE

FINITE ELEMENT MODELING

Introduction

This work uses the finite element solver and material models provided by ATENA in combination with the modeling scheme proposed by Lotfi and Shing [26] and later updated by Stravridis and Shing [27]. The meshing scheme follows the one used by Redmond [28]. The scheme uses fixed smeared crack elements to model compression and tension failure of the masonry, and interface elements to model shear failure and tension failure. In this chapter the modeling scheme is outlined, the element formulations are described, and the calibration is outlined. After the modeling scheme is calibrated, validation studies are presented. The results of these studies show the modeling scheme is capable of accurately capturing the behavior of masonry systems with LW grout.

Modeling Scheme

In this modeling scheme, the masonry blocks are modeled with two smeared crack band elements separated by a vertical block interface element. Each smeared crack band element represents half of the block. The mortar head and bed joints are also modeled using interface elements. In the case of grouted masonry walls, the smeared crack band elements representing grouted cores are replaced with a module of four triangular smeared crack band elements and four diagonal interface elements representing the grout and masonry. This change can be seen in Figure 3.1a, Figure 3.1b, and Figure 3.1c as they show an ungrouted, partially grouted, and fully grouted wall, respectively.

The legend labels the type of material the interface elements represent. Note that a finer mesh may be used where each $\frac{1}{2}$ block may contain multiple smeared crack band elements (if ungrouted) or multiple modules of the smeared crack band and interface elements (if grouted).

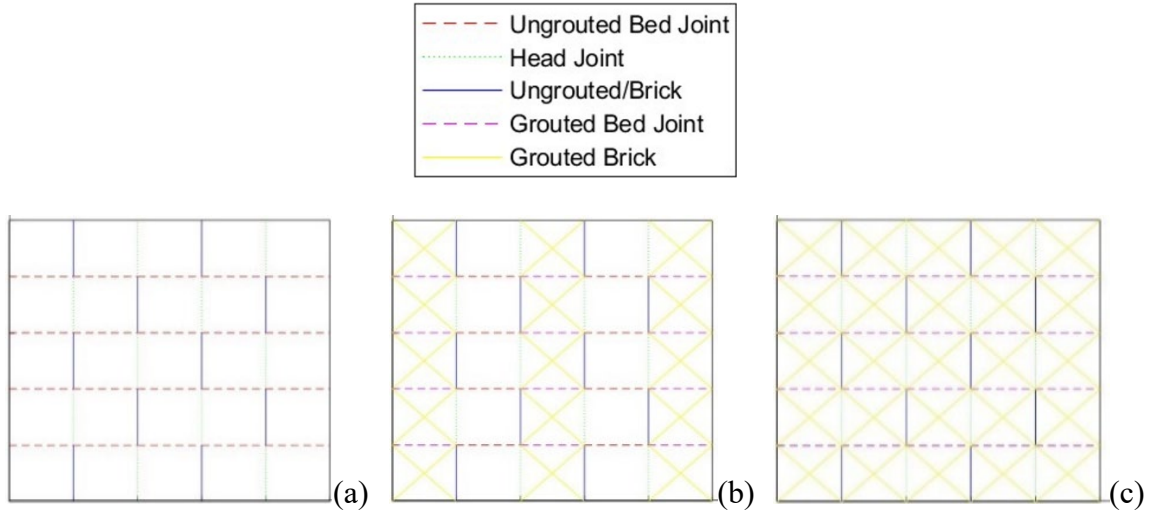


Figure 3.1: An ungrouted wall (a), A partially grouted wall (b), and a fully grouted wall (c)

Element Formulation

Smeared Crack Band Elements

The smeared crack band elements used the SBETA material model presented in the ATENA Theory Section 2.1 [29]. The failure surface is represented by the biaxial stress failure criterion presented by KUPFER et al. [30] shown in Figure 3.2. The failure surface is defined by equation sets 3-1 through 3-3. Where σ_{c1} and σ_{c2} are the principal stresses in concrete and f'_c is the uniaxial cylinder strength of the concrete. Equation set 3-1 is applied under biaxial compression and predicts the effective concrete compression strength, $f'_c{}^{ef}$, under a proportional stress path assumption. Equation set 3-2 is applied in

the tension-compression state. Equation set 3-3 is applied in the tension-tension state of principal stresses. Equation set 3-3 can be represented in two forms, a linear decrease of the tensile strength or hyperbolic decrease. f'_t represents the uniaxial tensile strength of the concrete, while A and K are constants that define the shape of the hyperbola, section 2.1.5.1 [29].

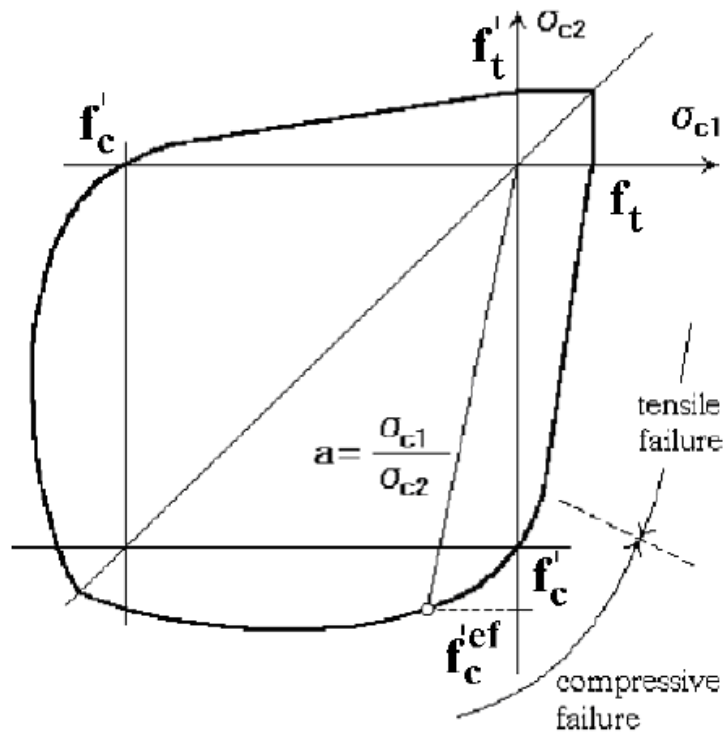


Figure 3.2: Biaxial failure criterion [29]

$$f_c^{'ef} = \frac{1+3.65a}{(1+a)^2} f_c', a = \frac{\sigma_{c1}}{\sigma_{c2}} \quad \text{Equation Set 3-1}$$

$$f_c^{'ef} = f_c' r_{ec}, r_{ec} = \left(1 + 5.3278 \frac{\sigma_{c1}}{f_c'}\right), 1.0 \geq r_{ec} \geq 0.9 \quad \text{Equation Set 3-2}$$

$$f_t^{'ef} = f_t' r_{et}, r_{et} = 1 - 0.95 \frac{\sigma_{c2}}{f_c'} \text{ or } r_{et} = \frac{A+(A-1)B}{AB}, B = Kx + A, x = \frac{\sigma_{c2}}{f_c'} \quad \text{Equation Set 3-3}$$

The compressive behavior of the element between the initial yield surface and the failure surface is governed by a linear softening displacement law (Figure 3.3). The shape of the plasticity curve is governed by $f_c^{'ef}$, the concrete effective compressive strength from the biaxial failure criterion; ϵ_c , strain at the peak stress $f_c^{'ef}$; E_o , the initial elastic modulus; E_c , the secant elastic modulus at peak stress; k , a shape factor that must be greater than or equal to 1; and E_d , the softening modulus. The stress versus strain diagram before the peak stress is reached is defined by equation set 3-4, section 2.1.2.4 [29].

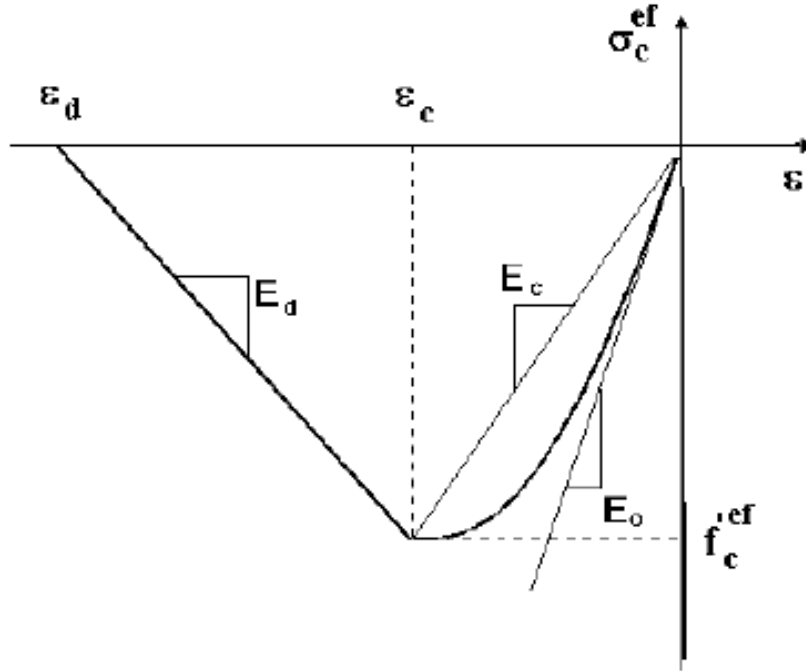


Figure 3.3: Compressive stress-strain diagram [29]

$$\sigma_c^{ef} = f_c^{'ef} \frac{kx - x^2}{1 + (k-2)x}, x = \frac{\varepsilon}{\varepsilon_c}, k = \frac{E_0}{E_c}, E_c = \frac{f_c^{'ef}}{\varepsilon_c}$$

Equation Set 3-4

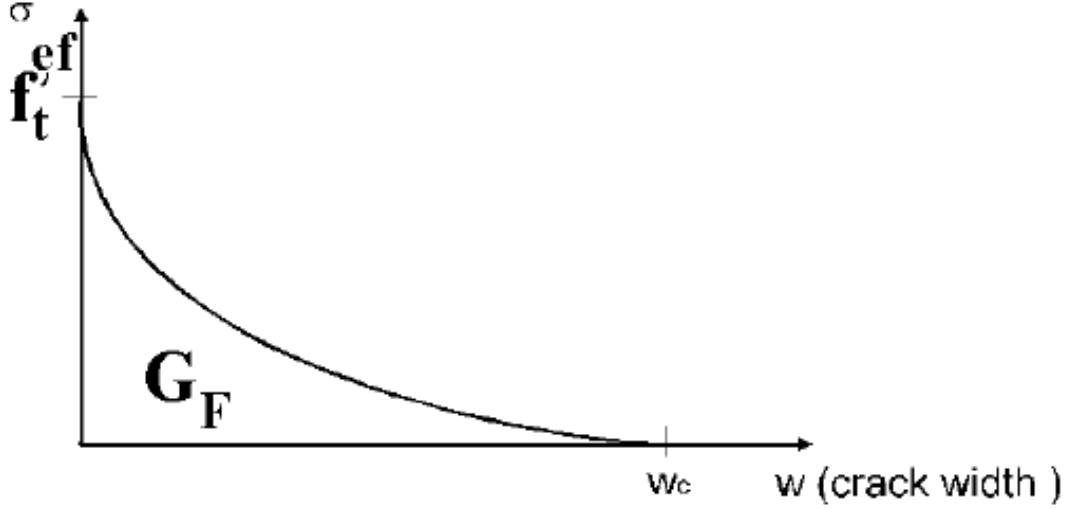


Figure 3.4: Exponential crack opening law [29]

$$\frac{\sigma}{f_t^{'ef}} = \left\{ 1 + \left(3 \frac{w}{w_c} \right)^3 \right\} \exp \left(-6.93 \frac{w}{w_c} \right) - \frac{w}{w_c} (10) \exp(-6.93), w_c = 5.14 \frac{G_f}{f_t^{'ef}}$$

Equation Set 3-5

The tensile failure occurs when the maximum principal stress reaches a Rankine-type cut-off criterion. The material then follows a fictitious crack model based on a crack-opening law and fracture energy [29]. The crack opening law used in this work is the exponential crack opening law derived by HORDIJK [31] (Figure 3.4). The crack opening law is defined by equation set 3-5 where w is the crack opening. Before failure, the concrete is linear elastic. After failure, the concrete follows the exponential crack opening law that is controlled by $f_t^{'ef}$, the effective tensile strength from the biaxial failure criterion; and G_f , the mode I fracture energy, section 2.1.2.3 [29].

Typically, smeared crack models have isotropic and orthotropic properties that are followed depending on if the concrete is uncracked or cracked. This is not the case for the

ATENA SBETA material model because it is based on the Crack Band Theory, described by Bazant and OH [32]. This material model relies on a compliance matrix in which single terms can be changed at a time rather than a stiffness matrix where every term needs to be recalculated when failure occurs [32]. The SBETA material model represents failures as fictitious planes normal to the direction of principal stress in tension or compression. The post-peak displacements and energy dissipation are localized in these planes. To account for the element size effect, the characteristic length, L_c , of each element is taken as the projected length of the element on a plane normal to the failure plane, Figure 3.5. Typically, the characteristic length is calculated as the square root of the elements area [33], but this is not true for ATENA's SBETA material model. For quadrilateral meshes, the characteristic length is corrected to account for the element orientation effect by multiplying the characteristic length by an element orientation factor, γ . Equation set 3-6 shows how the element orientation factor is calculated where, θ , is the minimum angle ($\min(\theta_1, \theta_2)$) between the direction of the normal to the failure plane and element sides shown in Figure 3.5. The element orientation factor varies linearly from 1.0 to 1.5. For cases where a module of four triangular elements fail, the element with the largest calculated characteristic length governs the softening curve. The SBETA material model is compatible with fixed or rotating crack models. This study will use fixed cracks.

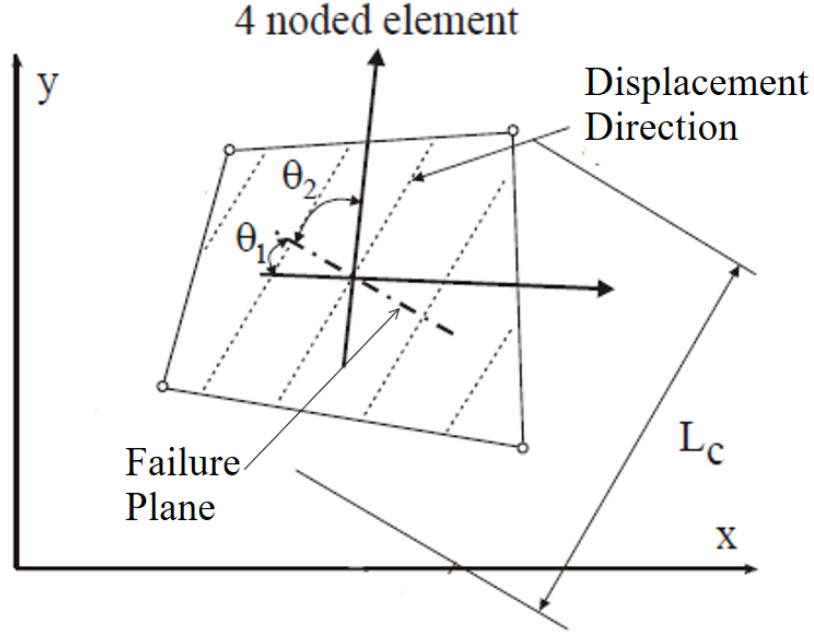


Figure 3.5: Element orientation and size effect corrections [29]

$$\gamma = 1 + (0.5) \frac{\theta}{45}, \quad \theta \in (0; 45)$$

Equation Set 3-6

Interface Elements

The interface elements in ATENA are double-noded elements with zero thickness (Figure 3.6). The interface model can model mode-I, mode-II, and mixed mode fracture. The interface models do not fail in compression. Their main function is to model the opening of cracks. The failure surface is a Mohr-Coulomb failure surface with an ellipsoid tension region (Figure 3.7). This failure surface is defined by equation sets 3-7, 3-8, and 3-9. The failure surface is governed by σ , the normal stress at the interface; f_t , the tension strength of the interface; ϕ , the friction coefficient of the interface; and c , the cohesion of the interface, section 2.6 [29].

The user can define softening laws for the cohesion and tension strength of the elements. The stress versus displacement curves for shear and tensile stress are shown in Figure 3.8a and Figure 3.8b, respectively. The dotted line represents the stress versus strain behavior with user-defined softening laws applied and the solid line is the behavior without a defined softening law, section 2.6 [29].

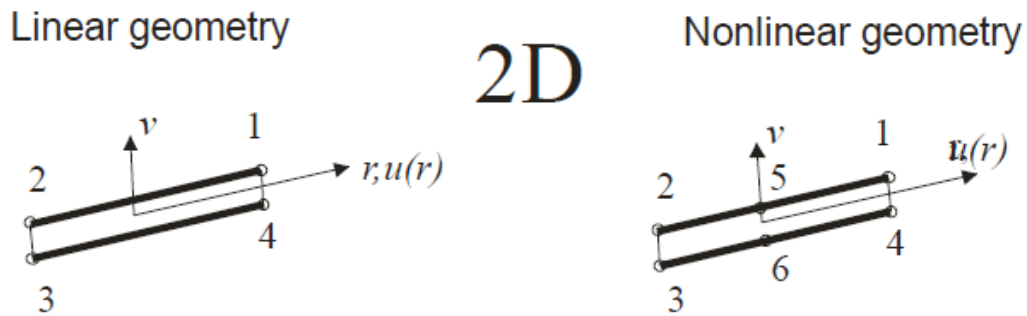


Figure 3.6: Interface element local axis [29]

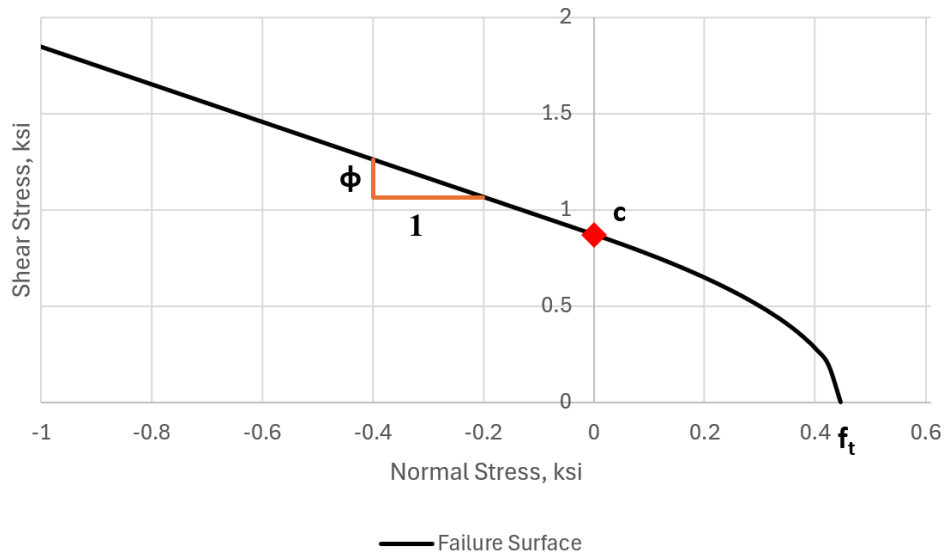


Figure 3.7: Interface element surface

$$|\tau| \leq c - \sigma * \phi, \text{ when } \sigma \leq 0$$

Equation Set 3-7

$$\tau = \tau_0 \sqrt{1 - \frac{(\sigma - \sigma_c)^2}{(f_t - \sigma_c)^2}}, \tau_0 = \frac{c}{\sqrt{1 - \frac{\sigma_c^2}{(f_t - \sigma_c)^2}}}, \sigma_c = -\frac{f_t^2 \phi}{c - 2f_t \phi}, 0 < \sigma \leq f_t$$

Equation Set 3-8

$$\tau = 0, \sigma > f_t$$

Equation Set 3-9

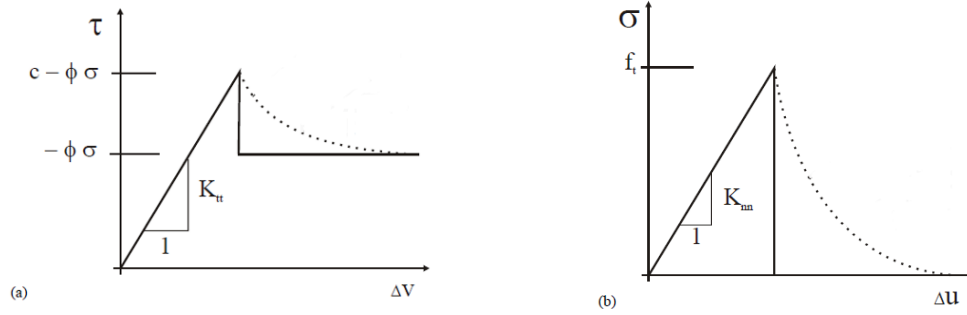


Figure 3.8: (a) Shear stress versus displacement and (b) Tensile stress versus displacements [29]

Mesh Size Dependance

For smeared crack band elements, the parameters that are dependent on the mesh size include the critical compressive displacement, w_d , and the mode I fracture energy, G_f^I . Both should be scaled to the characteristic length of the elements. To simplify this, the characteristic length for quadrilateral elements can be taken as the length with the lowest root mean squared (RMS) error as compared to the projected length times the element orientation factor at any orientation. For triangular elements the element orientation factor is neglected [34]. Figure 3.9 shows the range of characteristic lengths over any orientation for quadrilateral and triangular meshes and the RMS value. The elements mentioned in Figure 3.9 4in by 4in quadrilateral elements and 45-45-90

triangular elements with an 8in hypotenuse. The effect the element orientation has on the compression and tension softening is shown in Figure 3.10 and Figure 3.11.

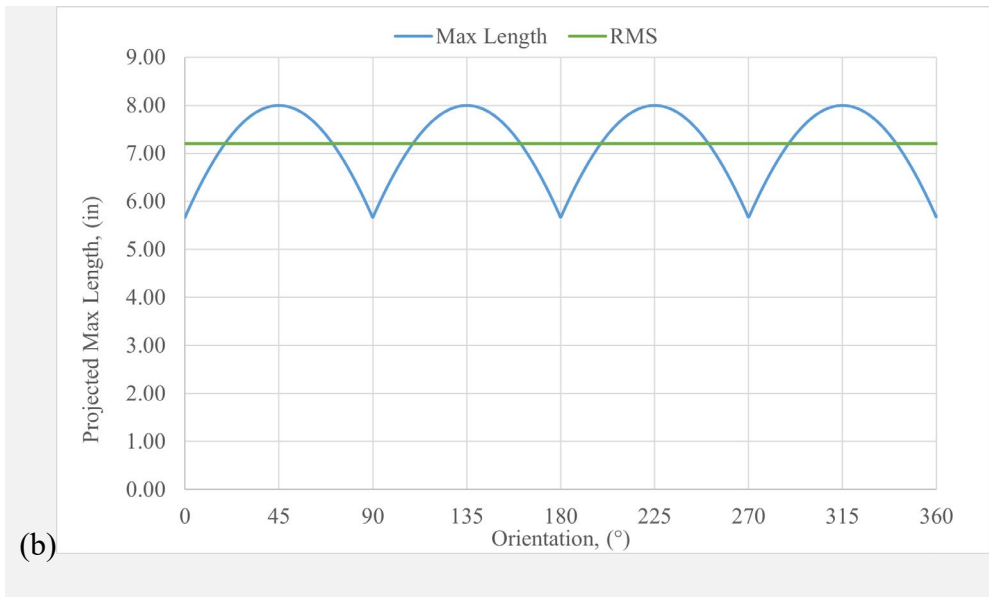
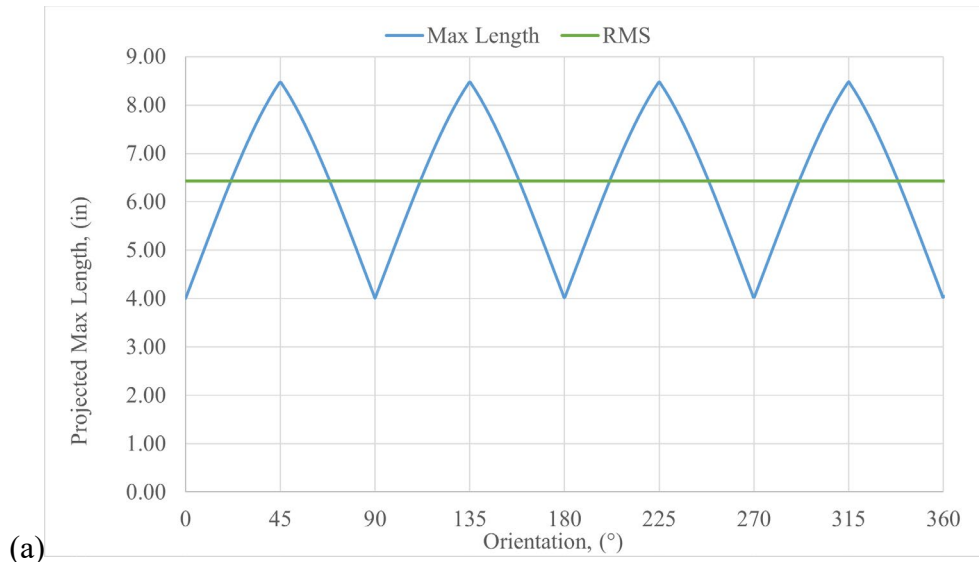


Figure 3.9: Maximum projected length of (a) quadrilateral and (b) triangular meshes

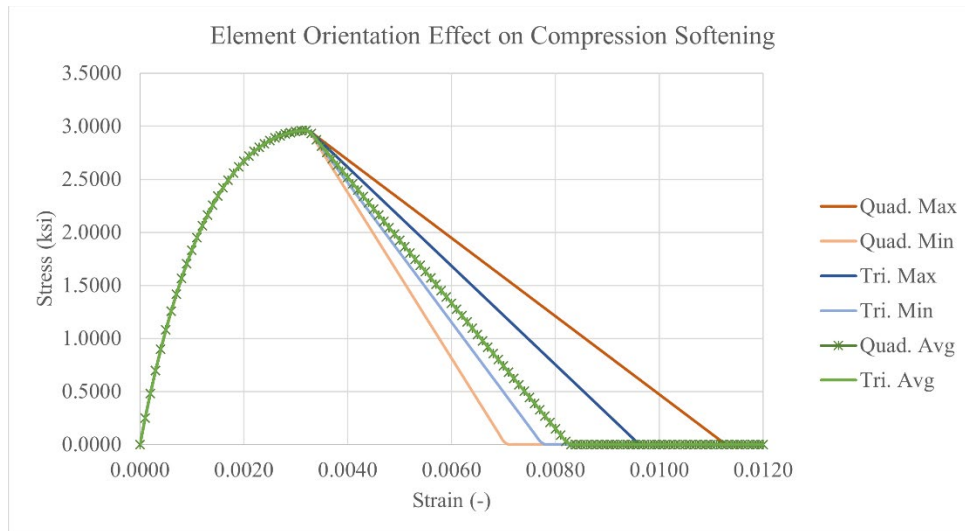


Figure 3.10: Element orientation effect of compression softening

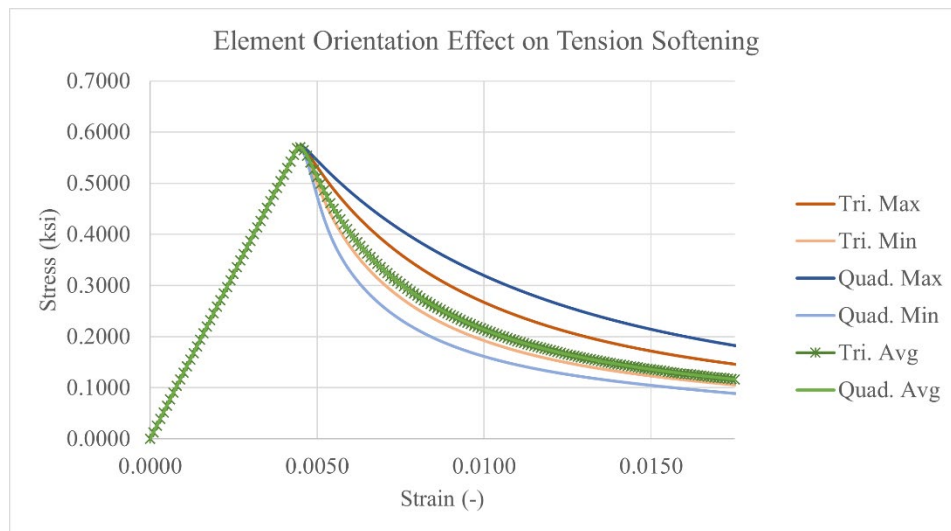


Figure 3.11: Element orientation effect of tension softening

For interface elements the mode I fracture energy, G_f^I , needs to be calibrated based on the distance between parallel interface elements. This means that a different fracture energy is required for each interface orientation.

Material Calibration

Block Calibration

To calibrate the module comprised of smeared crack band elements and interface elements the tension behavior of each elements needs to be aligned so that cracking in one element is not preferred over cracking in the other. To do this, the smeared crack band element is first calibrated to the grouted block material properties and then the interface elements user defined softening equations are input to match the smeared crack band elements.

Pure tensile tests on concrete masonry block are rarely performed. If these tests cannot be conducted, the tensile strength can be assumed to be 10 to 15 percent of the grout's compression strength, which is in the family of typical ranges for tensile strength of concrete. Mode I fracture energy, G_f^I , can be assumed from typical values [35] or calculated from empirical formulas [36]. The initial elastic modulus, E_o ; secant elastic modulus, E_c ; strain at the peak stress, ϵ_c ; and softening modulus, E_d can be estimated from ASTM C1019 tests for grout properties and C90 tests for concrete block properties, if full stress vs. strain data is obtained. For grouted masonry, calculations assuming their combined property reflects a volume-proportional behavior, or calibrating the elements to tests of grouted block may be conducted. These values can then be used to calibrate the

smeared crack band elements. If these values cannot be gathered from testing, it is reasonable to approximate them from relationships with the compressive strength of the grout found in literature [25].

The softening modulus, E_d , must be input in terms of plastic displacement, w_c , and characteristic length, L_c , which is dependent on the mesh size and failure plane orientation. The softening modulus can be calculated with Equation set 3-10 and must remain the same when the mesh size changes.

$$E_d = \frac{f_c^{ef}}{w_c/L_c} \quad \text{Equation Set 3-10}$$

The interface elements representing the concrete masonry block or grouted masonry block are calibrated with the same tensile strength as the smeared crack band elements. The dry friction ϕ can be assumed from typical values, but the cohesion, c , must be greater than 2 times the product of the dry friction and tensile strength per ATENA limits (Equation Set 3-11). To make sure the interface elements do not affect the stiffness of the grouted block before fracture the interface stiffnesses, K_{tt} and K_{nn} , must be large values, but not too large to ill-condition the solution. It is recommended to use value 100 times the stiffness of adjacent smeared crack band elements, typically on the order of 10^4 . The residual stiffness, K_{tt}^{MIN} and K_{nn}^{MIN} , will also need to be defined for model stability. At failure the true stiffness is 0, but to keep the global stiffness matrix positive and definite small but not excessively small minimum stiffness values need to be used. These values are typically on the order of 10^1 . Finally, Equation set 3-5 is used to define the user input softening law for the interface element.

$$c > 2f_t \cdot \emptyset$$

Equation Set 3-11

Masonry Assembly calibration

The masonry assembly can be modeled with up to seven different material models as shown in Figure 3.12: the smeared crack band elements representing the ungrouted units (middle square elements in Figure 3.12), the smeared crack band elements representing the grouted units (triangular elements in Figure 3.12), the interface elements representing the block interface (1d in Figure 3.12), the interface elements representing the grouted interface (1e in Figure 3.12), the interface elements that represent ungrouted bed joints (1a in Figure 3.12), the interface elements that represent grouted bed joints (1c in Figure 3.12), and the interface elements representing head joints (1b in Figure 3.12). Each group needs to be calibrated considering the mechanics of the modeling scheme.

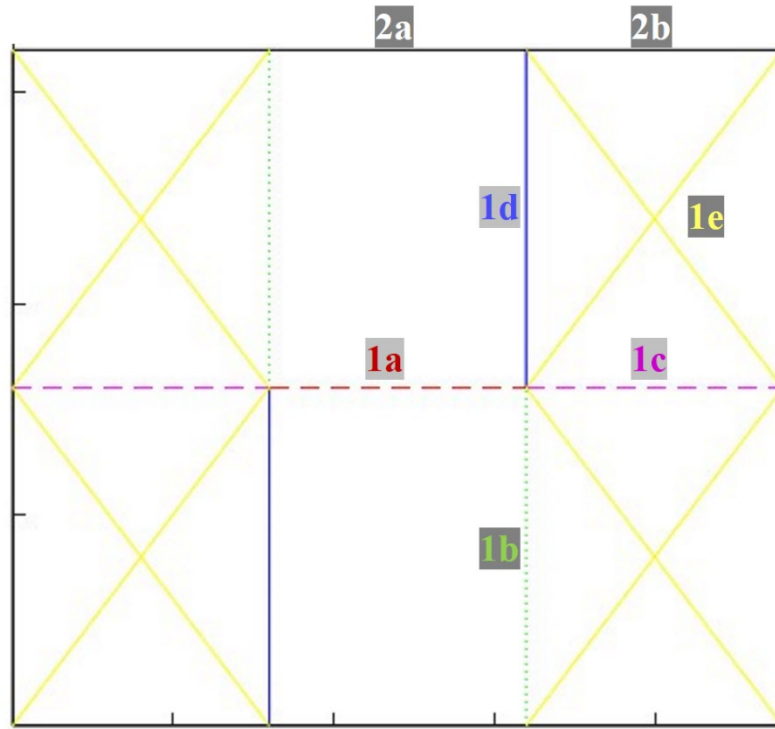


Figure 3.12: Element type schematic

Mortar Interface Elements and Grouted Bed Joint Interface Elements

The calibration process can start with the mortar (ungrouted) and grouted bed joint interface elements labeled in Figure 3.12 as 1a and 1c, respectively. The tensile behavior of bed joints can be calibrated to direct tensile tests. If this data cannot be acquired, bond-wrench [37, 38] or beam tests [22] can be used to calibrate the tensile strength of the mortar interface. The test setup for the testing presented in Banks et. al. and ASTM E518 are shown in Figure 3.13, respectively.

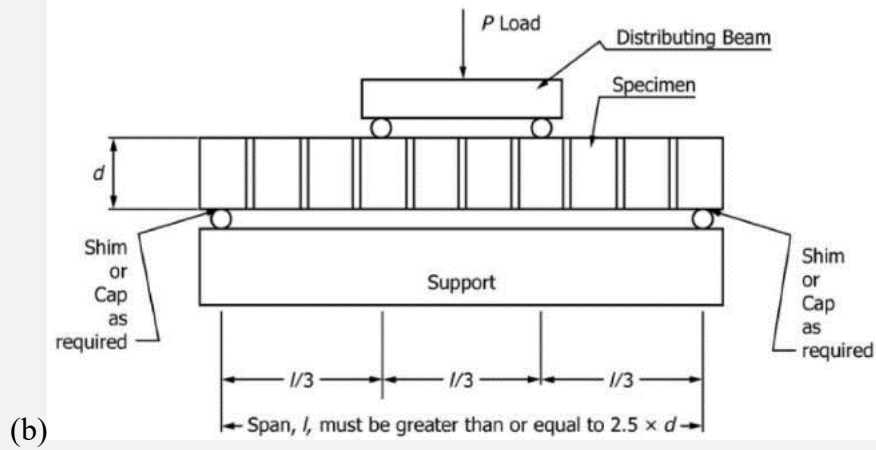
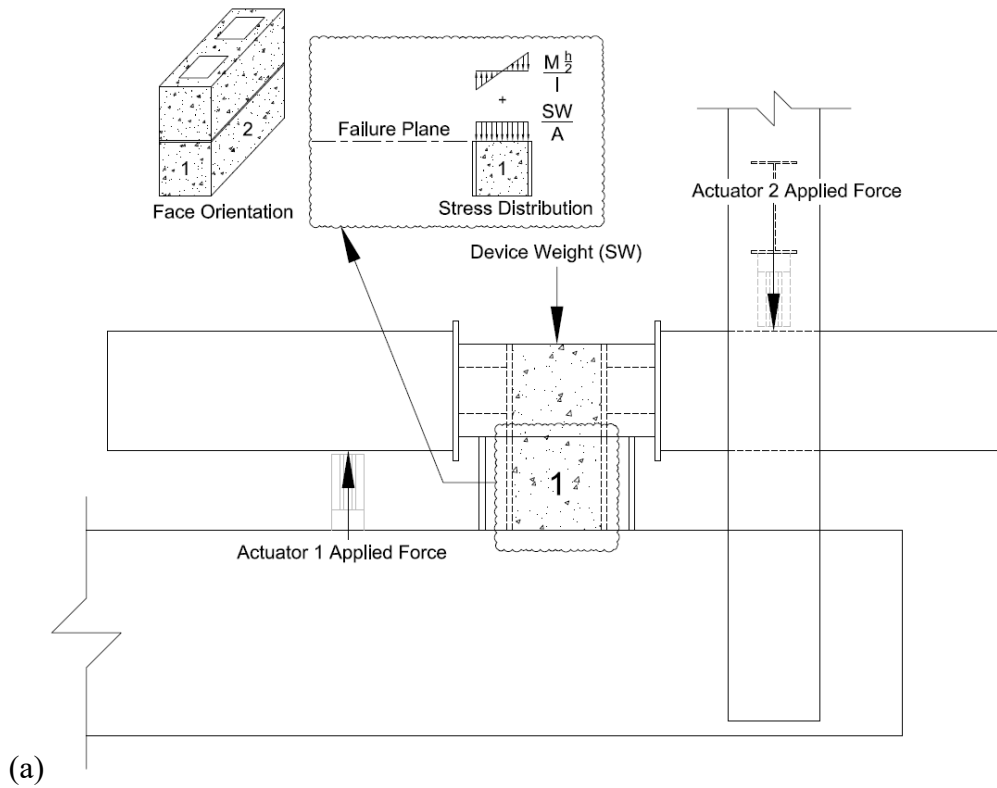


Figure 3.13: (a) Modified C1072 test setup [38] (b) ASTM E518 test setup [22]

The shear behavior of the mortar bed joints can be calibrated with tests that consider the interaction of the mortar joints and block units. The cohesion, c , and friction coefficient, ϕ , can be determined from direct shear tests [39, 40, 41], triplet tests [42], or

shove tests repeated under different values of normal stress. These tests can also provide approximations for the elastic tangential stiffness, K_{tt} , and the mode II fracture energy, G_f^{II} . The elastic stiffness of the mortar joint under normal stress, K_{nn} , can be assumed to be $2 * K_{tt} * (1 + \nu)$. The mode I fracture energy can be obtained from assuming the ratio of G_f^I to G_f^{II} can be between 10 [25, 26, 43]. The setups for ASTM 1531 direct shear test and the DIN EN 1052-3 triplet test are displayed in Figure 3.14.

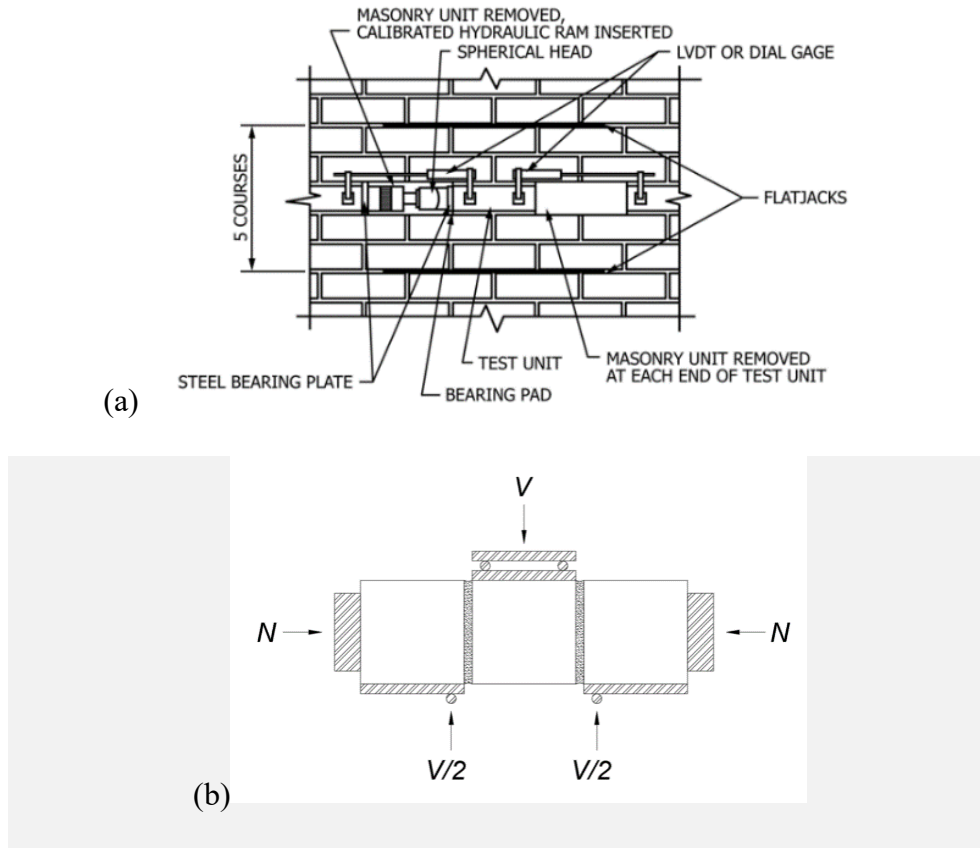


Figure 3.14: (a) Direct shear test [39] and the (b) Triplet test setup [42]

The fracture energies will be used in equation set 3-5 to define the softening laws of tension and shear for the interface elements. If the stiffness normal to the mortar joint cannot be gathered from test data, it is reasonable to approximate the stiffness using the

prism modulus of elasticity. The prism can be modeled as a series of springs with area averaged properties, Figure 3.15. The mortar and block moduli of elasticity, E_m and E_b , can be approximated with their compression strength, f_m and f_b , and the block unit weight, w_b , using empirical equations from Cheema and Klinger [44] shown in equation set 3-12. The area of the grout, A_g , mortar, A_m , block, A_b , and prism, A_p , are then used to find the area weighted modulus of elasticity of the grouted block, E_{gb} , and grouted bed joint, E_{gbj} in equation set 3-13. The length of the prism, L_p , grouted block, L_{gb} , and grouted bed joint, L_{gbj} , can then be used to find the stiffness of the prism, k_p , grouted block, k_{gb} , and grouted bed joint, k_{gbj} , the grout modulus of elasticity can be edited until the known stiffness of the physical prism and combined stiffness of the modeled grouted block and grouted bed joint are equal (seen in equation set 3-14). The references for variables not directly related to the geometry of a grouted block are listed in Table 3.1. The final normal stiffness of the grouted bed joint can be calculated using equation set 3-15.

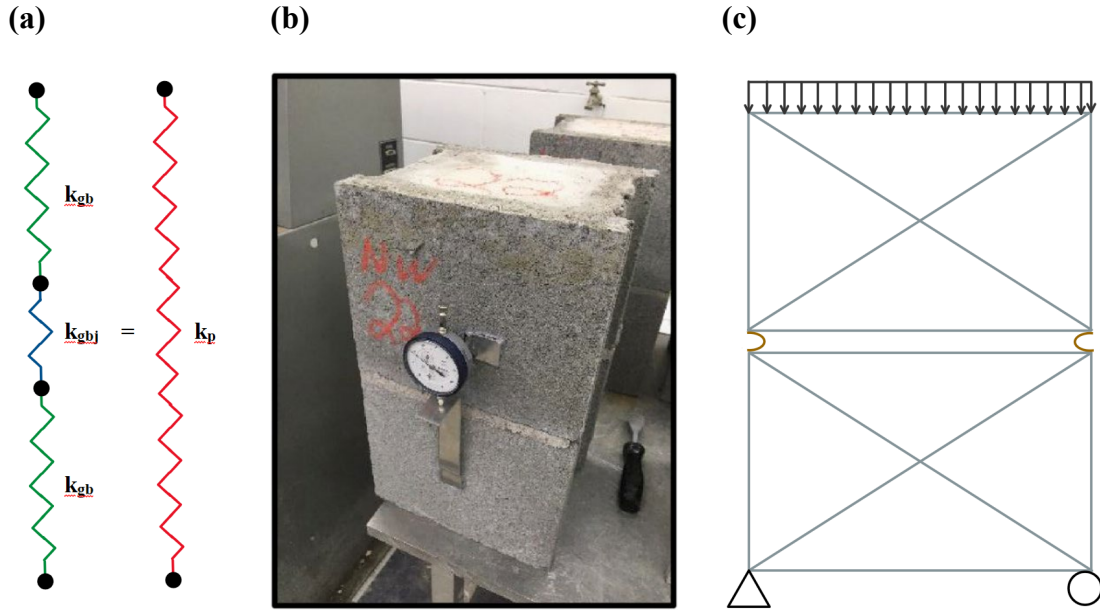


Figure 3.15: (a) Simplified stiffness model, (b) Prism modulus of elasticity test specimen [25], (c)

Simplified

Table 3.1: Stiffness variable references

	E_m	[44]
	E_b	[44]
	E_g	Varied to match required stiffness
$E_m = 1000 \cdot f'_m$	$E_b = 22(w_b^{1.5})\sqrt{f'_b}$	Equation Set 3-12
$E_{gb} = \frac{A_g \cdot E_g + A_b \cdot E_b}{A_p}$	$E_{gbj} = \frac{A_g \cdot E_g + A_m \cdot E_m}{A_p}$	Equation Set 3-13
$\frac{1}{k_p} = 2 \frac{1}{k_{gb}} + \frac{1}{k_{gbj}}$, $k_p = \frac{A_p E_p}{L_p}$, $k_{gb} = \frac{A_p E_{gb}}{L_{gb}}$, $k_{gbj} = \frac{A_p E_{gbj}}{L_{gbj}}$		Equation Set 3-14
$K_{nn} = \frac{E_{gbj}}{L_{gbj}}$		Equation Set 3-15

Mortar head joints, labeled as 1b in Figure 3.12, have worse bond strength when compared to the ungrouted mortar bed joints because of the difficulty in placing them and they do not benefit from axial compression to reduce shrinkage stresses [45, 46]. Mortar head joints are typically numerically represented by the same properties of the mortar bed joints [47, 48] or are assumed to have nearly no bond strength [49, 50]. Based on the sensitivity study of [28] the head joint to ungrouted bed joint bond strength will be initiated at 0.5 for all models and increased if cracking patterns are inconsistent with the experimental observations.

Assembly of Smeared Crack Band Elements and Interface Elements Representing UngROUTED or GROUTED Block

The ungrouted block and grouted block units are represented by a combination of smeared crack band elements and interface elements. For both scenarios, grouted and ungrouted, the elements need to be constantly calibrated so that cracking is not favored in one element over the other. The smeared crack band elements can be calibrated first. The tensile strength of the block is typically assumed to be 10-15% of the compressive strength assuming a volume proportional property between the grout and the unit compression strength (grouted block). Data from literature can also help in approximating mode I fracture energy, G_f^I , [35, 36].

The calibration of the block and grouted interface elements in tension uses the same value of tension strength and mode I fracture energy found for the corresponding smeared crack band element. The mode II fracture energy, G_f^{II} , can be approximated by using the same relationship mentioned for mortar interface elements. The friction

coefficient, ϕ , and cohesion, c , can be difficult to calibrate so values can be selected from literature conservatively. The softening laws for the interface elements can be defined by equation set 3-5 with the corresponding fracture energies. The interface elements should not affect the behavior of the masonry before fracture so their normal and tangential stiffness, K_{tt} and K_{nn} , should be high, but not too high to make the model numerically ill-conditioned.

The compression failure of the masonry smeared crack band elements can be calibrated to the prism strength of ungrouted and grouted assemblies. The flexibility of the mortar interface should be considered so that two smeared crack band elements and one mortar interface element represent the prism stress-strain curve. Thus, the stress vs. strain behavior from a prism test should be compared to the stress vs. strain behavior of an analytical prism, Figure 3.16. Note that the individual stiffness of the mortar joint and units needs to be calibrated together, typically assuming a stiffness for the unit and mortar based on equations from Cheema and Klinger and then selecting the appropriate grout stiffness to match the prism behavior using the equations in the Mortar Interface Elements and Grouted Bed Joint Interface Elements section. The stress-strain curve of the prism can also be used to calibrate the strain at peak stress, ϵ_c , the initial elastic modulus, E_o , and the softening modulus, E_d .

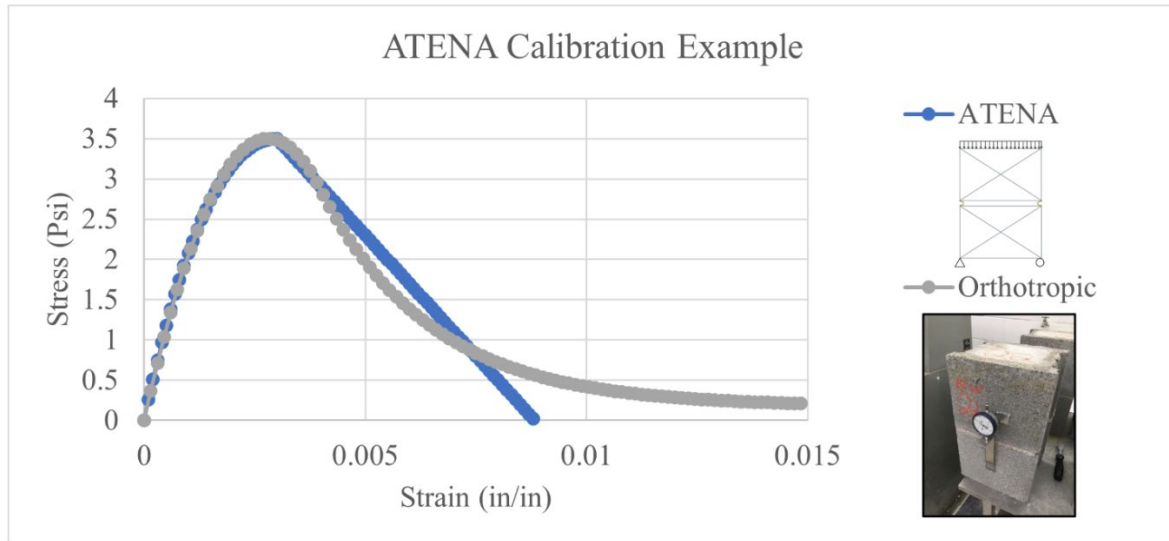


Figure 3.16: Example of the calibration process.

Model Validation

The finite element modeling scheme is evaluated in a series of models ranging from single elements to large scale tests. Element level tests in pure tension and compression were conducted first to understand the influence of the interface elements. Then the modeling scheme was compared against the system wide behavior of prism tests and finally diagonal tensions tests conducted by Shrestha [7].

ATENA Outputs

In the principal stress directions ATENA outputs the material state of the SBETA material model. The material states correspond to 4 different regions of the equivalent uniaxial stress-strain diagram (Figure 3.17).

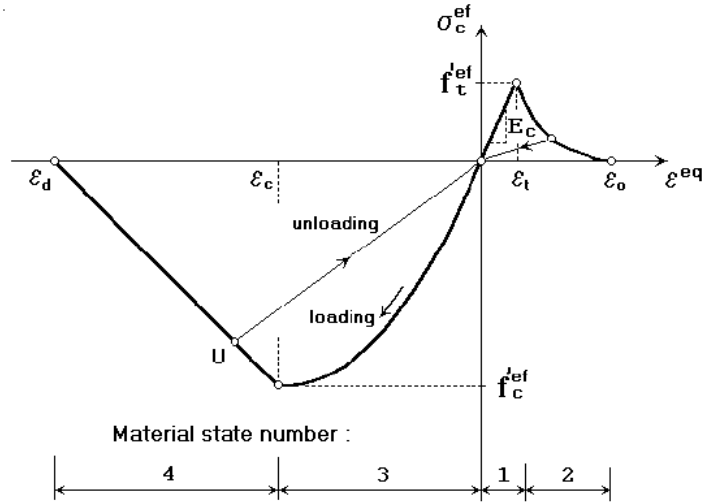


Figure 3.17: Equivalent uniaxial stress-strain diagram [29]

Pure Tension and Compression

To understand the effect of adding interface elements along the boundaries of smeared crack band elements, pure tension and compression models were evaluated using 8x8 inch square samples discretized with one element, four elements, and sixteen elements, with and without perpendicular and diagonal interface elements. The legend labels correspond with the interface orientation and the number of elements. Figure 3.18 shows the cracking patterns of the tensile specimens and Figure 3.19 shows the stress versus strain curves for each specimen. The addition of interface elements does not affect the cracking pattern or the displacement at which cracking occurs.

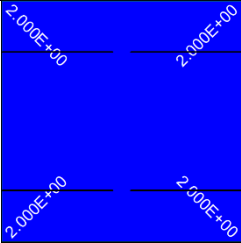
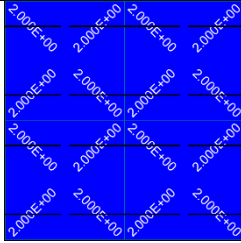
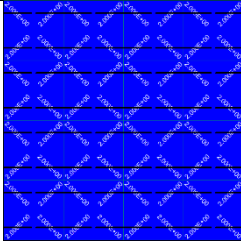
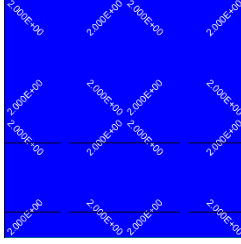
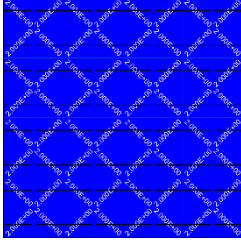
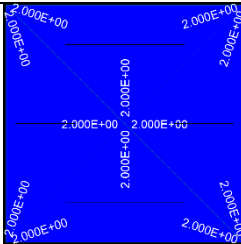
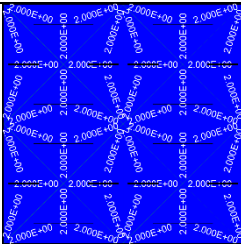
	1x1	2x2	3x3
(N) No Interface Elements			
(H) Perpendicular Interface Elements	N/A		
(I) Diagonal Interface Elements	N/A		

Figure 3.18: Pure tension test cracking patterns

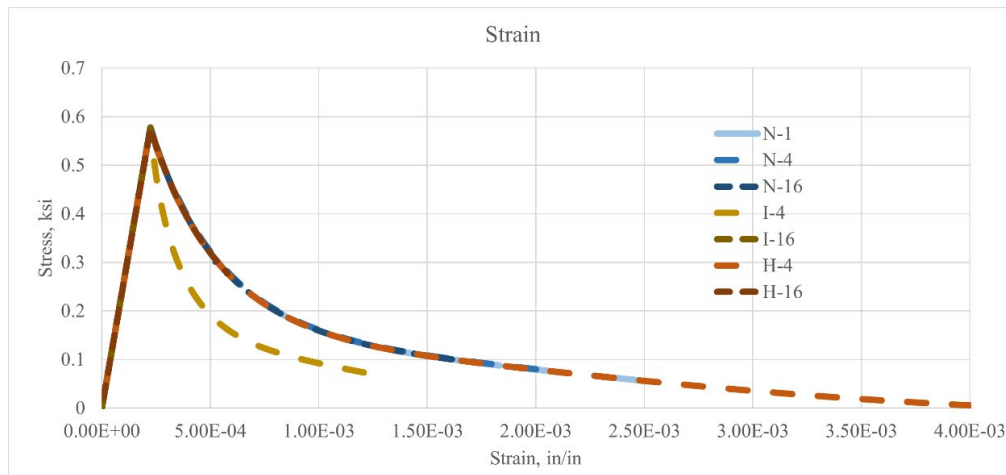


Figure 3.19: Pure tension test stress versus displacement curves*, **

Figure 3.20 shows the crushing pattern of the compression specimens and Figure 3.21 shows the stress versus strain curves of each specimen. The presence of interface elements at the boundaries does not affect the crushing patterns for the specimen or the displacement at which crushing occurs.

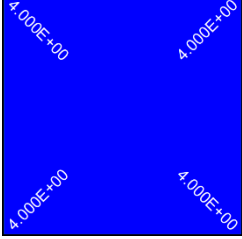
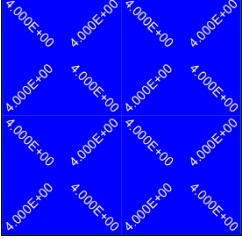
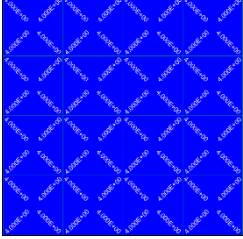
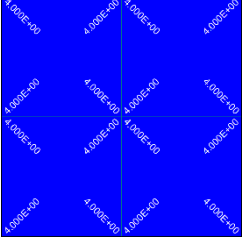
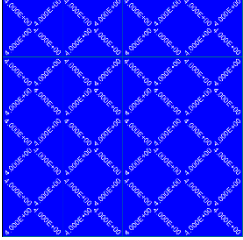
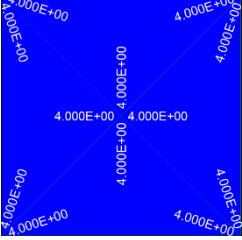
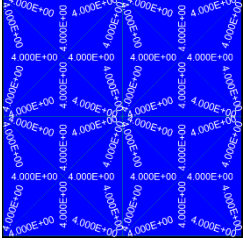
	1x1	2x2	failure3x3
(N) No Interface Elements			
(H) Perpendicular Interface Elements	N/A		
(I) Diagonal Interface Elements	N/A		

Figure 3.20: Pure compression test crushing patterns

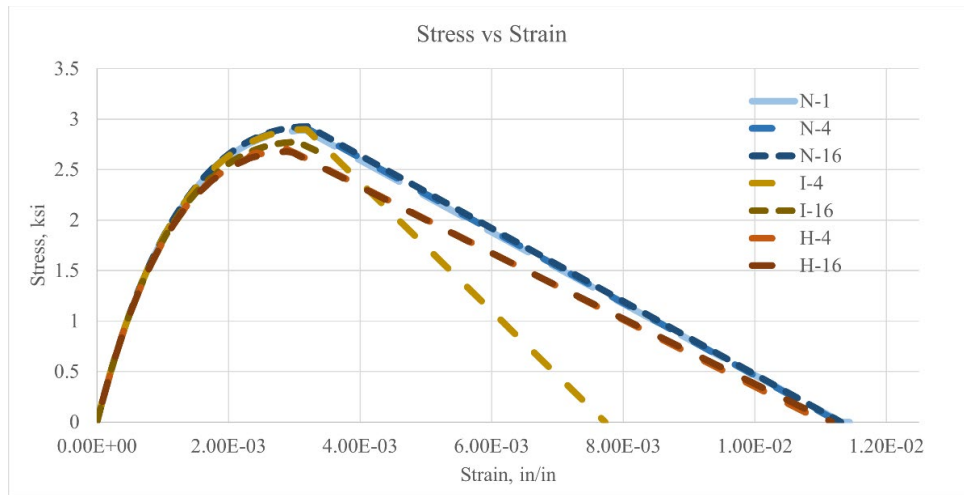


Figure 3.21: Pure compression test versus displacement curves*,**

*16 element models failed at peak stress due to convergence criteria

** The sensitivity of the I-4 models is due to the different characteristic lengths of the smeared crack band elements

Prism Test

Prism tests were modeled to confirm the meshing scheme can accurately represent the tension and compression failures of grouted masonry prisms. The modulus of elasticity, peak strengths and softening was compared against calibrated values. The grouted bed joint stiffness was selected using the estimation explained in the Mortar Interface Elements and Grouted Bed Joint Interface Elements section. The tension test modulus of elasticity was within one percent of the calculated modulus of elasticity and the compression test modulus of elasticity was within five percent of the calculated modulus of elasticity. The peak strength for the tension and compression failures were both within three percent of the expected value. Figure 3.22 shows how the prism test

model performed compared to the expected performance given ATENA's equations. The tension softening was not able to be matched because of failures due to convergence criteria and the compression softening differs due to the localization of the failure into an element with a smaller characteristic length.

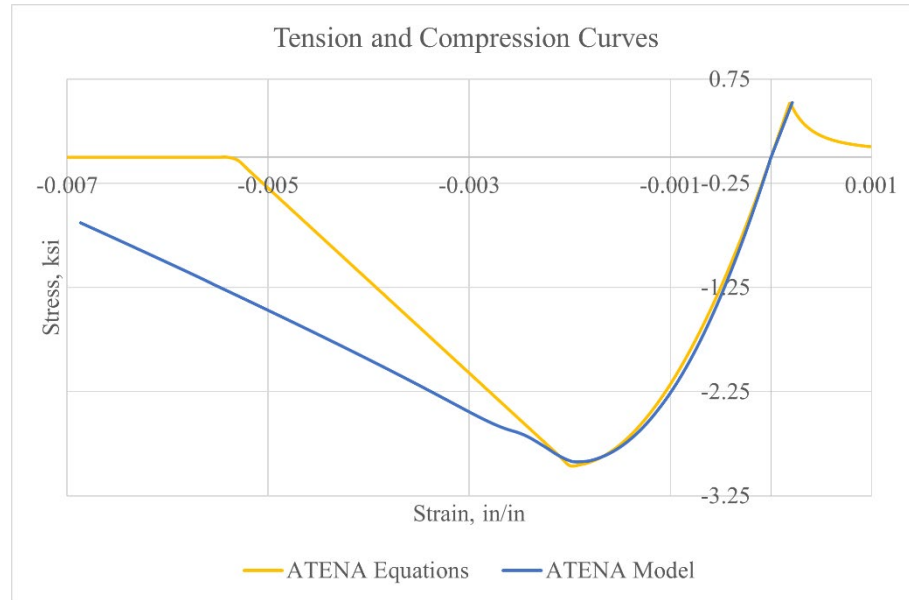


Figure 3.22: Prism tension and compression behavior check

Shear Interface Test

Shear tests were modeled to confirm the meshing scheme can accurately represent the tension and cohesion failures of the prescribed Rankine-type failure criteria with a tension cutoff. Three different modeling schemes were selected to test so the effect of adding diagonal interfaces could be studied. The modeling schemes are shown in Figure 3.23.

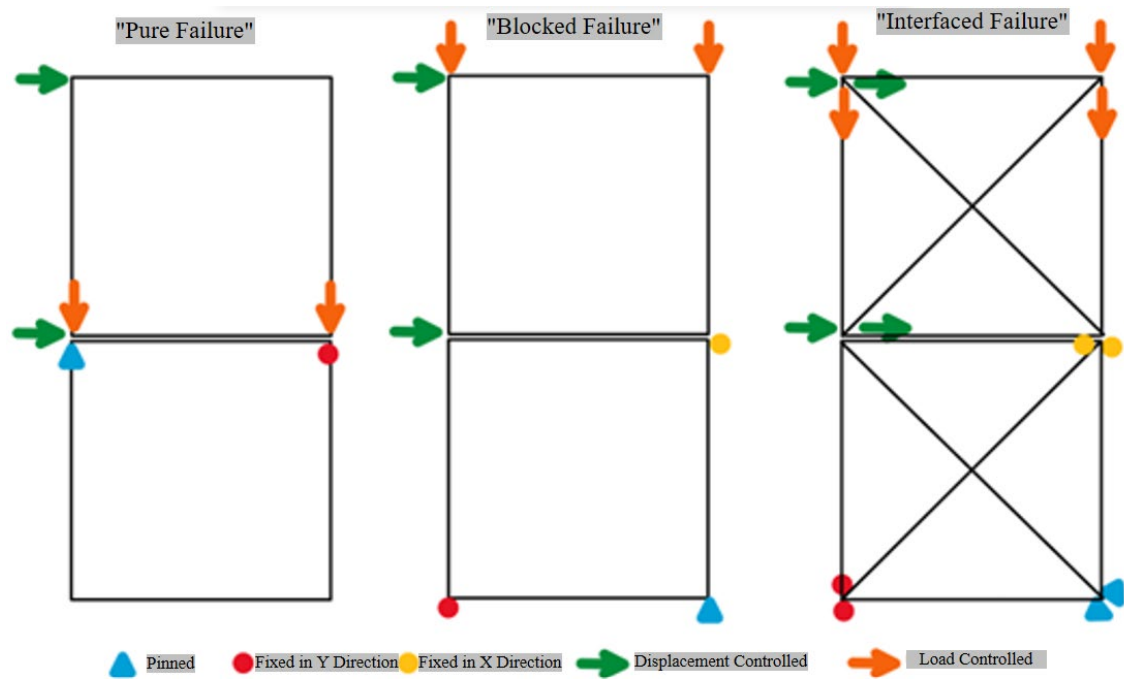


Figure 3.23: Shear modeling schemes

The peak strength before failure for the different modeling schemes are plotted in Figure 3.24 against the prescribed failure criteria. As seen, the failures are minimally by the introduction of diagonal interface elements as compared to the solid block scheme.

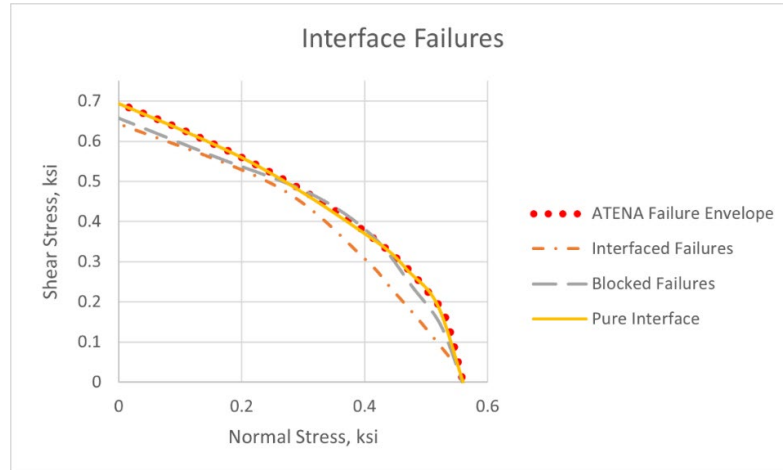


Figure 3.24: Interface failure envelopes

Diagonal Tension Test

The diagonal tension test is based off the test conducted by Shrestha [7] seen in Figure 3.25. This section describes how the parameters of each element were chosen.



Figure 3.25: Diagonal tension test setup [7]

The elastic modulus is calculated using the approximate spring method described previously, where the target prism modulus of elasticity, E_p , was selected based on the lower bound ratio from previous testing from Shrestha [51]. The tensile strength was selected based on ratio of C1019 compression strength to modulus of rupture strengths found by Shrestha on a similar grouted mix. The prism compression strength, f'_m , was found using the strength ratio of the prisms and C1019s tested during Shrestha's diagonal tension test. The fracture energies can be selected from estimates from [35] and tuned if needed. The strain at peak stress has been taken as 0.002 and can be tuned as required. The critical compression displacement has been assumed to be at a strain level of 0.003 but can be tuned as required. Note the fracture energies and critical compressive displacement must be recalibrated depending on the mesh size as mentioned in the Mesh Size Dependence section. The value used and resulting curve of this calibration can be seen in Figure 3.26.

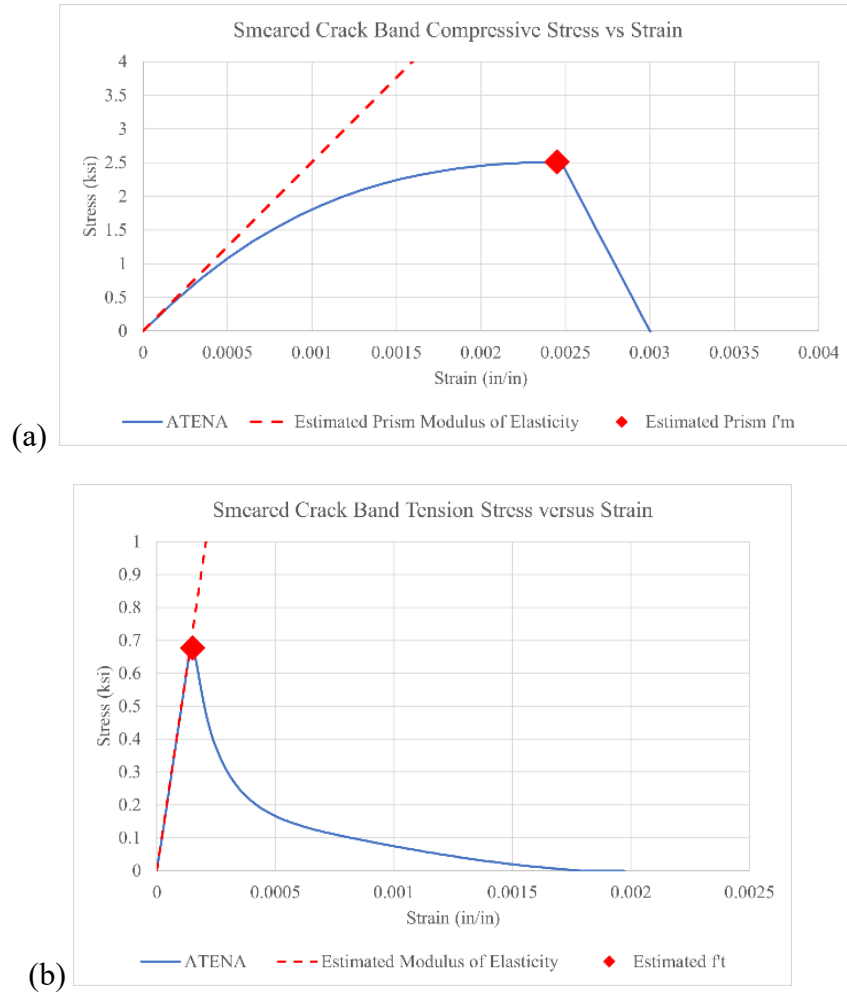


Figure 3.26: Compression Calibration (a) Tension Calibration (b)

The grouted bed joint interface elements normal stiffness was calibrated using the calculation presented in the Mortar Interface Elements and Grouted Bed Joint Interface Elements section. The tangential stiffness was estimated as $\frac{K_{nn}}{2*(1+\nu)}$. The tensile strength was selected based on ratio of C1019 compression strength to modulus of rupture strengths found by [38] on a similar grouted mix. The value used and resulting curve of this calibration can be seen in Figure 3.27

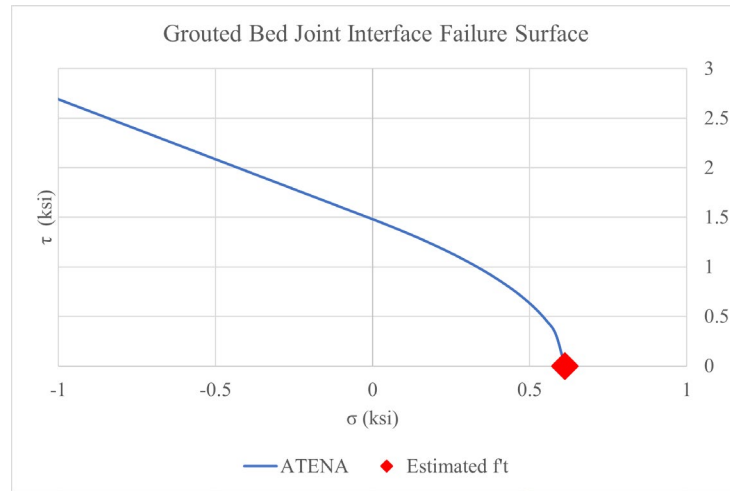


Figure 3.27: Grouted Bed Joint Calibration Curve

The bed and head joint normal stiffnesses were approximated using mortar modulus of elasticity calculated in the Mortar Interface Elements and Grouted Bed Joint Interface Elements section divided by the grouted bed joint length. The tangential stiffnesses were estimated as $\frac{K_{nn}}{2*(1+\nu)}$. The bed joint tensile strength of the mortar was taken as 15 percent of the mortar compression strength. The head joint tensile strength is assumed to be half the bed joint tensile strength due to the poor bond of head joints. The value used and resulting curve of this calibration can be seen in Figure 3.28.

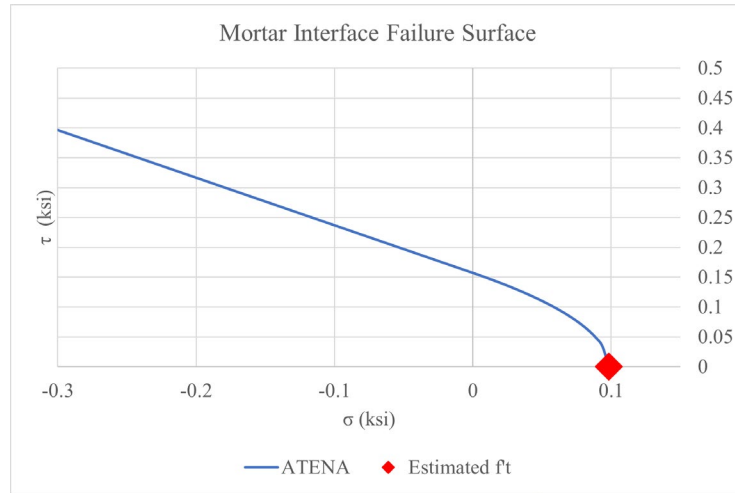


Figure 3.28: Mortar Interface Calibration Curve

The grouted block interface was calibrated according to the smeared crack band properties. The normal and tangential stiffness were set at $2E+4$ kip/in³ to neglect any unwanted elasticity while not ill conditioning the solution. The tensile strength was set the same as the smeared crack band elements. The value used and resulting curve of this calibration can be seen in Figure 3.29.

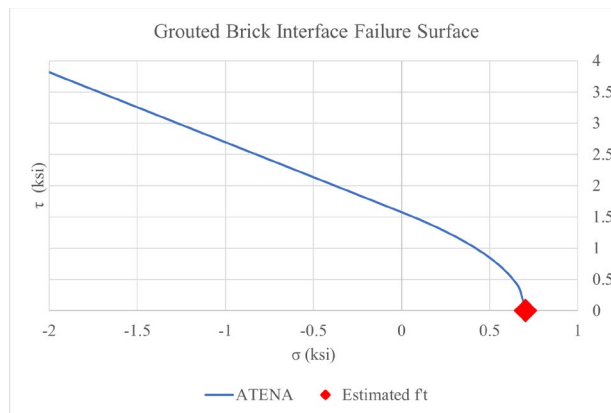


Figure 3.29: Grouted Brick Calibration Curve

The diagonal tension test set up used by Shrestha [7] utilized relief cuts cut diagonally across the test specimen from the support to the loading. Similar properties for

the grouted block were used. The stiffness was scaled down from the values used for the grouted block based on the cut depth. The tensile strength was selected based on ratio of C1019 compression strength to modulus of rupture strengths found by Shrestha on a similar grouted mix and further reduced by a stress concentration factor for a cut notch based on the saw blade width and cut depth. The value used and resulting curve of this calibration can be seen in Figure 3.30.

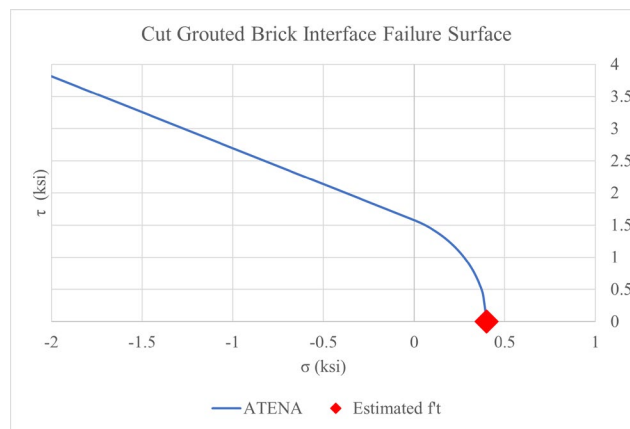


Figure 3.30: Cut Grouted Brick Calibration Curve

For each interface element type the cohesion, friction coefficient, and fracture energies are estimated similarly. They have been initialized using estimates from literature. The fracture energies can be selected from estimates from [35]. Note the fracture energies must be recalibrated depending on the mesh size as mentioned in the Mesh Size Dependence section. While the friction coefficient and cohesion can be estimated from Hamid et. al. and Redmond [28, 52] using Equation Set 3-16. The cohesion should also satisfy the minimum requirement based on ATENA's equations. The failure envelope using ATENA's minimum cohesion should be compared to the failure envelope using the initial estimates. If there is a drastic difference the tensile

strength will be taken as 90% the original value and the friction angle will be reduced so the low compression stress portions of the graphs match.

$$\phi = 0.6 + 0.00015 (f_g, f_m \text{ or } f'_m) \quad c = 65 + 0.015 (f_g, f_m \text{ or } f'_m) \text{ (psi)} \quad \text{Equation Set 3-16}$$

The material properties used in each model is given in appendix C. The cracking patterns of the experiment and the typical cracking of the model before failure due to convergence are shown in Figure 3.31. The primary cracks are shown in red, and the secondary cracks are green. Each model failed when the first cut brick interface cracked. This reflects the brittle behavior of the experiments. The range of shear moduli across the physical tests are compared to the models' shear moduli and listed in Table 3.2. The shear moduli were calculated in accordance with ASTM E519 [22]. The range of peak loads for experimental samples and modeled samples are in Table 3.3.

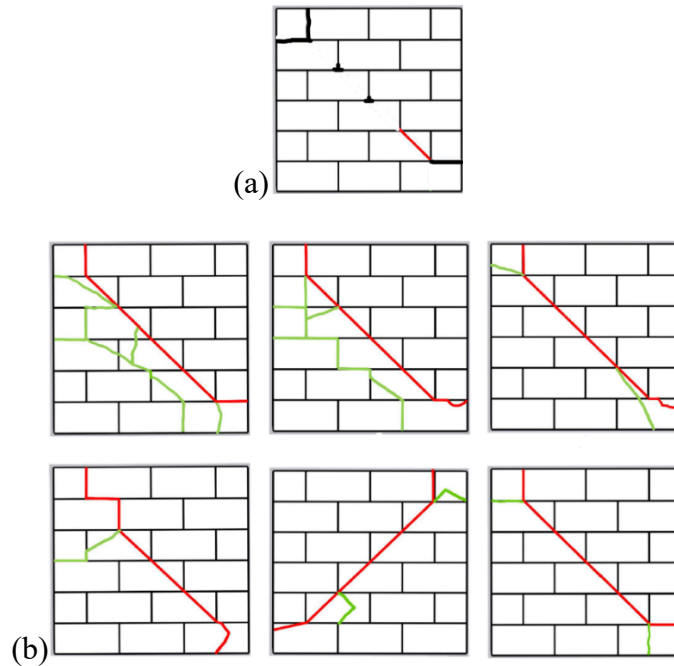


Figure 3.31: Model cracking pattern (a) and experimental cracking patterns [7] (b)

Table 3.2: Shear Modulus Comparison

Sample Type	Shear Modulus (ksi)				
	Model G	Max G	Min G	Max %Δ	Min %Δ
		Exp.	Exp.		
ESST	1666	1583	1306	5.23	27.59
ECST	1497	2042	1021	26.70	46.61

Table 3.3: Peak Load Comparison

Sample Type	Peak Load (kip)						
	Model	Max Load	Avg Load	Min Load	Max	Avg	Min
	Load	Exp.	Exp.	Exp.	%Δ	%Δ	%Δ
ESST	84.0	93.0	81.4	67.5	9.67	3.20	24.45
ECST	68.1	85.3	73.6	57.6	20.21	7.48	18.16

Summary

The modeling scheme, element formulation and material calibration process have been described in detail. The validation studies show that the modeling scheme proposed yield consistent results with previous masonry assemblies with LW grout for pre-peak and peak behavior.

The pure compression, tension, and shear tests show that the modeling scheme proposed has a negligible effect on the overall material behavior of the model with respect to failure of the element. The material calibration process outlines experimental tests and approximations from literature that reasonably capture the material properties of

masonry assemblies. The results from the diagonal tension tests indicated that the proposed meshing scheme and material calibration are capable of capture overall pre-peak system behavior including stiffness, peak load, and initial failure patterns.

The results of the validation studies confirm that the constitutive model is appropriate to model the behavior of masonry assemblies with LW grout.

CHAPTER FOUR

TRIPLET TESTS

Statement of Contribution

The following work presented is the collaborative effort of Hannah Kessler, Cooper Banks, and Dr. Laura Redmond. The contribution of Cooper Banks includes the analytic analysis of the failure patterns and the finite element modeling of the expanded clay (EC) and expanded slate (ES) triplet tests. All experimental work was conducted by Hannah Kessler.

Introduction

The shear strength of grouted masonry bed joints depends on two factors: cohesion and shear friction. Cohesion is the strength of the bed joint under no compression load and is dependent on the mortar and grout bond characteristics. Shear friction is the additional strength a joint gains when a compressive load acts perpendicular to it. The shear strength of grouted masonry joints has been shown to increase with increasing compressive load [52; 53]. Because the shear strength of these joints is inherently dependent on the tensile properties of the grout, a similar reduction factor may be needed on the predicted shear capacity of joints using lightweight grout. In the TMS 402/602-22 code, the shear strength of fully grouted masonry bed joints laid in running bond is determined according to its respective equation from Table 9.2.6.1, this equation is reproduced following as equation set 4-1.

$$V_n = 90A_{nv} + 0.45P_u \quad (V_n = 0.620A_{nv} + 0.45P_u)$$

Equation Set 4-1

Where

V_n = nominal shear strength of the bed joint in lb (N)

A_{nv} = shear area of the bed joint in in² (mm²)

P_u = force normal to the bed joint in lb (N)

Previous Shear Strength Tests on Grouted Masonry bed joints

Two studies were identified in the literature that have tested the shear strength of grouted masonry bed joints with and without additional normal compression stresses. The first, conducted by Hamid et al. [52], tested grouted masonry assemblies that used two different types of normal weight grout: one termed “weak,” with a compressive strength of 2080 psi (14.3 MPa), and one termed “strong,” with a compressive strength of 5350 psi (36.9 MPa). Specimens of each grout type were tested at three different levels of normal compression stress: 0 psi (0 MPa), 100 psi (0.7 MPa), and 200 psi (1.4 MPa). All specimens were made with mortar with a compressive strength of 3110 psi (21.4 MPa), a nominal joint thickness of 0.375 in (0.953 cm), and blocks with compressive strength of 2850 psi (19.7 MPa). The grout type, number of specimens tested, normal compression stress, and average shear strength of each set of specimens is shown in Table 4.1.

Table 4.1: Grout type, number of specimens tested, normal compression stress, and average shear strength of specimens from Hamid et al. [52]

Grout Type	Number of Specimens	Normal Compression Stress, psi (MPa)	Shear Strength, psi (MPa)
Weak	4	0 (0)	106 (0.7)
	3	100 (0.7)	237 (1.6)
	4	200 (1.4)	331 (2.3)
Strong	4	0 (0)	153 (1.1)
	4	100 (0.7)	316 (2.2)
	3	200 (1.4)	416 (2.9)

Hamid et al. noted that the failure mode of the specimens was consistently a “shear-slip” failure at the mortar joints. They also noted that precompression significantly increased the shear capacities of the grouted masonry joints.

The second set of studies [28, 53] tested grouted masonry assemblies in shear using a procedure adapted from DIN EN 1052-3, the German version of a European standard that dictates test methods for determining the shear strength of masonry assemblies. The shear triplet specimens from this study used grout made with normal weight aggregates (batched by ASTM C476 requirements for proportions), lightweight masonry units, and mortar made with type M Portland cement-lime mortar. The average 28-day compressive strengths of the grout and mortar were 3050 psi (21.0 MPa) and 4430 psi (30.5 MPa), respectively. The compressive strength of the CMU blocks used was 1700 psi (11.7 MPa). Three specimens were tested at three different levels of normal compression stress, 0 psi (0 MPa), 50 psi (0.4 MPa), and 100 psi (0.7 MPa). The normal

compression stress, number of specimens, and average shear strength are shown in Table 4.2.

Table 4.2: Normal compression stress, number of specimens, and average shear strength of shear triplets tested by Redmond et al. [53]

Normal Compression Stress, psi (MPa)	Number of Specimens	Average Shear Strength, psi (MPa)
0 (0)	3	77.6 (0.54)
50 (0.4)	3	190.8 (1.32)
100 (0.7)	3	194.7 (1.34)

They proposed equation set 4-2 with a cohesion of 110 psi (0.76 MPa) and shear friction coefficient of 1.07 as a relation between direct shear strength (ν) and normal compressive stress (f_a) based on the experimental results of Hamid et al. and validated on their experimental data.

$$\nu = 110 \text{ psi} + 1.07 f_a \quad (\nu = 0.76 \text{ MPa} + 1.07 f_a) \quad \text{Equation Set 4-2}$$

Redmond et al. also compared the results of their tests with the predictions of TMS 402/602-16 equation 9.2.6.1 (e), which is the same as equation set 4-1 from the TMS 402/602-22 code. The results of their 50 psi and 100 psi normal compression groups fell well above the predicted values from the TMS equation. The results of their 0 psi normal compression group fell close to or slightly below the predicted values from the TMS equation, see Figure 4.6.

EXPERIMENTAL PROGRAM

Grout Mix Design

There is not currently an ASTM standard applicable to grouts using lightweight aggregates. As such, the ASTM C476-19 requirements of a minimum compressive strength of 2000 psi (13.8 MPa) at 28-days and a slump between 8 to 11 inches (20.3 to 27.9 cm) were used to formulate the mix designs for the lightweight grouts tested in this work. Three different lightweight grout mix designs were developed using two different lightweight aggregates, one using fine and coarse expanded clay (EC) aggregate and two using fine and coarse expanded shale (ES) aggregate. The density properties, specific gravity, absorption, and gradation properties of the coarse and fine aggregates are shown in Table 4.3 [54].

Table 4.3: Density properties, specific gravity, absorption, and gradation of the EC coarse and fine aggregates and ES coarse and fine aggregates

Physical Property	EC Coarse	EC Fine	ES Coarse	ES Fine
Relative Density (OD)	0.92	0.88	1.44	1.75
Relative Density (SSD)	1.17	1.35	1.55	2
Specific Gravity (SG)	1.17	1.35	1.55	2
Absorption (%)	27.49	52.68	7.87	14.5
Gradation				
Sieve Size	Cumulative % weight by passing			
1/2 in	100	100	100	100
3/8 in	100	100	97.4	100
#4	30.6	100	9.3	100
#8	2.1	69.8	6.9	93.4
#16	1.3	43.6	5.8	41.9
#50	0.8	13.9	5.3	23.8
#100	0.5	9.8	4.9	10.4
#200	0.2	-	2.8	-

Though two batches of grout using EC aggregates were prepared, the first batch had workability issues that led to poor quality specimens. The second batch of EC specimens were prepared using the mix design of Shrestha et al. [7]. Based on the consistency of the shear behavior of the EC grout in wall assemblies in their testing, it was deemed that one batch of EC specimens would be sufficient for this initial test program.

Because lightweight aggregates are generally more porous than normal weight aggregates, it is necessary to soak them in water for a period of 72 hours to ensure that they are fully saturated before they are added to the mix (ASTM C127-15 and ASTM C128-15). The coarse aggregates were brought to the saturated surface dry condition (SSD) before they were added to the mix through a combination of hand drying using paper towels and a heat gun. Ideally, both the fine and coarse aggregates would have been added to the mix in the SSD condition, but the process for bringing the fine aggregates to the SSD condition was especially time intensive. Because of this, the free water content of the aggregates was calculated by removing a sample, approximately 5 lb (22.2 N) in weight, drying it to the SSD condition, weighing the SSD sample, and then subtracting the SSD weight from the starting (wet) weight. The amount of water added to the mix was the adjusted down to compensate for the percentage of free water present in the fine aggregates.

Previous work using the same lightweight aggregates by Shrestha et al. [54] found that mix designs that met the ASTM C476 volume proportion requirements had segregation issues that made them unusable. The components of mix designs using lightweight aggregates that instead followed the ACI 213R-14 design procedure remained integrated, so this procedure was used for the mix designs for this work. The as-batched volume proportions (using the bulk density of the materials and the specific gravity of concrete equal to 3.15), water to cement ratios by weight, and slumps of the three mix designs are shown in Table 4.4. The EC Mix used EC aggregates and ES-1 and ES-2 used ES aggregates.

Table 4.4: The as-batched volume proportions, water-to-cement ratios by weight, and slumps of the three mix designs

Mix Design	Volume Proportion			Water-to-Cement Ratio by Weight	Slump, in (cm)
	Cement	Fine Aggregates	Coarse Aggregates		
EC	1.00	1.08	0.48	0.31	8 (20.3)
ES-1	1.00	1.08	0.48	0.24	8 (20.3)
ES-2	1.00	1.08	0.48	0.34	8.5 (21.6)

Unit, Grout, and Mortar Strengths

Lightweight concrete masonry units (CMU) were donated by a local block producer for this work. These units were nominal 8” half blocks, some with a single split face. The compressive strengths of four ungrouted half blocks were tested using the testing apparatus and loading procedure described in ASTM C1314-18. The average net compressive strength, f_{mt} , of these blocks was 1790 psi (12.3 MPa) with a standard deviation of 361 psi (2.5 MPa).

Grout prisms were formed using molds formed from masonry units per ASTM C1019-19. Three prisms were formed for each of the three mix designs. All prisms were tested in compression at 28 days except for one from the ES-1 mix which was tested at 26 days. The two ES-1 prisms that were tested on day 28 showed a significant strength increase, so the result from the prism tested at day 26 was discarded. The number of specimens tested, the average 28-day grout compressive strength (f_g), and standard deviation for each mix design is shown in Table 4.5. The average grout compressive

strength for each mix design exceeded the minimum requirement of 2000 psi (13.8 MPa) from ASTM C476-19.

Table 4.5: Number of specimens tested, average 28-day grout compressive strength, and standard deviation for each mix design

Mix Design	Number of Prisms Tested	Average Grout Compressive Strength, f_g, psi (MPa)	Standard Deviation, psi (MPa)
EC	3	2970 (20.5)	240 (1.7)
ES-1	2	4700 (32.4)	40 (0.3)
ES-2	3	5160 (35.6)	990 (6.8)

The mortar for joining the masonry units was made using masonry sand, Type S mortar cement, and water in accordance with the proportion specifications in ASTM C270-19a. Approximately the same proportions of each of the mortar components were used in each of the three batches of mortar. At the time each batch of mortar was mixed, six 2 in (5.08 cm) mortar cubes were created in accordance with ASTM C109-16a. The mortar cubes were left in their molds in a moist room for 24 hours and were then demolded and allowed to wet cure for another 27 days. The number of specimens tested, the average 28-day mortar compressive strength (f_m), and standard deviation for each mortar batch (related to their corresponding grout batch) are shown in Table 4.6.

Table 4.6: Number of specimens tested, average 28-day mortar compressive strength, and standard deviation for each batch of mortar

Grout Batch	Number of Mortar Cubes Tested	Average Mortar Compressive Strength, f_m , psi (MPa)	Standard Deviation, psi (MPa)
EC	6	1130 (7.8)	300 (2.1)
ES-1	6	1310 (9.0)	190 (1.3)
ES-2	6	1350 (9.3)	170 (1.2)

Shear Triplet Testing

DIN EN 1052-3 is a standard published by the European Committee for Standardization for determining the initial shear strength of horizontal masonry bed joints. Specimens are typically composed of three masonry units and two mortar joints. The outer units are placed on supports that allow free rotation while the shear load is applied to the suspended middle joint and the normal compression force is applied longitudinally to the specimen. The typical setup for this test is shown in Figure 4.1, where V is the shear force applied to the specimen and N is the normal compression force applied to the specimen.

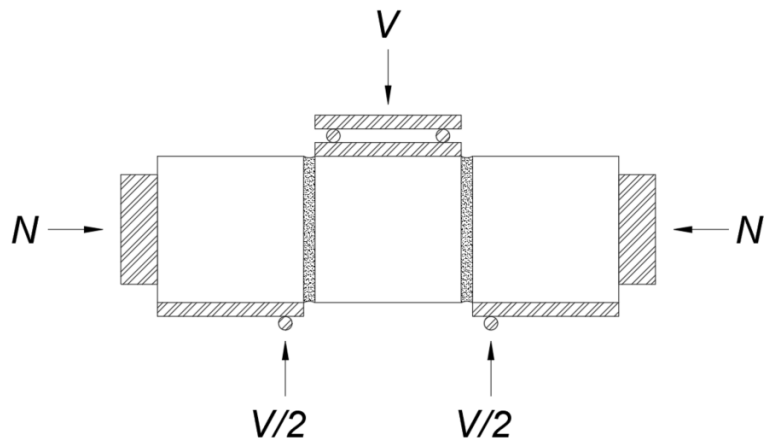


Figure 4.1: Typical test setup per DIN EN 1052-3 [42]

Annex A of DIN EN 1052-3 describes four different types of failures that typically occur in these tests. Mode A.1 is a shear failure in the unit and mortar bond area either on one face or divided between the two unit faces. Mode A.2 is a shear failure only in the mortar. Mode A.3 is a shear failure only in the unit. Mode A.4 is a crushing and/or splitting failure in the units that crosses the mortar joint. Figure 4.2 shows these four failure modes.

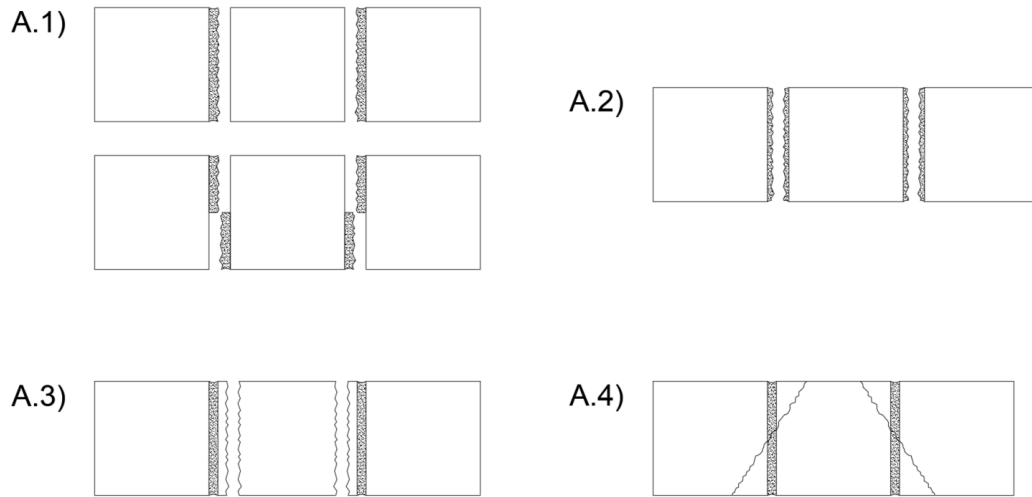


Figure 4.2: Failure modes described by DIN EN 1052-3 [42]

The following apparatus (Figure 4.3) was designed to execute masonry shear triplet tests in a procedure adapted from EN 1052-3. Care was taken to ensure that the shear and normal loads were distributed as uniformly as possible by using 0.5 in (1.27 cm) thick and 1.25 in (3.18 cm) thick steel plates to transfer the loads into the specimen. Additionally, neoprene rubber mats were placed between the steel transfer plates and the specimen to ensure a uniform contact surface. The plate that transferred the normal compression load was allowed to translate along the threaded rods with as little friction as possible by providing bearings between the plate and rods made of ultra-high molecular weight polyethylene, which has a low coefficient of friction.

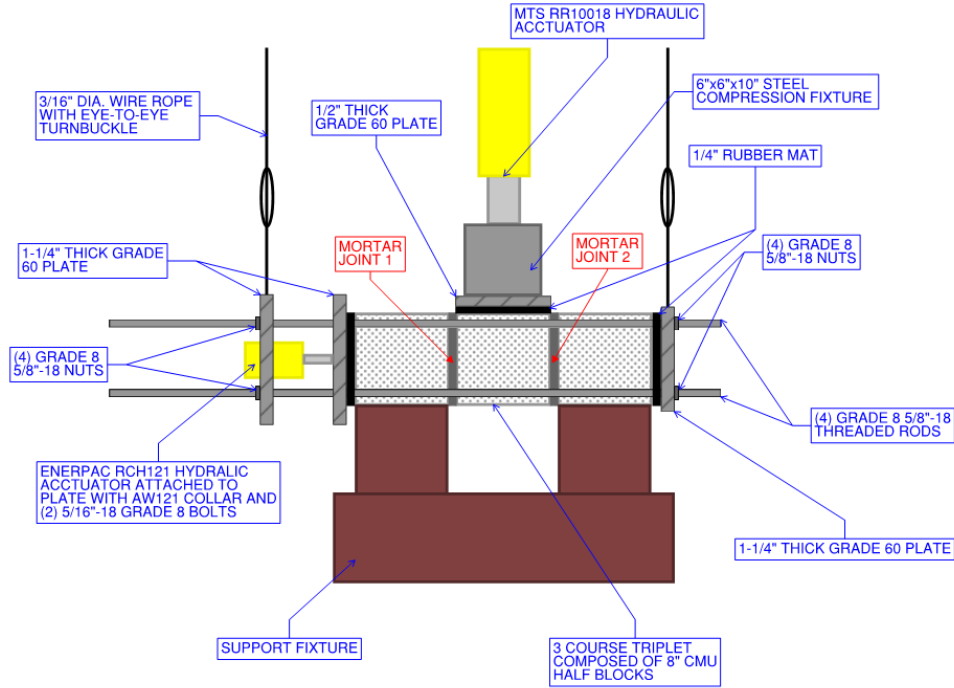


Figure 4.3: Apparatus for testing masonry triplets under shear and normal compression loads

Six shear triplets were fabricated for each mix design using the following procedure. First, three half blocks were mortared together using the Type S mortar described previously to produce two joints with nominal thicknesses of 0.375 in (0.953 cm). These mortar joints were allowed to cure for 3 weeks before the grout was poured. Next, the grout was mixed and poured into the block voids. The grout was poured in three lifts, the first up to the height of the first mortar joint, the second up to the height of the second mortar joint, and the third up to the full height of the specimen. The grout was tamped 25-30 times between each lift using a tamping rod. The grout was leveled at the full height of the specimen using a trowel. The grouted triplets were allowed to cure covered with plastic bags for 28 days.

The shear triplets were tested at three different normal compression loads, 50 psi (0.35 MPa), 100 psi (0.69 MPa), and 150 psi (1.03 MPa). Two shear triplets of each mix type were tested at each normal compression level. The specimens were named according to their mix design, specimen number (from 1 to 6), and normal compression value (in psi); for example, “EC_1_50” is specimen 1 that used the EC grout mix and was tested using a normal compression of 50 psi (0.35 MPa).

First, the normal compression was applied using the RCH121 Enerpac actuator shown in Figure 4.3. The normal compression load was maintained within a margin of $\pm 2\%$ for the duration of the test by monitoring the pressure displayed on the gauge and increasing it using the hand pump as necessary. Second, shear force was applied to the assembly at a rate between the bounds specified by the EN 1052-3 standard of 14.5 to 58.0 psi/min (0.1 to 0.4 MPa/min) using the Enerpac RR10018 actuator. The triplets were considered failed after the shear load began to drop rapidly and load could not be regained.

Results

Failure Modes

Two predominant failure modes were observed from testing. The predominate failure mode consisted of a crack initiating at the joint as shown in Figure 4.4. The crack opened approximately one-third to one-half the height of the block where it then progressed into the center block at an angle of approximately 45-degrees.



Figure 4.4: Mode 1 failure – combined joint and unit failure (a) before triplet blocks were separated and (b) after triplet blocks were separated

The inclined cracks in the failure modes may be explained by the imperfections of the manual loading. During the pauses between each loading pump, the stress has an opportunity to redistribute to the uncracked cross section. The finite element models mentioned later, failed along the bed joint only, due to the constant rate of loading. However, they were not able to reach convergence in the post peak beyond the point where the lower half of the joint breaks. The finite element models were used to confirm the failure was initiated due to shear failure of the grouted bed joint. If additional shear tests are conducted in the future, it is advisable to use a servo-controlled actuator to maintain a smoother loading profile.

Four of the eighteen specimens failed in an odd manner consisting of longitudinal splitting of the face shell and face shell spalling, followed by grout failure as shown in Figure 4.5. In this failure mode longitudinal cracks were first visible at the top of the

triplet specimen. These longitudinal cracks then caused the outer face shell on the center block to spall off. The removal of the face shell typically revealed approximately 45-degree cracks through the grout core. This failure mode was not similar to any described in DIN EN 1052-3.



Figure 4.5: Mode 2 failure – longitudinal splitting and face shell spalling followed by grout failure (a) before triplet blocks were separated and (b) after triplet blocks were separated.

A list of the specimens and their respective failure modes is presented in Table

4.7.

Table 4.7: Shear triplet specimens, their normal compression stress values, and their failure modes.

Normal Compression Stress, psi (MPa)	EC Specimens		ES-1 Specimens		ES-2 Specimens	
	Specimen	Failure Mode	Specimen	Failure Mode	Specimen	Failure Mode
50 (0.35)	EC_1_50	Mode 1	ES-1_1_50	Mode 1	ES-2_1_50	Mode 1
50 (0.35)	EC_2_50	Mode 1	ES-1_2_50	Mode 1	ES-2_2_50	Mode 1
100 (0.69)	EC_3_100	Mode 2	ES-1_3_100	Mode 1	ES-2_3_100	Mode 2
100 (0.69)	EC_4_100	Mode 2	ES-1_4_100	Mode 1	ES-2_4_100	Mode 1
150 (1.03)	EC_5_150	Mode 1	ES-1_5_150	Mode 1	ES-2_5_150	Mode 1
150 (1.03)	EC_6_150	Mode 2	ES-1_6_150	Mode 1	ES-2_6_150	Mode 1

The mode 1 failures that deviate slightly from a pure interface failure are likely due to the non-constant loading induced by the manual pump in the test set up and align well with model predictions of the shear failures. Note that the ES specimens very consistently exhibited these failures. However, the EC specimens only exhibited the expected failure (Mode 1) about half the time. Because these specimens were prepared by undergraduates as part of an educational program some of these may be due to fabrication issues. However, if the equations presented in the EN 1052-3 do not perfectly represent the failure mechanism observed in the masonry assemblies, EN 1052-3 states “the result may be used as a lower bound strength for each compression level” (DIN EN 1052-3) as the observed failure mechanism governed the capacity.

Shear Strength Results

The normal stress vs. shear stress at failure and relevant specimen properties for each of the EC, ES-1, and ES-2 specimens are summarized in Table 4.8.

Table 4.8: Normal stress vs. shear stress at failure and relevant specimen properties for each of the EC, ES-1, and ES-2 specimens

Specimen Name	Grout Type	Grout Compressive Strength, psi (MPa)	Normal Stress, psi (MPa)	Tested Shear Stress, psi (MPa)	TMS Equation Predicted Shear Stress, psi (MPa)	Tested/Predicted Shear Stress
EC_1_50	LW, EC	2970 (20.48)	50.1 (0.35)	86.5 (0.60)	112.5 (0.78)	0.77
EC_2_50	LW, EC		49.0 (0.34)	108.6 (0.75)	112.1 (0.77)	0.97
EC_3_100	LW, EC		102.9 (0.71)	124.0 (0.86)	136.3 (0.94)	0.91
EC_4_100	LW, EC		101.9 (0.70)	118.0 (0.81)	135.9 (0.94)	0.87
EC_5_150	LW, EC		155.5 (1.07)	125.2 (0.86)	160.0 (1.10)	0.78
EC_6_150	LW, EC		153.7 (1.06)	87.6 (0.60)	159.2 (1.10)	0.55
ES-1_1_50	LW, ES	4700 (31.41)	49.8 (0.34)	128.6 (0.89)	112.4 (0.78)	1.14
ES-1_2_50	LW, ES		45.5 (0.31)	93.5 (0.65)	110.5 (0.76)	0.85
ES-1_3_100	LW, ES		104.3 (0.72)	121.5 (0.84)	136.9 (0.94)	0.89
ES-1_4_100	LW, ES		101.9 (0.70)	136.0 (0.94)	135.9 (0.94)	1.00
ES-1_5_150	LW, ES		148.7 (1.03)	140.6 (0.97)	156.9 (1.08)	0.90
ES-1_6_150	LW, ES		155.6 (1.07)	155.4 (1.07)	160.0 (1.10)	0.97
ES-2_1_50	LW, ES	5160 (35.58)	48.0 (0.33)	126.3 (0.87)	111.6 (0.77)	1.13
ES-2_2_50	LW, ES		48.4 (0.33)	108.9 (0.75)	111.8 (0.77)	0.97
ES-2_3_100	LW, ES		99.3 (0.69)	162.0 (1.12)	134.7 (0.93)	1.20
ES-2_4_100	LW, ES		104.5 (0.72)	148.6 (1.03)	137.0 (0.95)	1.08
ES-2_5_150	LW, ES		155.0 (1.07)	167.8 (1.16)	159.8 (1.10)	1.05
ES-2_6_150	LW, ES		152.4 (1.05)	174.1 (1.20)	158.6 (1.09)	1.10

Figure 4.6 plots the results of the LW specimens compared to the tests of Hamid et. al. [52] and Redmond et al. [53] along with the TMS 402/602-22 code specified strength equation set 4-1, and best fit lines for the trends from each LW specimen set. In general, the lightweight (LW) grout specimens from the EC and ES-1 mixes were lower than or equal to the prediction of equation set 4-1 from TMS 402/602-22. The LW grout specimens from the ES-2 mix were generally very close to or above the prediction of the TMS equation. The shear strength from Redmond et al. and Hamid et al.'s tests on normal weight (NW) grout specimens were generally much greater than the prediction of the TMS equation.

To determine the cohesion values and shear friction coefficients for the EC and ES aggregate types, lines of best fit were generated for each and plotted against the experimental datasets for the EC and ES triplets and the NW triplets from Hamid et al. and Redmond et al. (Figure 4.6). The specimens tested by Redmond et al. [53] at 0 psi (0 MPa) normal compression were excluded because of the low break at approximately 50 psi, a little over half of the strength of the other two specimens. Additionally, including these much lower strength results would have made the methodology for determining the reduction factors, described following, unconservative. Specimen EC_6_150 was discarded from the EC dataset because it had a shear strength significantly lower than EC_5_150 and less than the average of the EC_1_50 and EC_2_50.

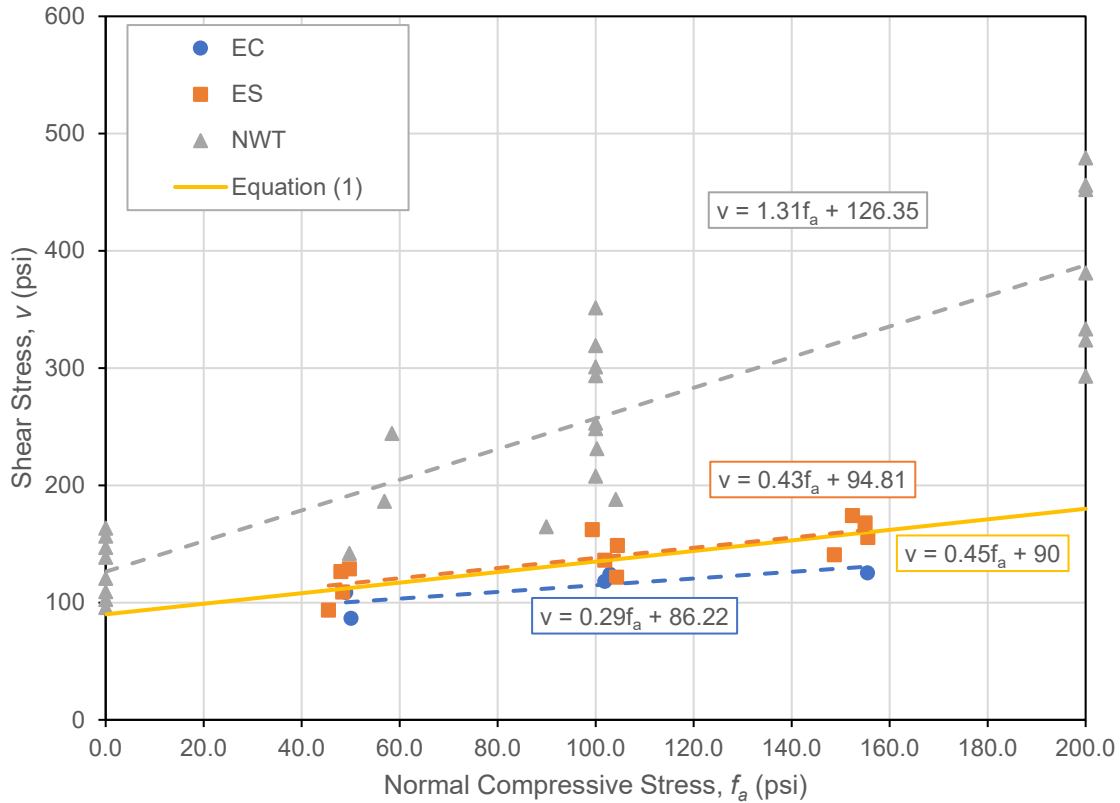


Figure 4.6: Lines of best fit, showing cohesion value and shear friction coefficients, for EC and ES aggregates plotted against normal weight (NW) experimental data and equation set 4-1 from TMS 402/602-22

The EC and ES aggregate grouts had similar cohesion values (86.22 psi (0.60 MPa) and 94.81 psi (0.65 MPa), respectively), but slightly different shear friction coefficients (0.29 and 0.43, respectively). The cohesion value and shear friction coefficient fit to the NW specimens of Hamid et al. and Redmond et al. were 126.35 psi (0.87 MPa) and 1.31, respectively. The cohesion value from equation set 4-1 from TMS 402/602-22 of 90 psi (0.621 psi) is close to the values from the lines of best fit for the EC and ES specimens.

Finite Element Model of the Tests

Beam theory assumptions do not apply for the test setup used, so a finite element model is used to determine the stress distribution across the bed joint of the triplet specimen. The stress distribution is used to determine that the failure of the test setup presented in Figure 4.3 is dominated by the shear strength of the assembly. The model was constructed in ATENA 2D using an array of 4 triangular smeared crack elements jointed by interface elements (shown in Figure 4.7) to properly capture potential shear cracking of the masonry. The boundary conditions of the model are also shown in Figure 4.7.

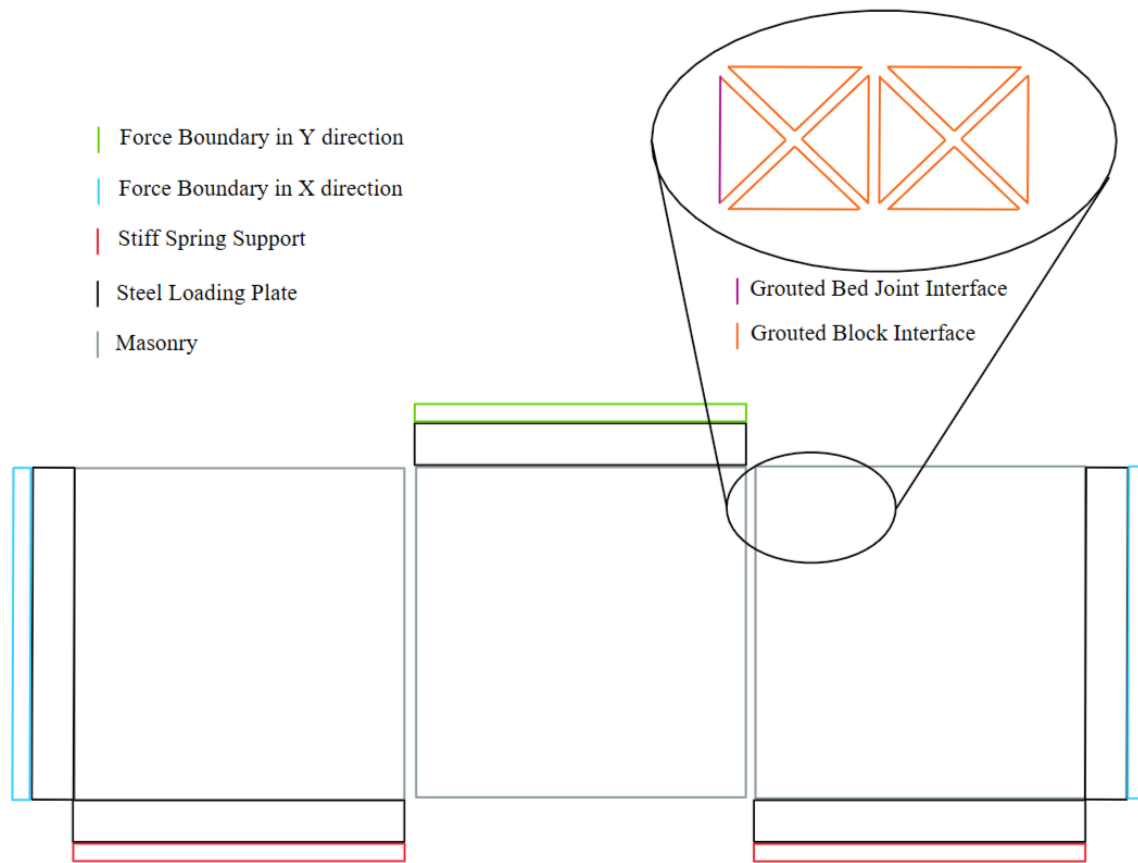


Figure 4.7: Finite element modeling scheme and boundary conditions

This follows the same smeared-crack and interface element module leveraged by Stravidis and Shing, Redmond et. al. and Redmond et. al. [27, 55, 56] for modeling reinforced concrete within masonry infill structures that may be subjected to shear failure. The boundary conditions considered replicate the proposed test set up. Note the maximum deflection of the stiff spring support, representing the neoprene, is on the magnitude of 1E-02 inches and the boundary does not carry any tension loads. This support is used to model the load redistribution effect of a layer of neoprene. The finite element models consisted of three element types: the smeared crack band elements, the grouted block interface elements, and the grouted bed joint interface

elements. The EC and ES models were calibrated assuming a grout strength of 2.97 ksi and 4.7 ksi respectively. The material parameters of each element are chosen based on similar grout mixes used by Shrestha et al. and Banks et al. [7, 38].

Masonry Prism Compression Behavior

The prism compression strength, f'_m , is found using the strength ratio of the prism strength, f'_m , over the C1019 strength, f_g , tested during Shrestha's diagonal tension test. The ratio from Shrestha's tests on similar grout is 84.5%. The elastic modulus of the smeared crack band elements is calculated by idealizing the grouted block and grouted bed joint as a system of springs in series, where the target system stiffness is selected based on the lower bound ratio from previous testing from Shrestha [51]. The detailed calculations can be found in appendix A. The prism modulus of elasticity is initialized as $947 * f'_m$. This approximation is slightly larger than $900 * f'_m$ that is presented in table 4.2.2 in TMS402/602 code. The critical compression displacement is assumed to be at a strain level of 0.003. The resulting compression stress vs. strain curves for the EC and ES models are found in Figure 4.8.

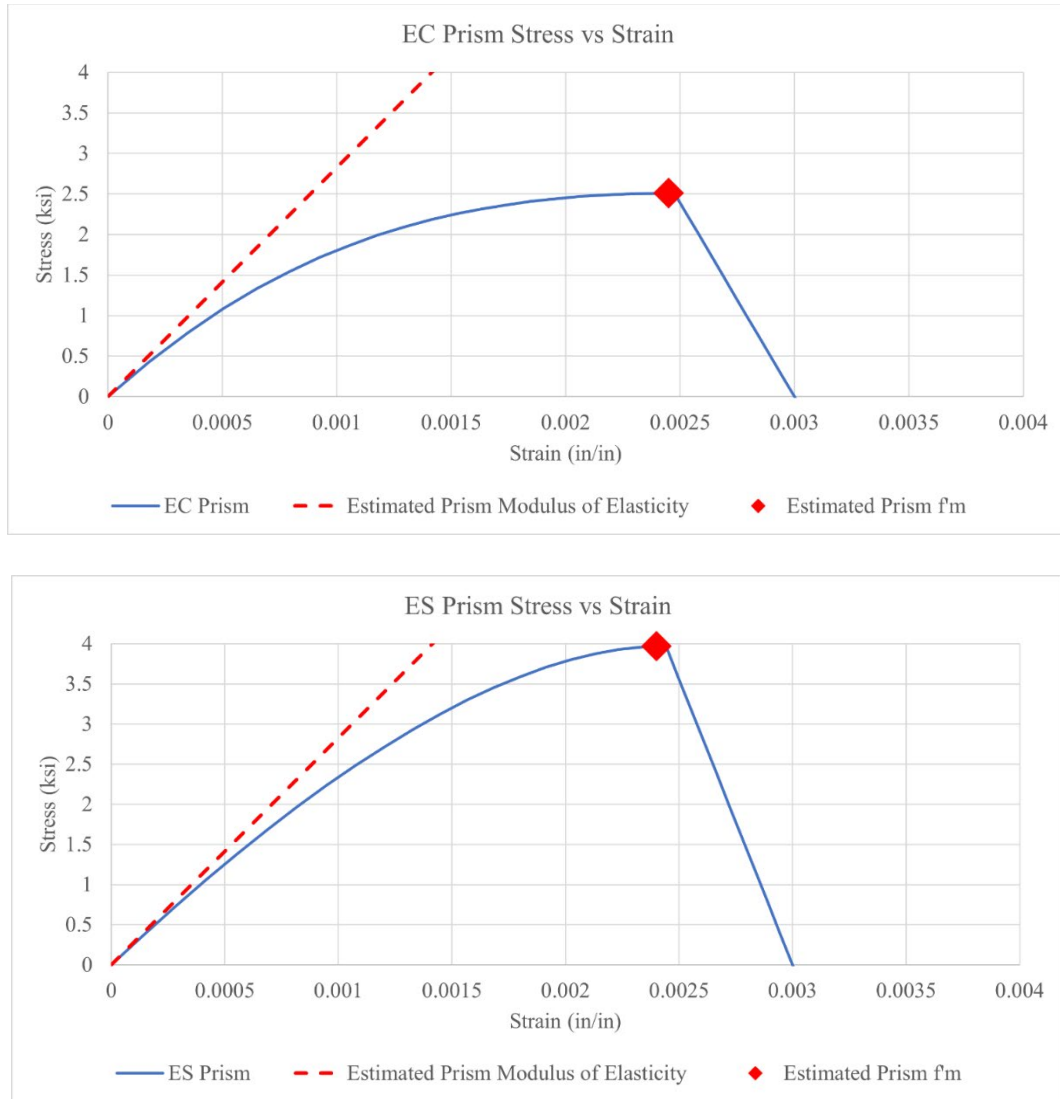


Figure 4.8: Prism Compression stress versus strain curves

Masonry Tension and Shear Behavior

The tensile strength of the masonry through the grouted block region is assumed to be dominated by the grout behavior. The smeared crack band element tensile strength is selected based on ratio of C1019 compression strength to modulus of rupture strengths of 15% found by Shrestha on a similar grout mix design [51]. The stiffness is through the

idealized series of springs method mention previously. The fracture energies are selected as, 1.76E-03 kip/in, the average estimates from Hillerborg for concrete of compressive strengths between 1.5ksi to 6.5ksi [35]. The strain at peak stress is taken as 0.002. Note the facture energies and critical compressive displacement must be recalibrated depending on the mesh size.

The grouted block interface is calibrated according to the smeared crack band properties. The normal and tangential stiffness are set to 2E+4 kip/in³ to neglect any unwanted elasticity while not ill conditioning the solution. The tensile strength is set the same as the smeared crack band elements. The cohesion, friction coefficient, and fracture energy are estimated from literature. The fracture energy is selected from estimates from Hillerborg [35]. While the friction coefficient and cohesion can be estimated from Redmond [28]. The cohesion should also satisfy the minimum requirement based on ATENA's equations. The failure envelope using ATENA's minimum cohesion should be compared to the failure envelope using the initial estimates. For the grouted block interface, the initial estimates satisfied ATENA's minimum cohesion and a reduction in tensile strength was not required.

Grouted Bed Joint Shear and Tension Behavior

The grouted bed joint interface elements normal stiffness is calibrated using the same idealized spring calculation for the smeared crack band element elastic modulus. The tangential stiffness is estimated as $\frac{K_{nn}}{2*(1+\nu)}$. The tensile strength is selected to be within the average and lower bound ratios of C1019 compression strength to modulus of

rupture strengths on similar grouted mix found by [38]. The specific ratios were selected to best fit the test data given ATENA's constraints, 9.4% from average EC samples and 9.9% from minimum ES samples. This results in the tensile strength presented in Table 4.9. This ratio is different for the EC and ES models. The cohesion, friction coefficient, and fracture energy are estimated from the best fit lines presented in Figure 4.12. Note that restrictions presented in ATENA's failure envelope equations make it impossible to match the best fit lines perfectly. Failure envelopes are selected with similar average error to the experimental results. The selected failure envelopes for the EC and ES models are shown in Figure 4.9.

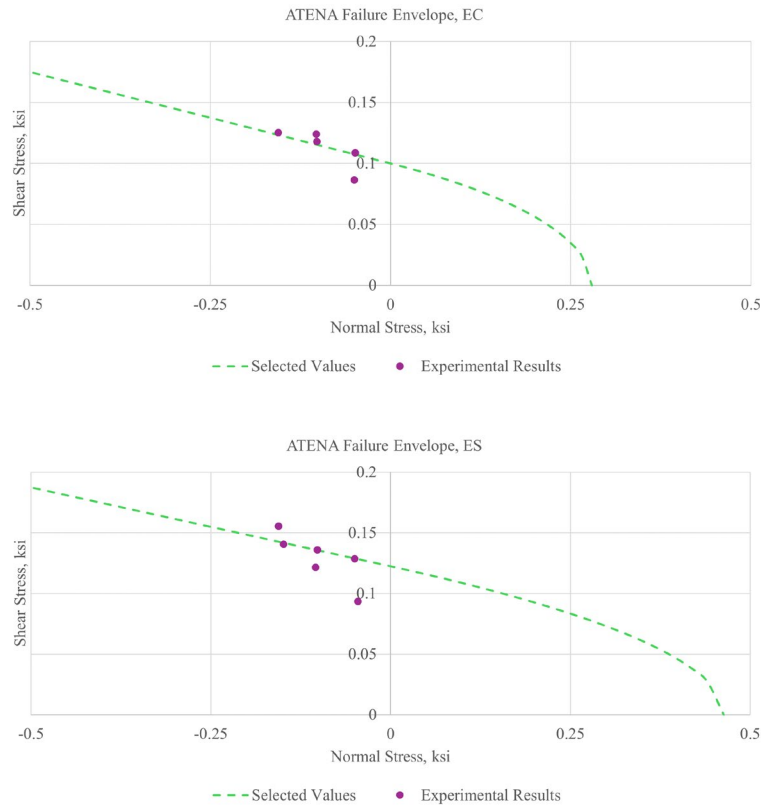


Figure 4.9: ATENA grouted bed joint failure envelopes.

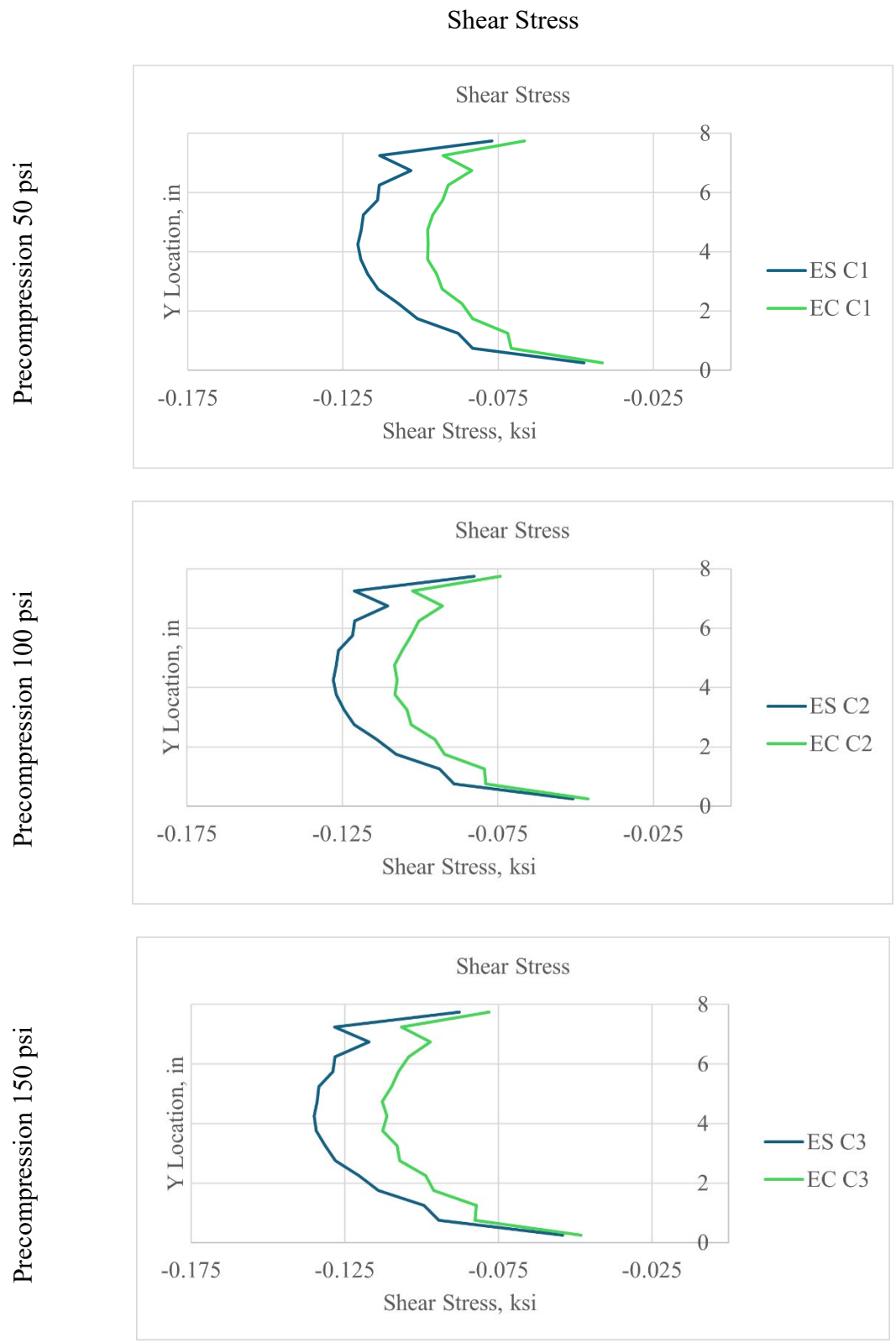
The material properties used in each model is given in Table 4.9.

Table 4.9: Element properties used in analysis

	EC	ES
Grout Strength, ksi	2.97	4.70
Fracture Energy, kip/in	1.76E-03	
Smeared Crack Band Elements		
Modulus of Elasticity, ksi	2.40E+03	3.78E+03
Poisson’s Ratio	0.25	
Tensile Strength, ksi	4.46E-01	7.05E-01
Compressive Strength, ksi	2.51	3.97
Strain at Peak Strength	2.00E-03	
Critical Compressive Displacement, in	1.35E-03	
Grouted Bed Joint Interface		
Normal Stiffness, kci	5.29E+03	8.98E+03
Tangential Stiffness, kci	2.12E+03	3.59E+03
Tensile Strength, ksi	2.79E-01	4.63E-01
Cohesion, ksi	1.00E-01	1.23E-01
Friction Coefficient	1.50E-01	1.30E-01
Grouted Block Interface		
Normal Stiffness, kci	2.00E+04	
Tangential Stiffness, kci	8.00E+03	
Cohesion, ksi	0.87	1.69
Friction Coefficient	0.98	1.20

Finite Element and Model Results

Figure 4.10 shows the shear and normal stress distribution across the grouted bed joint for the EC and ES models. The models all failed at the center of the grouted bed joint due to the shear strength capacity being reached. Note that the maximum tensile stress due to the bending induced by the test set up was much less than the average expected tensile strength of the joints and less than the minimum expected tensile capacity based on ratios of $\frac{f_r}{f_g}$ from bond wrench tests with similar grout mix designs by Banks et. al. [38]. Both tensile capacities are marked on the Normal Stress plots of Figure 4.10 for reference. Thus, the joint failure was indeed shear dominated. It is important to note that similar models were constructed of the tested specimens within the EN 1052-3 set up and there is still some tensile stress induced in the masonry. This is consistent with other works in the literature which point out the EN 1052-3 does induce some bending in the masonry [57, 58].



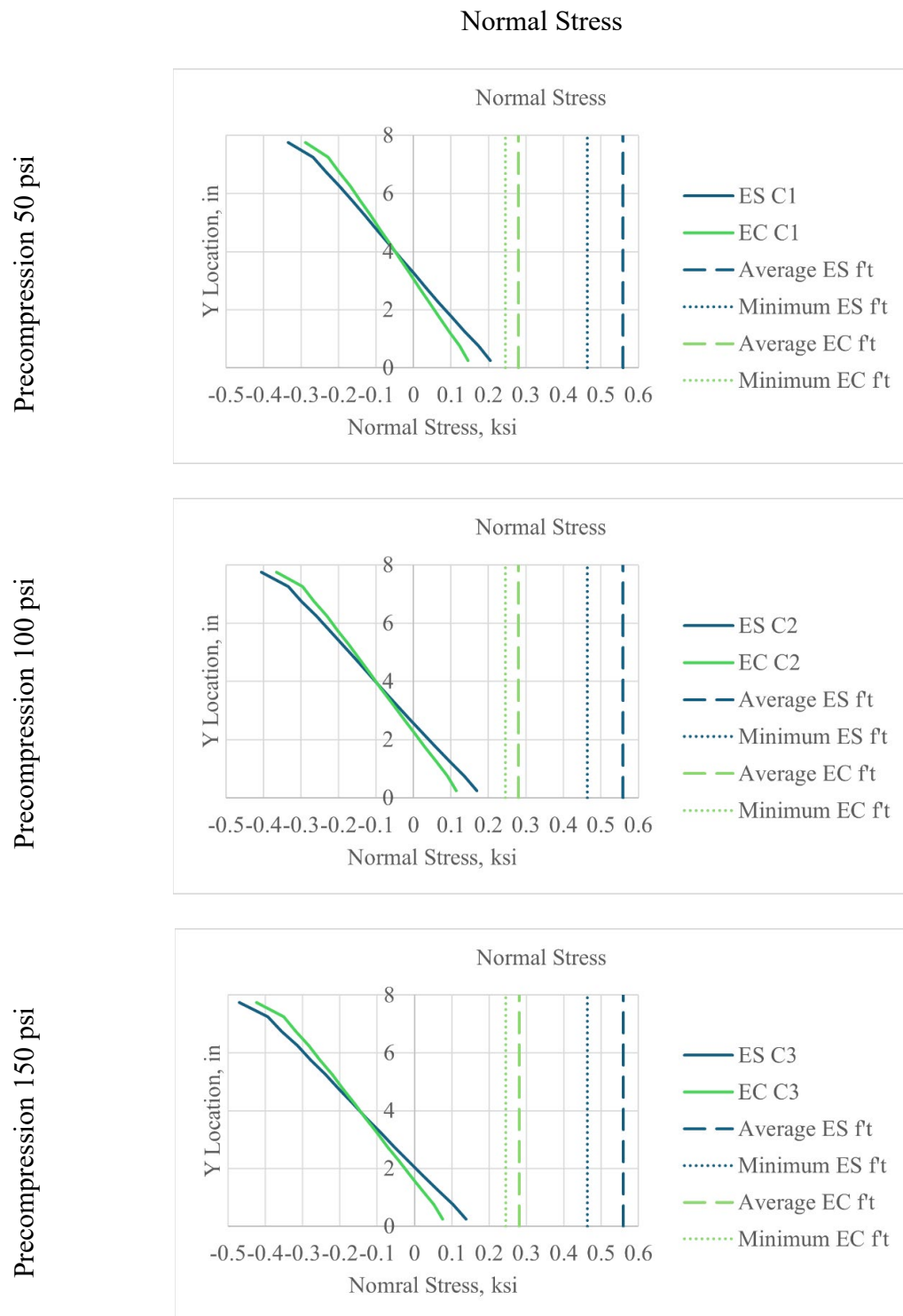


Figure 4.10: Model normal stress and shear stress distributions at difference precompression loads

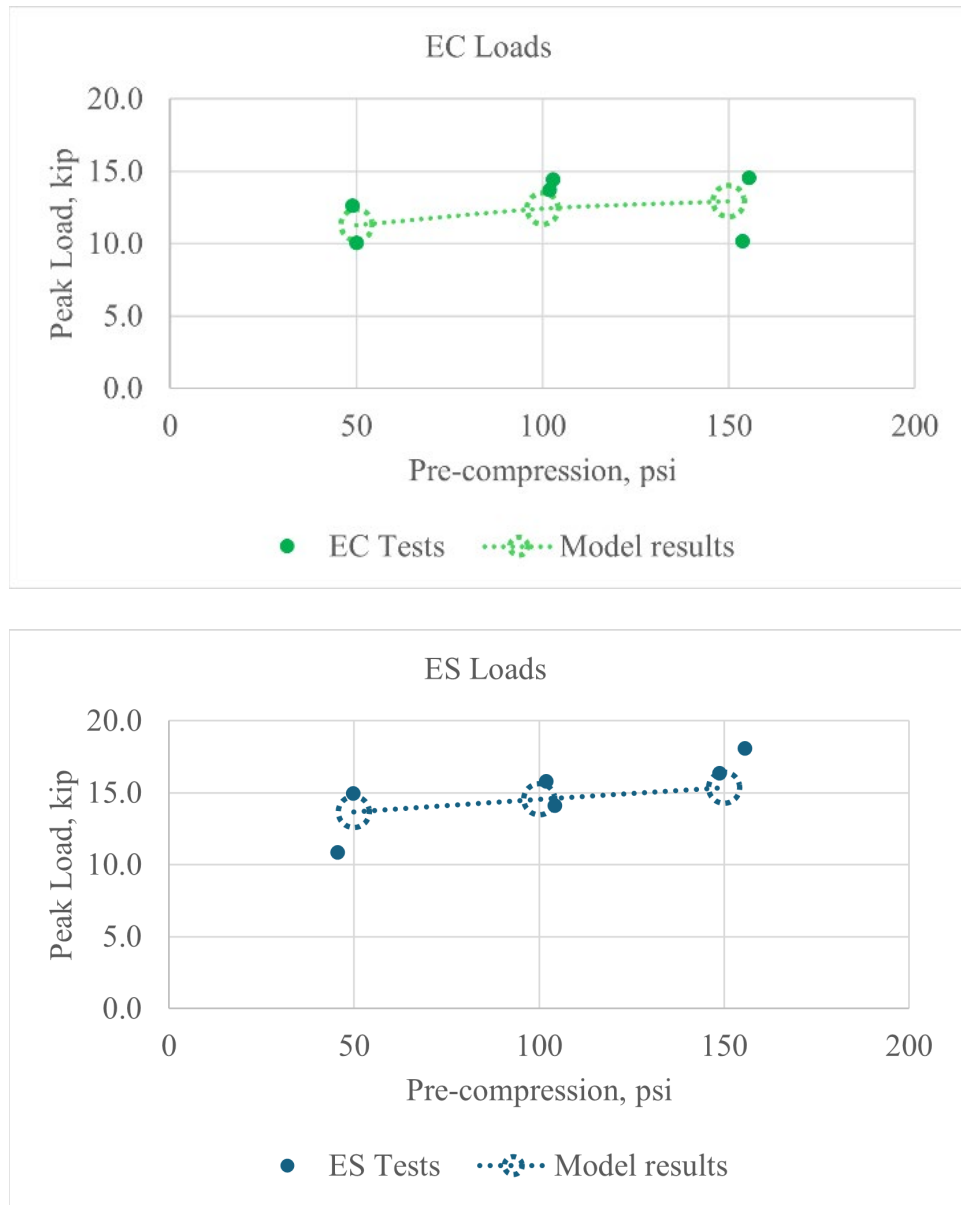


Figure 4.11: Model versus experimental peak loads.

Recommendations for Design

The following proposed reduction factors for the shear strength of grouted masonry bed joints assume that the density of the grout will control the reduction that is necessary, not the compressive strength of the grout based on the findings from Shrestha 2022b and consistent with ACI 318-19. Because of this assumption, the EC and ES datasets were compared to the whole NW dataset, except for EC_6_150 which was deemed to be an outlier. The relative densities of the EC aggregates were lower than those of the ES aggregates in both the oven-dry and saturated surface dry conditions, see Table 8.

The proposed reduction factor (λ) was calculated by equation set 4-3 to assure that the same minimum factor of safety for the LW grouts as the minimum factor of safety for the NW. Where the predicted values for both best fit equations were generated by equation set 4-1 from TMS 402/602-22. The reduction factors based on ensuring the same minimum factor of safety are very close to the range of those included in ACI 318-19 for lightweight concrete, 0.72-0.8 and are shown in Table 4.10 and Figure 4.12.

$$\text{minimum} \left(\frac{\text{Tested}_{\text{NWT}}}{\text{Predicted}_{\text{NWT}}} \right) = \frac{1}{\lambda} * \text{minimum} \left(\frac{\text{Tested}_{\text{LWT}}}{\text{Predicted}_{\text{LWT}}} \right) \quad \text{Equation Set 4-3}$$

Table 4.10: Proposed reduction factors for shear strength of grouted masonry bed joints.

	Minimum NW Tested/Predicted Shear Stress	Minimum LW Tested/Predicted Shear Stress	Suggested Reduction Factor, λ	Minimum Tested/(λ*Predicted) Shear Stress
EC	1.06	0.77	0.72	1.06
ES	1.06	0.85	0.80	1.06

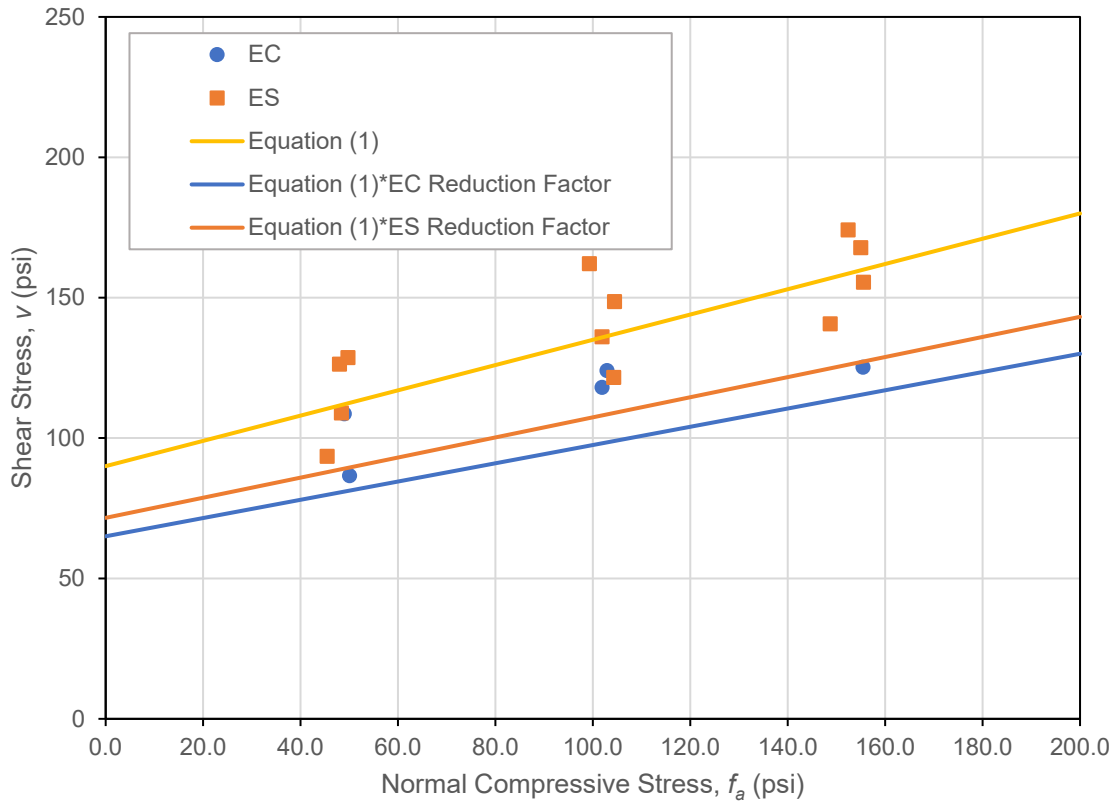


Figure 4.12: Equation set 4-1 reduced by minimum reduction factors equation set 4-3 in comparison with the unreduced version and the EC and ES datasets.

Conclusion

The lightweight grout specimens tested in this study consistently demonstrated reduced performance when compared to their normal weight counterparts and Equation (1) from TMS 402/602-22. This implies that a reduction factor for the shear strength of lightweight grouted masonry bed joints is necessary. These reduction factors have been proposed based on ensuring the same minimum ratio of tested to predicted capacity as

tests in the literature for LW grout. These reduction factors come out to 0.72 for EC and 0.80 for ES and are close to the range of values suggested in ACI 318-19, 0.75-1.00.

There was a significant difference between the reduction factors required for the two different aggregate types, with the lower density aggregate (EC) requiring a lower reduction factor. This suggests that a reduction factor based on density of the grout akin to ACI 318-19, may be more appropriate than a single reduction factor for grouts composed of all-lightweight aggregates. Additional test data at zero normal compression force are needed to verify the cohesive behavior of the lightweight grouts, and tests of different types of lightweight grouts with similar strengths are required to definitively confirm the difference in reduction factor persists based on the grout type and density.

Acknowledgements

This work was incorporated into the lab curriculum of the undergraduate and graduate masonry course, CE 4040/6040 at Clemson University; the students were eager to learn and lend their hands. The masonry blocks, expanded clay aggregates, and expanded shale aggregates were generously donated by General Shale, Arcosa Aggregates, and STALITE, respectively. James Cain of the Southeast Masonry Association, Todd Cox of OldCastle, and Doug Peay of DP Masonry contributed to lectures and connected the class to a local mason who demonstrated proper mortaring techniques to the students.

CHAPTER FIVE

BOND WRENCH TESTS

Statement of Contribution

The following work presented is the collaborative effort of Cooper Banks, Dr. Laura Redmond, Ben Hiner, Stephen Wright, and Dr. Micheal Stoner. The contribution of Cooper Banks includes the experimental testing of the expanded slate (ES) specimens, the proposed reduction factors, and the equilibrium density measurements of the expanded clay (EC) and ES specimens. The experimental testing of the EC specimen was conducted by Ben Hiner and the design of the testing apparatus was conducted by Stephen Wright.

Introduction

Lightweight (LW) concrete exhibits numerous benefits for the construction industry including higher thermal resistance [1, 2, 3], reduced seismic mass, and internal curing [4]. While LW concrete is approved and used in many circumstances, the TMS 402/602-22 code specification does not currently permit LW grout to be used in masonry design [59]. This is due to the lack of test data for LW grouted masonry assemblies. To date, there has been limited research on lightweight grout's wet and cured properties [5, 6], bond to reinforcement [7], shear strength [7], and testing on anchors within masonry assemblies constructed with LW grout [8, 9, 10].

This study is focused on measuring the flexural bond strength of fully grouted masonry assemblies with LW grout using a moment couple test device, modified from

that described by ASTM C1072 [37]. This work examines the test results for masonry prisms constructed with LW grout using expanded clay (EC) and expanded slate (ES) aggregates. The flexural bond strength test results were compared with the strength ratios of masonry assemblies with normal-weight (NW) grout from the literature to help determine whether reduction factors would be necessary to account for strength differences between LW and NW grout. The ratios used to compare LW and NW tests include that of flexural bond strength (or Modulus of Rupture), f_r , to the grout compression strength, f_g , and the $\frac{f_r}{\sqrt{f_g}}$ calculation to compare to the standard value from ACI 318-19 [15] for NW concrete, along with the average ratio of the tested to predicted flexural bond strength, f_r/f_{rp} , with predicted bond strength per TMS 402/602-22. Finally, equilibrium density measurements of each grout were used to determine a relationship between the density of the grout and the flexural bond strength of the assembly. The observed trends are compared to the lambda factor in ACI 318-19, which relates the reduction factor (lambda) to the equilibrium density of concrete.

Flexural Bond Strength of Normal-Weight Grout

Previous research has been conducted to determine the flexural bond strength masonry assemblies with NW grout, including Brown, R. et al. [60]; Hamid, A. et al. [61]; and Hamid, A. et al. [62]. The materials used, test setup description, and results are outlined below for each study. These studies are compared against the results of the tests with masonry assemblies containing LW grout in this work.

Brown, R. et al. [60] tested 40 specimens. Four different mortars with hollow clay blocks and fully grouted concrete masonry were used. The hollow clay block specimens

and concrete masonry specimens were eight and four blocks tall, respectively. The unit size used was 8 in nominal blocks conforming to ASTM C90 [64]. The grout compressive strength ranged from 5,551 to 6,939 psi (38.3 to 47.8 MPa). The specimens were tested using a modified ASTM C1390, now ASTM E518 [22], third point loading test (Figure 5.1). The concrete masonry flexural bond strengths ranged from 122 psi (0.84 MPa) to 162 psi (1.12 MPa).

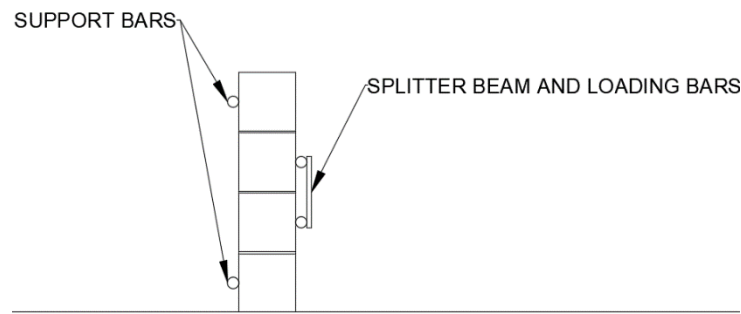


Figure 5.1: Modified C 1390 Testing Apparatus [60]

Hamid, A. et al. [61] tested 172 specimens. Each specimen was 31 in by 62 in (790 mm by 1,600 mm) concrete block masonry walls. The block sizes used were 7.48 in by 7.48 in by 15.35 in (19 cm by 19 cm by 39 cm) blocks, 5.51 in by 7.48 in by 15.35 in (14 cm by 19 cm by 39 cm) blocks, and 9.45 in by 7.48 in by 15.35 in (24 cm by 19 cm by 39 cm) blocks. The grout compressive strength ranged from 1,987 to 5,947 psi (13.7 to 41.0 MPa). Each specimen was tested using third point bending, either testing the tensile strength normal or parallel to the bed joint (Figure 5.2). The flexural bond strength of fully grouted specimens ranged from 197.3 psi (1.36 MPa) to 242.2 psi (1.67 MPa).

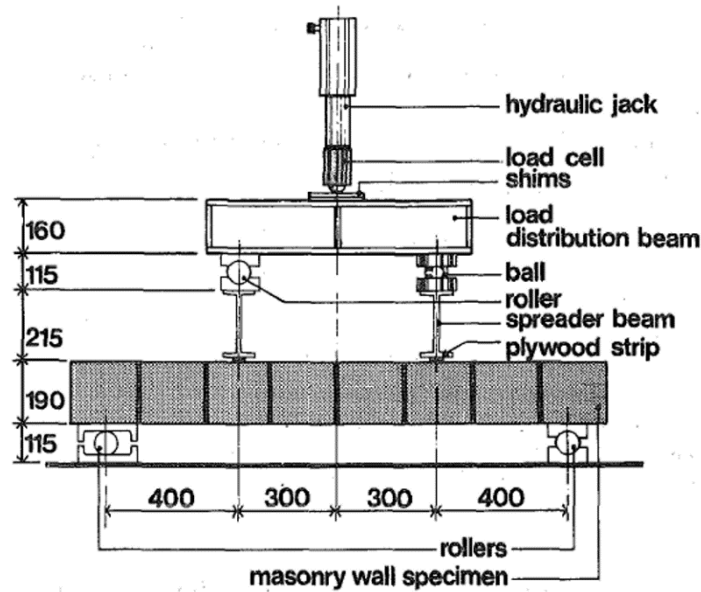


Figure 5.2: Hamid, A. et al. Test Set-Up [61]

Hamid, A. et al. [62] tested 15 small-scale masonry unit walls. Every specimen was three courses tall but varied in width depending on the spacing of the grout. The unit size used was 8 in nominal blocks conforming to ASTM C90 [64]. The grout compressive strength ranged from 1,681 to 1,847 psi (11.6 to 12.73 MPa). Three specimens were created for the grout conditions of ungrouted, fully grouted, and cells grouted at 16 in (41 cm), 24 in (61 cm), and 32 in (81 cm) on center. Each specimen was failed along both bed joints resulting in 30 total tests. The specimens were tested using a modified bond wrench test similar to the ASTM C1072 [37] test. A sketch of this modified bond wrench was not recreated for the literature review because the authors could not precisely discern what modifications were made. The flexural bond strength of fully grouted specimens ranged from 293 psi (2.02 MPa) to 345 psi (2.38 MPa).

Flexural Bond Strength Testing per ASTM C1072

The standard flexural bond strength test is detailed in ASTM C1072 [37]. This test is applicable for stacked clay or concrete masonry units bonded with mortar, which have an applied force normal to the bed joint from the bond wrench device. The breaking strength of these masonry units at the mortar joint gives an indication of the flexural tensile strength of the mortar used to connect the concrete masonry units. The standard design of the bond wrench device applicable to this test is shown (Figure 5.3). While this test is useful for finding the flexural tensile strength of masonry walls connected with mortar under loads normal to their bed joints, it is not applicable for fully grouted masonry units as tested in this study. This is due to the dimensions of this standard bond wrench device as it only allows for masonry units 3.625 in (9.21 cm) wide by 2.25 in (5.72 cm) high with a length between 7 in (18 cm) and 7.625 in (19.37 cm). The fully grouted masonry units used for this LW grout study have dimensions 7.625 in (19.37 cm) wide by 7.625 in (19.37 cm) high with a length of 15.625 in (39.69 cm) and would not fit within this standard bond wrench testing apparatus. This apparatus also only applies its load in a single direction to break the masonry at the mortar joint. This is appropriate for the lower overall strength of mortar but would not be sufficient for the higher strength of the fully grouted concrete masonry units used in this study.

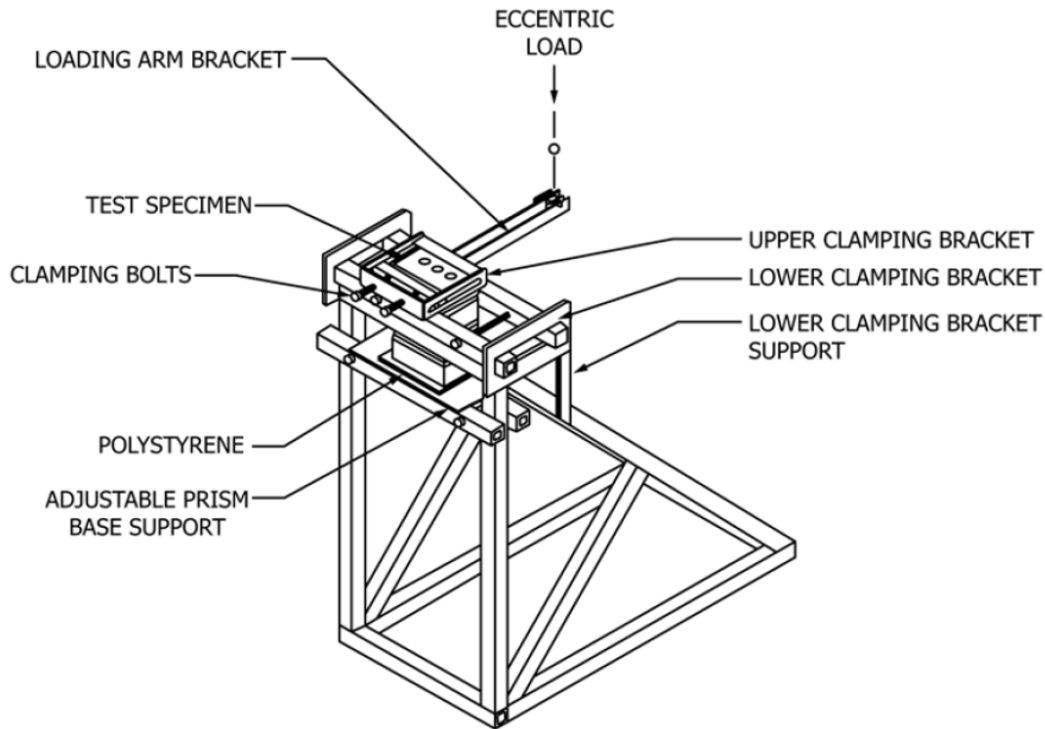
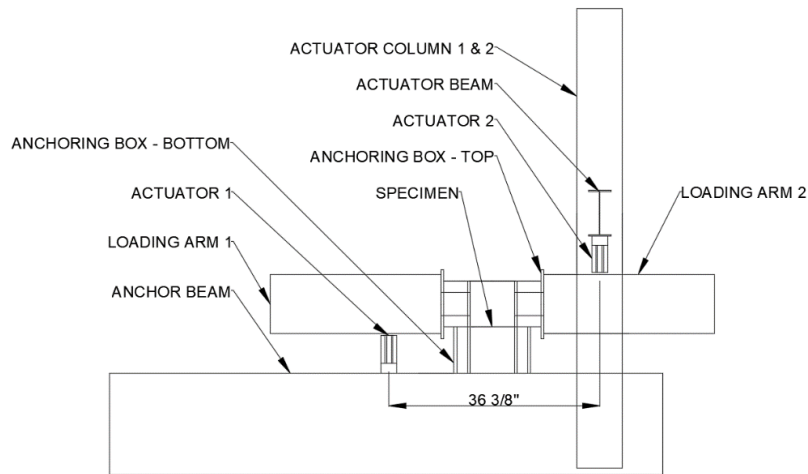


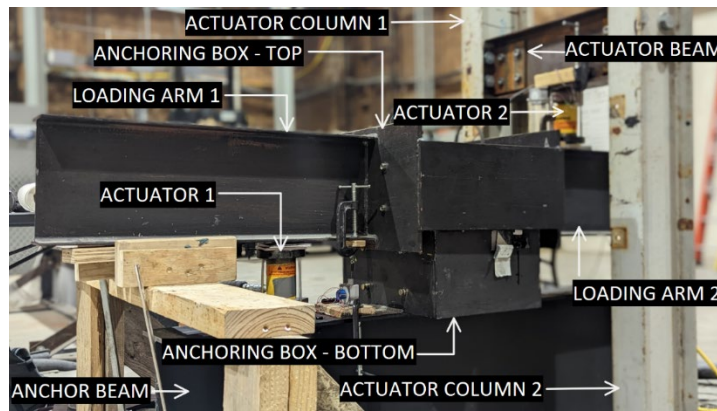
Figure 5.3: ASTM C1072 Bond Wrench Testing Apparatus [37]

Design of the Moment Couple Device

The moment couple test device was designed to induce a flexural failure mode across the mortar joint of fully grouted masonry prisms (akin to ASTM C1072 specimens). This was accomplished by applying a moment across the bed joint of the specimen using two actuators that were pressurized from one hydraulic pump using a T-splitter (Figure 5.4(a) and Figure 5.4(b)). This actuator orientation creates no net axial force across the masonry cross section. The only axial force applied to the masonry is from the self-weight of the testing apparatus and top course of masonry. The failure mode of the masonry produced is representative of out-of-plane flexure (tension normal to the bed joint).



(a) Schematic of the test set up



(b) Physical test set up

Figure 5.4: Schematic of the test set up (a) and the physical test set up (b) [38]

Load Path Description

The target stress distribution along the failure plane of the masonry specimen (Figure 5.5) is a combination of the self-weight of the masonry and testing device, resulting in axial compression only, (calculated previously) and the applied moments from actuator 1 and 2. Figure 5.5 also visualizes the loading and orientation of the

masonry faces. The load path flows from each of the actuators 1 & 2 shown in (Figure 5.5 and Figure 5.6), then is transferred through the loading arms (Figure 5.6) to the top anchoring box with welded connections. The loads are transferred from the top anchoring box to masonry face plates (Figure 5.6) unit using a series of bolted clip angles referred to as the top connection (Figure 5.6). The loads from the face plates are transferred to the top unit of the masonry prism with bolted connections that use epoxied threaded rods embedded in the masonry. The bottom course of the masonry prism is restrained using a bolted face plate to anchoring box connection. This connection is referred to as the bottom connection (Figure 5.6). The bottom anchoring box was welded to the anchor beam and the anchor beam was connected to the strong floor. Although not all capacity checks are presented here for brevity, the critical limitation of the device was found to be the epoxied anchors. To avoid failure of the epoxied anchors, the device was limited to testing assemblies with grout compression strength less than 3,500 psi (24 MPa).

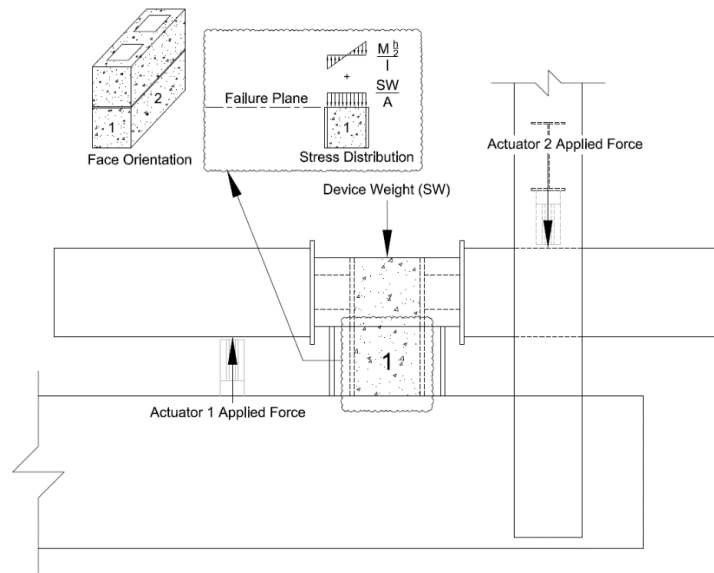


Figure 5.5: Loading and Specimen Orientation [38]

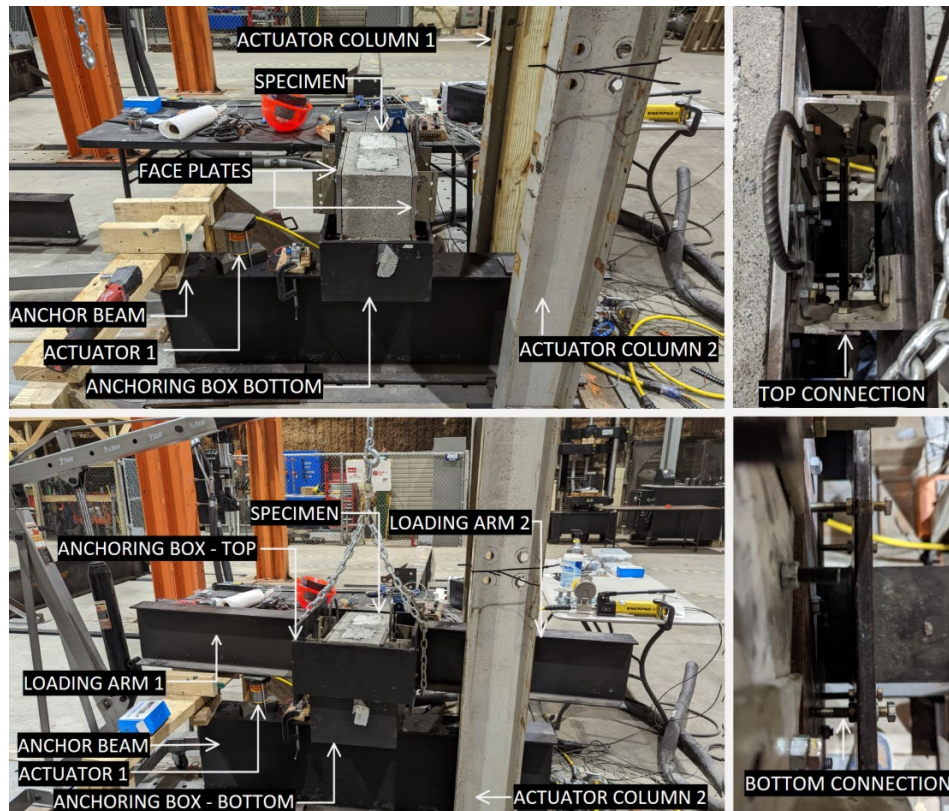


Figure 5.6: Demonstration of Specimen Placement and Connection from Masonry to the Loading Arm [38]

Assembly Process

To assemble the device for testing, the steel face plates were first attached to the face of the masonry prism with drilled and epoxied in place threaded rods. Once that was complete, the specimen was lifted onto the anchor beam (Figure 5.6) and attached to the bottom anchoring box with the bottom connection. Next, the loading arm assembly was lowered over the specimen and attached to the top plates of the masonry using the top connection (Figure 5.6). After, the actuator beam and actuator 2 were placed. Finally, string pots were connected to loading arm 1 and 2 at equal distances from the neutral axis of the masonry prism so that one could monitor that the displacements were approximately equal throughout the test. Note that during the assembly processes, best efforts were made to center the specimen within the device, but the specimen location could vary slightly test to test. Tolerances were required to be able to load the specimen into the device ~1.0 in. (2.54 cm) gap between the masonry specimen and the inside of the anchoring box. Worst case, these tolerances could result in up to a +/- 5.5% change of length on the moment arm for each actuator, but best efforts were given to place the masonry at the center of the test device.

Calculation of Masonry Stress State at Failure and Comparison to the ASTM C1072 Bond Wrench Device

The state of stress in the masonry prism is a combination of compression (due to the weight of the loading device, plates, and top masonry unit) and flexure (due to the moment induced from the actuators). The goal of the moment couple device design was

to ensure that the compression stress induced by the machine was similar to the low level of compression stress induced by the ASTM C1072 [37] bond wrench device. To calculate the compression stress on the masonry for the moment couple test, the unit weight from the equilibrium density test of the masonry grouted assembly of 97.2 lbf/ft³ (1560 kg/m³) was used. The measured weights for the components of the moment couple device are shown below in Table 5.1. The dimensions of the upper portion of the masonry specimen were detailed, and the self-weight of the top masonry course was calculated to be 50.2 lbf (220 N). The weight of the upper portion of the test device includes loading arm 1, loading arm 2, the top anchoring box, and the face plates (see Figure 5.6). These elements contribute to the compression force experienced during testing. The weights of these parts of the device total 243.9 lbf (1085 N). Based on the total weight of the specimen and loading device, the compression stress on the specimen is 2.33 psi (0.016 MPa). A similar calculation was conducted for the standard ASTM C1072 [37] bond wrench device for a standard modular clay brick specimen, and the compression stress is 1.6 psi (0.01 MPa). Note that the loading for the ASTM C1072 device is a one-sided lever arm, so the applied axial load has significance. However, for the moment couple device used in this testing, the axial loads from each loading arm offset each other. In future testing, the precompression load could be further reduced by shortening loading arm 1 and 2, but for initial testing the beam was kept longer to permit flexibility to use the device for other research applications. Note that the actual ratio of the compression stress from self-weight to the tensile stress at failure was much lower for this device than the ASTM C1072 [37] device (see Test Results and Discussion).

Table 5.1: Masonry Self Weight (SW), Dimensions, and Other Dead Weight from Test Device

Top Course	b	h	A	I	Loading arm 1 and 2	Face Plates	Anchoring box - top
SW	in (cm)	in (cm)	in² (cm²)	in³ (cm³)	lbf (N)	lbf (N)	lbf (N)
50.2 (223)	15.625 (39.69)	7.625 (19.37)	119.14 (768.64)	577.24 (9459.3)	95 (420)	48 (210)	100.91 (448.87)

The flexural bond strength was calculated for each test by equation set 5-1:

$$f_r = \frac{-SW}{A} + \frac{M \frac{h}{2}}{I} \quad \text{ASTM C1072 [37] Equation Set 5-1}$$

where SW is the self-weight of the masonry and device (294.51 lbf, 1310.1 N), A is the cross-sectional area of the grouted CMU (119.14 in², 768.64 cm²), M is the moment applied by the two actuators shown in Figure 5.5, h/2 is the distance to the maximum tensile stress location from the neutral axis (3.8125 in, 9.684 cm), and I is the moment of inertia across the axis of bending (577.24 in³, 9459.3 cm³),.

Material Properties

The aggregate and grout mix properties are specified in the following sections. Since the flexural tension capacity of the grouted prisms is governed by the grout behavior, ASTM tests of the mortar and the unit compression strength were not conducted. The block was a standard 8 in x 8 in x 16 in (20 cm x 20 cm x 40 cm) unit complying with ASTM C90 [64]. The mortar was a type S mortar cement.

Aggregate Properties

Aggregate properties have previously been characterized by Shrestha, R. et al. (2022a) [10] and are repeated here. Note that the aggregate gradation complied with ASTM C330 and ASTM C404 [65, 66].

Table 5.2: Aggregate Properties

Physical Property	Expanded clay coarse	Expanded clay fines	Expanded slate coarse	Expanded slate fines
Relative density (OD)	0.92	0.88	1.44	1.75
Relative density (SSD)	1.17	1.35	1.55	2
Specific Gravity (SG)	1.17	1.35	1.55	2
Absorption (%)	27.49	52.68	7.87	14.5
Gradation				
Sieve Size	Cumulative % weight by passing			
½ in	100	100	100	100
3/8 in	100	100	97.4	100
#4	30.6	100	9.3	100
#8	2.1	69.8	6.9	93.4
#16	1.3	43.6	5.8	41.9
#50	0.8	13.9	5.3	23.8
#100	0.5	9.8	4.9	10.4
#200	0.2	-	2.8	-

Grout Mix Design and Compressive Strength

To prepare the masonry prisms and C1019 [37] specimens, the aggregate for the grout mix was weighed in approximately saturated surface dry (SSD) condition. Approximate SSD conditions were achieved by soaking the aggregates for 72 hours and then drying them for 24 hours ASTM C127/C128 [67, 68] by laying them on elevated plastic sheeting with drain holes covered by a tarp. This ensured the aggregates did not draw excess water away from the grout mix or contribute too much free water to the mix. After this process, the necessary amounts of cement and water were weighed out, and the mixing process could begin. First, the coarse and fine aggregates were added and combined in the mixer, and then cement and water were added in small batches to prevent clumping of the cement. The slump of the mix was tested periodically, and water was added after each test until the desired consistency was achieved (8-10 in (20.32-25.4 cm) slump per ASTM C476 [20]. The final volume proportions and compression strength of the three batches of grout used in this study are shown in Table 5.3 and Table 5.4. Note that the volume proportions provided in Table 5.3 were found using the SSD densities of the aggregates and the bulk density of cement (94 lbf/ft³). Note that the final compression strength corresponds to a compression test of the ASTM C1019 [37] specimens within seven days of the flexural bond strength test. Batch 1's compression strength was lower than Batch 2's due to increased water content. This was reflected in the higher slump in Batch 1.

Table 5.3: Mix Design for Grout Batches

Batch Number	Components			Slump in (cm)
	Coarse aggregate	Fine aggregate	Cement	
Batch 1 (EC)	0.79	1.77	1	8.5 (22)
Batch 2 (EC)	0.79	1.77	1	8.25 (21)
Batch 3 (ES)	0.94	1.94	1	8.25 (21)

Table 5.4: Compression Test Results

Compression Tests										
Batch Number		psi (MPa)								
		7-Day			28-Day			Final		
Batch 1 (EC)	Individual	1404	1350	1225	1587	1732	1698	1989	2040	2018
		(9.7)	(9.3)	(8.5)	(10.9)	(11.9)	(11.7)	(13.7)	(14.1)	(13.9)
	Average	1326 (9.1)			1672 (11.5)			2015 (13.9)		
Batch 2 (EC)	Individual	1860	1802	1881	2067	2147	2056	2565	2638	2604
		(12.8)	(12.4)	(13)	(14.3)	(14.8)	(14.2)	(17.7)	(18.2)	(18)
	Average	1847 (12.7)			2090 (14.4)			2602 (17.9)		
Batch 3 (ES)	Individual	-	-	-	2035	1858	1954	2035	1858	1954
					(14)	(12.8)	(13.5)	(14)	(12.8)	(13.5)
	Average	-			1949 (13.4)			1949 (13.4)		

Preparation of the Masonry Prisms

The ungrouted masonry prisms consisted of two hollow CMU blocks stacked with one mortar joint. After the ungrouted specimens were prepared, they were filled with the grout described in the material properties section and tamped with a rod when the mixture reached each third point of the specimen. Eight ES and Eight EC specimens were prepared. For the C1019 [37] specimens, CMU blocks were used to create a 3 in (7.62 cm) square void into which grout mix could be placed and lined with soaked paper towels. When the masonry prisms and C1019 [37] specimens were filled with grout, they were covered with plastic. After 24 hours, the C1019 [37] specimens were removed from their molds and relocated to a fog room until compression testing. The masonry prisms remained covered in plastic for 28 days within the climate-controlled environment of the laboratory. For compression testing, the C1019 specimens were saw cut to meet the dimensional requirements of ASTM C1019 [37].

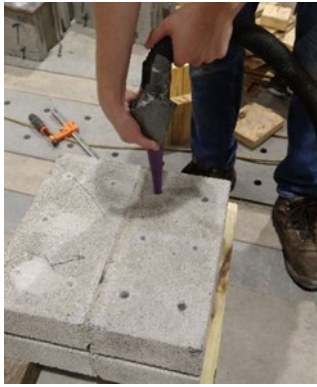
To prepare the masonry prisms for testing in the moment couple device, twelve holes were drilled on each side, with six holes equally spaced on each CMU block face. Pilot holes were first drilled through the metal plates to ensure that they were in the correct locations (Figure 5.7a and Figure 5.7b). Afterwards, these metal plates were removed, and the final 2.5 in (6.4 cm) deep holes were drilled using a 0.50 in (1.3 cm) masonry drill bit. The depth of each hole was checked with a marked threaded rod (Figure 5.7c). Note that several test specimens were saw cut along the mortar joint to check that the drilling process did not disturb the bed joint interface (no cracking was present).



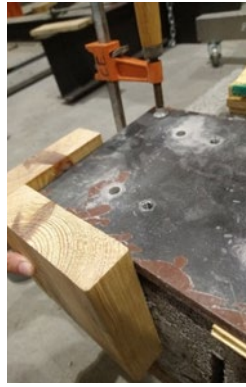
(a) Plates Placed for Pilot Holes (b) Drilled Pilot Hole (c) Anchor Depth Check

Figure 5.7: Holes Drilled in Masonry [38]

After these holes were drilled, a vacuum was used to remove any excess dust that resulted from the drilling process (Figure 5.8a), and then the holes were filled with SET-XP epoxy. Threaded rods 4 in (10 cm) long and 0.375 in (0.95 cm) in diameter were placed in each hole, displacing the epoxy. Any excess epoxy that was pushed out of the holes was cleaned away using paper towels. Afterwards, wooden spacers were placed on the face of the masonry to separate the face plates from excess epoxy. Then, the final metal plates were placed over these with the threaded rod feeding through the holes in the metal plates. The plates were then aligned with the corners of the CMU blocks and clamped down to ensure they did not slide (Figure 5.8b). The epoxy was allowed to set for 4-8 hours before the prism specimens were rotated, and the process was repeated. A specimen with the plates attached is shown (Figure 5.8c).



(a) Excess Dust Removal



(b) Plate Squaring



(c) Specimen with Plates

Figure 5.8: Masonry Specimen Preparation [38]

Test Procedure

The overall test set up is shown in Figure 5.4. Both string pots connected to loading arm 1 and 2 were secured and used to ensure there was not excessive slip in the connections of the masonry to the loading device. Actuator 2 attached to the actuator beam and actuator 1 attached to the anchor beam. The actuators were centered and tightened down to secure them in place. The setup of actuator 2 and string pot is shown in Figure 5.9. Hydraulic hoses were attached to upper and lower actuators and connections were tightened. The hydraulic splitter was opened, and the hydraulic pump was operated until the actuators had contacted the upper and lower sides of loading arm 1 and 2, respectively. At this point, the test could begin, and the hydraulic pump was operated at a consistent pace so that the specimen broke at the mortar joint between one and three minutes from the start of the test (per ASTM E518 [22]). Measurements taken during the testing included continuous measurement of the pressure in the individual hydraulic

actuators using two digital pressure gauges and displacements of loading arm 1 and 2. The first specimens tested were used to practice the assembly process with the test device, and ultimately six ES and five EC specimens were tested, and their results are compiled in the test results and discussion section.



Figure 5.9: String pot and Actuator Set Up [38]

Test Results and Discussion

Flexural Tensile Strength Results

Examples of a typical failure for an EC and ES specimen are shown in Figure 5.10a and Figure 5.10b. The specimens all exhibited a clean tensile splitting failure across the mortar/grout joint initiating from the end of the specimen in tension during the testing.



(a) Expanded Clay Specimen



(b) Expanded Slate Specimen

Figure 5.10: Typical Failures [38]

The data gathered from the flexural tensile strength tests performed on fully grouted masonry specimens using EC and ES LW grout is laid out in this section. In Table 5.5, the bond strength of these masonry specimens is based on the resulting maximum force outputs from the actuators during testing. These flexural tensile strength values were compared to values for grout compression strength obtained from compression tests performed on C1019 [37] grout samples within seven days of the flexural tensile strength tests. The ratio of flexural bond strength (or Modulus of Rupture), f_r , to the grout compression strength, f_g , was also tabulated and converted to a percentage value. The average $\frac{f_r}{f_g}$ ratio came out to 10.8%. This value is compared to NW samples from the literature. The $\frac{f_r}{\sqrt{f_g}}$ calculation of Table 5.5 was included to compare to the standard value from ACI 318-19 [15] for NW concrete, which specifies that:

$$f_r = 7.5\sqrt{f'_c}, \text{ in psi for } f'_c \text{ in psi} \quad \text{ACI 318 [15] Equation Set 5-2}$$

Where f'_c is the characteristic concrete strength. This value was found to be 4.91 for the LW grout samples. This calculation was also performed for the NW grout data from previous studies to account for the fact that the 7.5 factor from ACI 318-19 [15] would be most applicable for samples made up of solely grout, while these flexural tensile stress tests include the full assembly and account for the strength of the mortar joint. Therefore, these calculations were performed for both NW and LW samples in Table 5.7 so a more direct comparison of the level of conservatism of the TMS 402/602 [59] code could be made.

Table 5.5: Results of Flexural Bond Strength Tests

Test Date (Grout Batch)	Breaking	Applied	Flexural	Grout	Ratio	$f_r/\sqrt{f_g}$ U.S.
	Strength	Moment	Bond	Compression		
			Strength	Strength		
	Applied P	M	f_r	f_g	f_r/f_g	
	lbf (N)	lbf*in (N*m)	psi (MPa)	psi (MPa)	(%)	
6/2/2022 Batch 1 (EC)	699.2 (3110)	25435 (2874)	165.5 (1.14)	1672 (11.53)	9.90	4.05
7/15/2022 Batch 1 (EC)	701.6 (3120.9)	25520 (2996)	166.2 (1.15)	2015 (13.89) ¹	8.25	3.75
				Batch 1 COV %	12.92	6.35
8/3/2022 Batch 2 (EC)	976.3 (4343)	35513 (4012)	232.3 (1.60)	2602 (17.94) ¹	8.93	4.55
8/4/2022 Batch 2 (EC)	1092.9 (4861.5)	39755 (4492)	260.3 (1.79)	2602 (17.94) ¹	10.00	5.10
8/5/2022 Batch 2 (EC)	1101.5 (4899.7)	40068 (4527)	262.3 (1.81)	2602 (17.94) ¹	10.08	5.14
				Batch 2 COV %	6.68	6.68
10/28/2022 Batch 3 (ES)	809.3 (3600)	29440 (3326)	192.1 (1.32)	1949 (13.43)	9.86	4.35
10/30/2022 Batch 3 (ES)	1002.4 (4458.9)	36462 (41120)	238.5 (1.64)	1949 (13.43)	12.24	5.40

11/1/2022 Batch 3 (ES)	1106.3 (4921.1)	40240 (4547)	263.5 (1.82)	1949 (13.43)	13.52	5.97
11/1/2022 Batch 3 (ES)	1112.7 (4949.5)	40474 (4573)	265.0 (1.83)	1949 (13.43)	13.60	6.00
11/1/2022 Batch 3 (ES)	958.3 (4263)	34856.9 (3938)	227.9 (1.57)	1949 (13.43)	11.69	5.16
11/2/2022 Batch 3 (ES)	859.3 (3822)	31257.1 (3532)	204.1 (1.41)	1949 (13.43)	10.47	4.62
				Batch 3 COV		
				%	12.95	12.95
				Average	10.8	4.9
				Standard		
				Deviation	1.76	0.74

1. The grout compression strength was found by taking cores from failed specimens, rather than the 28-day strength of C1019 samples cast with the specimens.

The ratio of the compression stress (calculated previously) to the tested average flexural bond strength was 1.13%. The maximum ratio for any test was 1.4%. This compared to the standard ASTM C1072 [37] bond wrench machine for a modular brick with type N masonry cement mortar, the ratio of compression stress (calculated previously) to tabulated flexural bond strength from TMS 402/602 [59] was 3.13%.

Table 5.6 shows the comparison between the tests bond strength (f_r) shown in Table 5.5 and the predicted bond strength (f_{rp}) from TMS 402/602-22. Because a type S mortar cement was used for all masonry assemblies in this study, the predicted bond

strength was 163 psi (1.12 MPa) overall. The resulting ratio of tested to predicted flexural bond strength was 1.38 on average and always greater than 1.0 for all specimens tested. This is a positive indication that the current code is conservative for LW specimen, but ideally the tested to predicted ratios for NW specimens and LW specimens should be similar to provide a similar level of conservatism with respect to the code predictions. The coefficients of variation (COV) for the calculated ratios in Table 5.5 and Table 5.6 are within a reasonable range, of 10% - 20% for bond wrench tests given work done by Wood, S. [63].

Table 5.6: Tested Strength vs. Predicted Strengths

Test Date (Grout Batch)	Mortar Type	TMS 402-602	
		Predicted Flexural Bond Strength	Ratio
		f_{rP} , psi (MPa)	f_r / f_{rP}
6/2/2022 Batch 1 (EC)	Type S Mortar Cement	163 (1.12)	1.02
7/15/2022 Batch 1 (EC)		163 (1.12)	1.02
		Batch 1 COV	0.24
		%	
8/3/2022 Batch 2 (EC)		163 (1.12)	1.42
8/4/2022 Batch 2 (EC)		163 (1.12)	1.60
8/5/2022 Batch 2 (EC)		163 (1.12)	1.61
		Batch 2 COV	6.68
		%	
10/28/2022 Batch 3 (ES)		163 (1.12)	1.18

10/30/2022 Batch 3 (ES)	163 (1.12)	1.46
11/1/2022 Batch 3 (ES)	163 (1.12)	1.62
11/1/2022 Batch 3 (ES)	163 (1.12)	1.62
11/1/2022 Batch 3 (ES)	163 (1.12)	1.40
11/2/2022 Batch 3 (ES)	163 (1.12)	1.25
	Batch 3 COV	12.95
	%	
	Average	1.38
	Standard Deviation	0.23

Comparison of Test Data to Assemblies with Normal-weight Grout

The data gathered for the masonry prisms with LW grout were subsequently compared to data gathered from previous research on masonry assemblies with NW grout, compiled in Table 5.7 below. The averages and single standard deviation errors of the $\frac{f_r}{\sqrt{f_g}}$ and $\frac{f_r}{f_{rP}}$ ratios for the NW and LW batches are displayed in Figure 5.11 and Figure 5.12, respectively. Column four of this table displays the average percentage ratio between the flexural bond strength and grout compressive strength for each NW batch. At the bottom of this table, the average values over all these data points considered and the average for data within a comparable grout compressive strength range are shown. The comparable grout compressive strength range was defined as values of grout compressive strength between 1987 psi (13.70 MPa) and 3350 psi (23.1 MPa), similar to the compression strengths for the LW grout samples in this study. As can be seen, the tension

to grout compression strength ratio for the comparable values was 10.2%, displaying a similar result to the 10.8% obtained from the samples constructed with LW grout.

The $\frac{f_r}{\sqrt{f_g}}$ values were calculated in the same manner as the previously discussed ratio; an average value was determined for all results, as well as an average value for results with comparable grout compression strength values to the LW grout tested in this study. The average $\frac{f_r}{\sqrt{f_g}}$ of all the NW specimens was 2.9, somewhat lower than the 4.9 value from the assemblies constructed with LW grout. However, when taking an average from the results with comparable grout compression strengths, this average came out to be 5.5, much closer to the 4.9 result from the assemblies with LW grout.

The average ratio between the tested and predicted flexural bond strengths were also calculated for the NW batches, as is shown in column 11 of Table 5.7. The predicted strengths for these NW grouts differ based on the type of mortar used, as per TMS 402/602-22. Note that many of the presented NW samples were used to formulate the TMS 402/602 provisions and the equations are formulated for conservatism first, rather than accuracy, and thus we would not expect all the NW tested and predicted flexural bond strengths to be around 1.0. The overall average tested to predicted strength was 1.2 considering all data points, while for the average of the results with comparable grout compression strengths was 1.8. The average value from the masonry assemblies with LW grout was 1.38, meaning that the predictions for flexural bond strength in TMS 402/602 were conservative for the LW specimens tested and resulted in acceptable ratios of tested to predicted capacity. However, this ratio is slightly lower than the ratio of 1.8 for the

NW specimens with comparable grout compression strengths. The COVs of the NW studies show similar levels of variation with the LW specimens and of previous literature from Wood, S. [63].

Table 5.7: Normal-Weight Grout Test Results

Research Study	TMS									
	Average		Average				402/602			
	Flexural	Grout					Mortar	Predicted		
	Bond	Compression	Ratio				Type	Flexural	Ratio	
	Strength	Strength			$f_r/\sqrt{f_g}$		(Number	Bond		
					U.S.		of	Strength		
	f_r	f_g	f_r/f_g	COV		COV	Samples)	f_{rP}	f_r/f_{rP}	COV
	psi	psi (MPa)	(%)	(%)		(%)		psi (MPa)	(%)	(%)
	(MPa)									
[60]	133	6192	2.14	5.33	1.70	4.16	Type N	145 (1.0)	0.90	7.86
	(0.917)	(42.69)					Masonry			
							Cement			
							(5)			
	146	6192	2.38	8.08	1.86	9.77	Type S	153 (1.05)	0.96	11.9
	(1.01)	(42.69)					Masonry			
							Cement			
							(5)			
	145	6192	2.34	4.87	1.84	2.98	Type N	158 (1.09)	0.92	4.9
	(1.00)	(42.69)					PCL (5)			

	155	6192	2.50	2.83	2.00	3.54	Type S	163 (1.12)	0.92	4.9
	(1.06)	(42.69)					PCL (5)			
[61]	214	3664	6.87	42.4	3.73	17.4	Type S	163 (1.12)	1.3	13.3
	(1.48)	(25.26)					PCL (3)			
[62]	323	2980	10.9	6.67	5.92	6.36	Type S	163 (1.12)	1.97	6.95
	(2.23)	(20.55)					PCL (6)			
Total			4.6		2.9		Total			1.2
Average							Average			
Average for							Average for			
Comparable			10.2		5.5		Comparable			1.8
f_g							f_g			

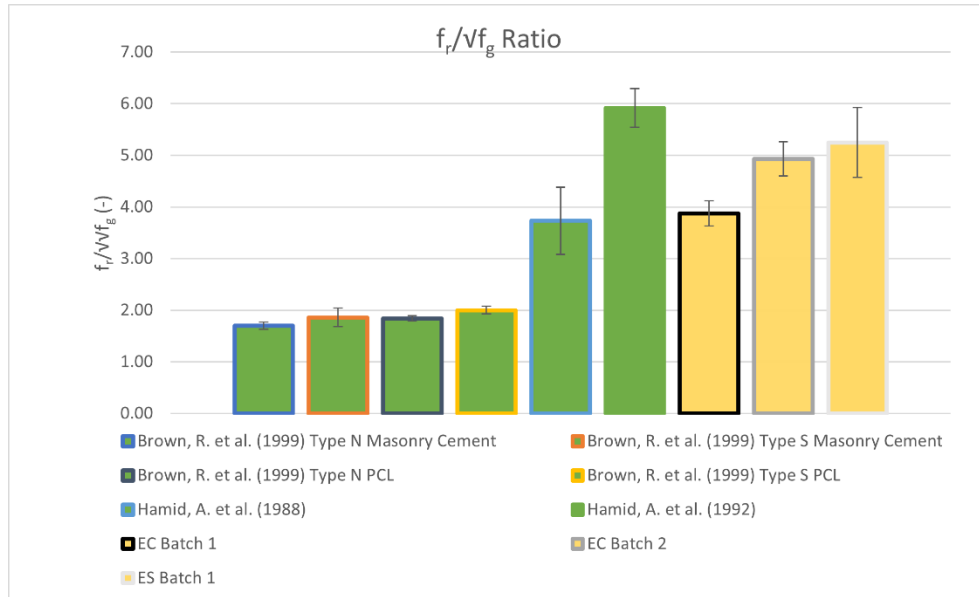


Figure 5.11: $\frac{f_r}{\sqrt{f_g}}$ NW and LW batch comparison [38]

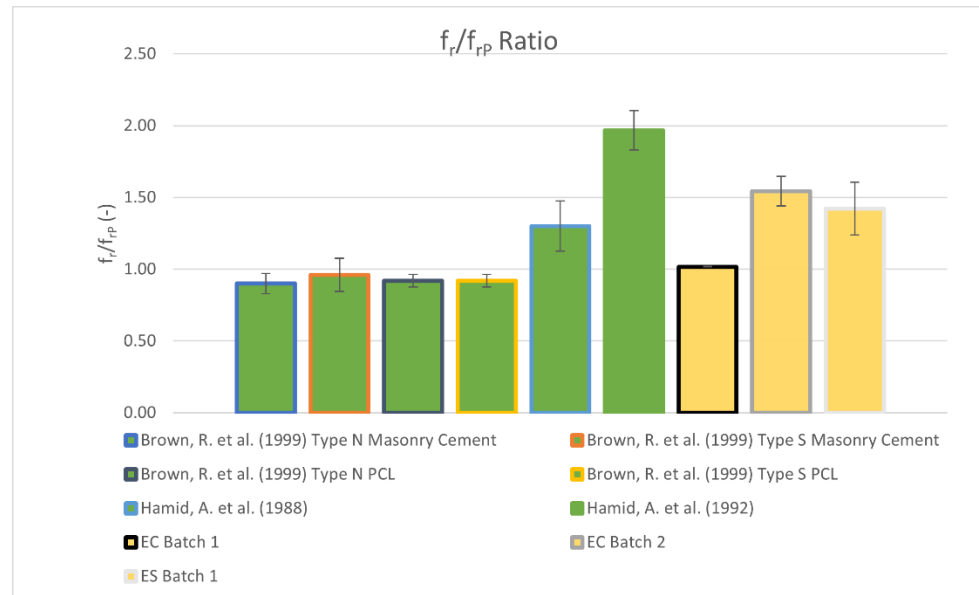


Figure 5.12: $\frac{f_r}{f_{rP}}$ NW and LW batch comparison [38]

Effect of Lightweight Grout Density on Flexural Bond Strength

The lambda values and equations from ACI 318-19 [15] are repeated in Table 5.8. The lambda factor presented in ACI 318-19 [15] increases as the density of grout increases.

Table 5.8: Values of λ for lightweight concrete based on equilibrium density from ACI 318-19

$w_c, \text{lb/ft}^3$	λ	
≤ 100	0.75	(a)
$100 < w_c \leq 135$	$0.0075 w_c \leq 1.0$	(b)
> 135	1.0	(c)

To determine if a similar relationship can be established for LW grout, first the equilibrium density of each grout batch was found following the procedure of ASTM C567 [69] and is presented in Table 5.9 along with the average ratio of the tested to predicted flexural bond strength, f_r/f_{rP} . Although reduction factors for flexural tensile strength were not found to be strictly necessary per the previous analysis, reduction factors, ϕ , were proposed to adjust the average f_r/f_{rP} ratio of the EC and ES samples to the be equivalent to the results of the NW specimens with comparable grout compression strength (1.8 from Table 5.7). The formula used to calculate this reduction factor is shown in Equation 3 and the results are also shown in Table 5.9. The strength reduction factor was calculated with the f_r/f_{rP} ratio instead of the $\frac{f_r}{\sqrt{f_g}}$ ratio to assure the most conservative value.

$$\phi = \frac{f_r/f_{rP}}{1.8}$$

Equation Set 3

Finally, the last column of Table 5.9 displays the reduction factors found in Table 19.2.4.1(a) of ACI 318-19 [15] for concrete with the same equilibrium density as the measured grout specimens. The ACI predictions are similar to the lambda values calculated from the test data but are more conservative for the expanded slate samples. Note that in agreement with the ACI 318-19 equations, the proposed reduction factors, ϕ , increase in value with increasing equilibrium density.

Table 5.9: Lightweight Grout Equilibrium Densities

Density Relationship	Equilibrium	Average	Reduction Factor, ϕ	ACI Reduction Factor, λ
	Density	Ratio		
	lb/ft ³	f_r/f_{rP}		
	(kg/m ³)			
Expanded Clay	76.2 (1220)	1.33	0.75	0.75
Expanded Slate	97.2 (1560)	1.42	0.80	0.75

Conclusion

The data of this study indicates that a reduction factor may not be needed for the flexural bond strength of masonry assemblies using LW grout. The tabulated values from TMS 402/602-22 for flexural bond strength of grouted specimens with tension normal to the bed joint were conservative as compared to the capacities measured during the testing (ratios of tested/predicted values all greater than 1). In addition, the ratio of tested to predicted strength, ratio of flexural bond strength to grout compression strength and the

$\frac{f_r}{\sqrt{f_g}}$ were all very comparable between the tested samples prepared with LW grout and values from the literature for assemblies with NW grout and comparable grout compressive strengths. Although reduction factors for flexural tensile strength were not found to be strictly necessary per the analysis in the comparison of test data to assemblies with normal-weight grout section, reduction factors were proposed to adjust the average f_r/f_{rp} ratio of the EC and ES samples to be equivalent to the results of the NW specimens with comparable grout compression strength. The proposed reduction factors have a similar relationship with equilibrium density and are in a comparable range with the lambda factor presented in ACI 318-19 [15]. Future work could expand this dataset to include other types of LW grouts (expanded shale, etc.) and mortar types.

Acknowledgements

This project builds upon research funded under grant 2019.001 from the National Concrete Masonry Association, and Expanded Shale, Clay, and Slate Institute. The authors would like to acknowledge donations of materials from General Shale, Arcosa Lightweight, and Stalite. Additionally, the team would like to thank undergraduate researcher Dylan Smith for assisting with the testing.

CHAPTER SIX

COST BENEFITS OF LIGHTWEIGHT GROUT

Statement of Contribution

The following work presented is the sole effort of Cooper Banks, and Dr. Laura Redmond.

Introduction

Previous works in the literature have proposed possible reduction factors for design of masonry assemblies with lightweight grout with respect to reduced capacity for diagonal tension strength [7], flexural bond strength [38], anchorage [10], lap splice behavior [7], and shear strength under normal compression loads. However, there has been no studies comparing the potential cost benefits LW masonry designs with the reduction factors applied as compared to NW designs. This study aims to determine if a cost benefit can be found by comparing material cost of NW and LW designs for a fully grouted ordinary reinforced masonry shear wall made of 8-inch-thick nominal units with different seismic design categories, slenderness ratios, and heights subjected to in-pane loading.

Wall Design Procedure

Overview

The design example chosen for this study is based off example 12.4-9 in the Masonry Design Guide (MDG) [70]. The MDG example follow the provisions provided

in TMS 402/602-22 chapter 7 and 9 [59] Figure 6.1 shows the generalized geometry of the ordinary shear wall where; n is the number of stories and SR is the slenderness ratio of the total wall. The height of each story is set at 15 feet for each design. TMS 402/602 [59] does not permit ordinary reinforced masonry shear walls in seismic design category (SDC) D per Table CC-7.3.2-1, so this study will be limited to comparing designs in SDC B and C. Designs in this study are considered at 5, 10, and 15 stories and Slenderness ratios of 1.5, 3, and 4.5. The designs are redone assuming and NW and LW block were used for construction. In total 72 designs are considered. The detailed calculations can be found in Appendix A.

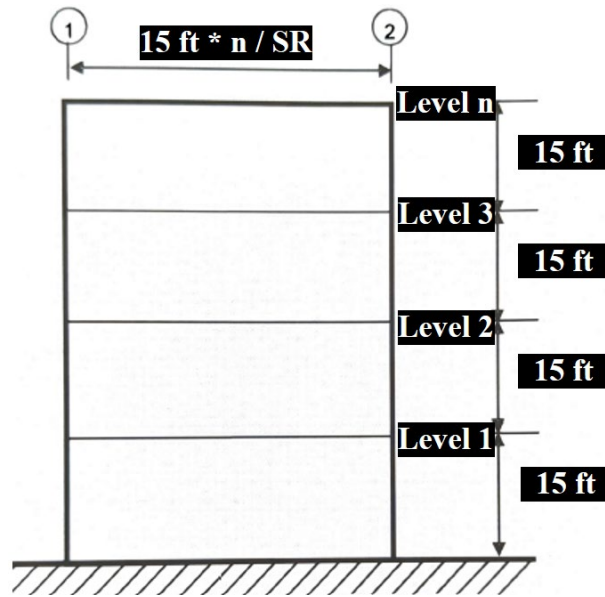


Figure 6.1: General Shear Wall Design Dimensions

Material Properties and Design Parameters

The ordinary reinforced masonry shear walls are designed with 8-inch-thick nominal concrete masonry units with type S Portland cement/lime mortar. The wall is

fully grouted with NW grout, having a density of 140 lbf/ft^3 , and is redesigned with LW having a density of 75 lbf/ft^3 , which is a reasonable assumption given the tested density range of 76.2 lbf/ft^3 to 97.2 lbf/ft^3 from Banks et. al. [38]. The wall is also design using LW block and NW block. The short-period response acceleration parameter, S_{DS} , is selected as 0.25 for SDC B and 0.49 for SDC C. This ensures that S_{DS} is within the ranges for SDC B and C provided in table 11.6-1 in ASCE 7-22 [71]. Each story is 15 ft high, and the number of stories designed are 5, 10, 15. The slenderness ratios designed for are 1.5, 3, and 4.5. Table 6.1 shows the design values for a single grout type, block type, and SDC. The design value shown in Table 6.1 are repeated for each combination of grout type and SDC.

Table 6.1: Design values for a single grout type and SDC

Grout Type: NW or LW Block Type: NW or LW SDC: B or C	n, Number of Stories, -		
SR, Slenderness Ratio, -	n=5	n=10	n=15
	SR=1.5	SR=1.5	SR=1.5
	n=5	n=10	n=15
	SR=3	SR=3	SR=3
	n=5	n=10	n=15
	SR=4.5	SR=4.5	SR=4.5

Loads

The superimposed dead loads and live loads are arbitrarily selected to match the MDG example. Each level below the roof has a superimposed deadload of 40 kips and a live load of 36 kips. The roof level has a superimposed deadload of 30 kips and a live load of 15 kips. The dead load of the wall is added to each level based on a linear interpolation of wall psf found in NCMA TEK 14-13B [72] based on the grout densities. The wall psf load is linearly extrapolated for the LW design. The resulting wall loads per square foot using LW block are 73 psf and 52 psf for the NW and LW grout designs, respectively. The resulting wall loads per square foot using NW block are 84 psf and 62 psf for the NW and LW grout designs, respectively. The in-plane lateral loads are calculated according to the equivalent lateral force procedure presented in section 12.8 of ASCE 7-22 [71]. This is a fictitious design, so the following assumptions are made to simplify the design.

- Assume the seismic response coefficient, C_s , does not exceed $\frac{S_{D1}}{T_a^* \frac{R}{I_e}}$
- Assume T_L is greater than T_a
- Assume S_1 is less than 0.6g

Reduction Factor

The reduction factor applied to the LW grout designs is assumed based on the shear reduction factors presented by Kessler and the grout densities of similar mixes used by Banks, et. al. [38]. Figure 6.2: Proposed Design Reduction Factors for TMS 402/602

shows the proposed reduction factor for TMS 402/602 compared to the reduction factors proposed by Kessler, and Banks, et. al. [38] along with the reduction factor currently used in ACI 318 [15]. The equation for the reduction factor equations for the proposed TMS factor and ACI 318's factor are shown in Table 6.2. Note that the density of the grout mixes used by Kessler were not recorded, the grout densities are assumed to be the same as those measured by Banks, et. al.

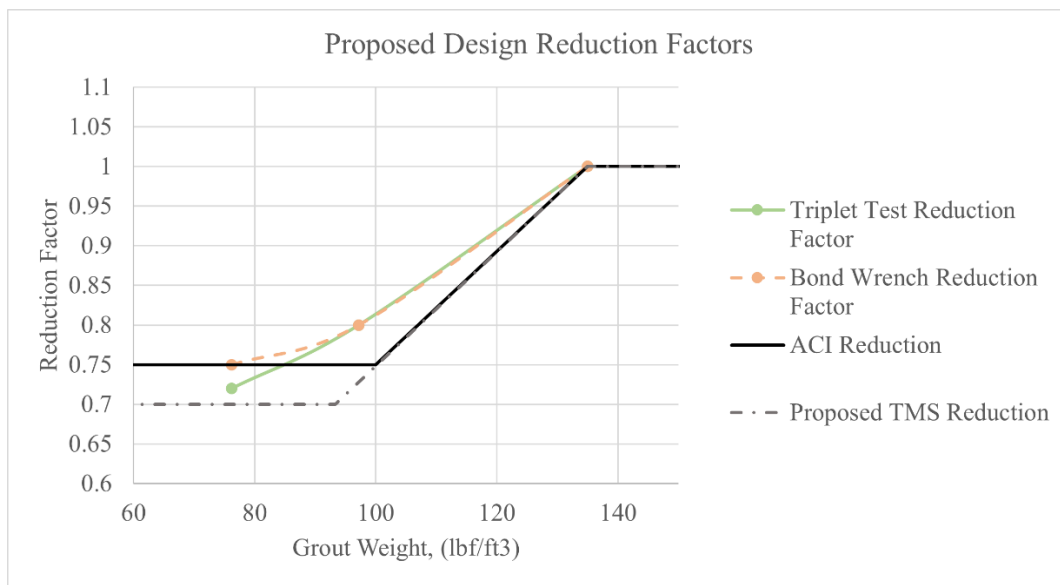


Figure 6.2: Proposed Design Reduction Factors for TMS 402/602

Table 6.2: Reduction Factor Equations

$w_c, \text{lb/ft}^3$	λ [15]	$w_c, \text{lb/ft}^3$	Proposed, ϕ_w
≤ 100	0.75	≤ 100	0.7
$100 < w_c \leq 135$	$0.0075 w_c \leq 1.0$	$93.33 < w_c \leq 135$	$0.0075 w_c \leq 1.0$
> 135	1.0	> 135	1.0

The reduction factor for LW grout was only applied in instances where the nominal shear strength and shear friction was directly affected by the properties of the grout and not applied to the portion of the equations related to the shear capacity of the

rebar. This is consistent with the application of the reduction factor in ACI 318 section 11.5.

Rebar Selection

The rebar is selected to have a minimum cost of rebar while still having adequate design capacity.

Cost Estimation Procedure

The material cost of grout in a completed design is calculated from the total volume of grout to fill every grout core in the systems times by the cost per cubic yard of NW concrete, provided by a local supplier, or the cost of LW concrete, provided by one of the suppliers of the LW aggregates used in the previous works of Shrestha, Kessler, Banks et. al. [7, 38]. The material cost of rebar in a complete design is calculated based on the total LF of different type of rebar present in the design. Note that the cost of block and mortar are the same between and NW and LW design so that cost is neglected in this study. The cost of labor, transportation of material, and additional rebar require for splice length is also neglected in this study. The potential cost savings using lightweight grout of smaller foundations and thermal efficiency of the structure are not discussed in this work.

Results

Out of the 36 designs where the material cost of the NW grouted wall is compared to the LW grouted wall only two displayed an outright cost benefit of 5.4% and 18.5%

percent difference to the NW design. Three of the NW designs could not meet the maximum reinforcement ratio, but the normal weight designs were adequate. Most of the designs had very similar rebar schemes used, the only difference in price was the increased expense of the LW grout. The results of each design are outlined in Figure 6.3 and Figure 6.4.

	Same design between NW and LW
	LW has less rebar but NW costs less
	LW can be designed, but NW cannot be designed
	LW design is cheaper
	NW and LW cannot be designed

SDC: B	n, Number of Stories, -		
SR, Slenderness Ratio, -	n=5	n=10	n=15
	SR=1.5	SR=1.5	SR=1.5
	n=5	n=10	n=15
	SR=3	SR=3	SR=3
	n=5	n=10	n=15
	SR=4.5	SR=4.5	SR=4.5

SDC: C			
SR, Slenderness Ratio, -	n=5	n=10	n=15
	SR=1.5	SR=1.5	SR=1.5
	n=5	n=10	n=15
	SR=3	SR=3	SR=3
	n=5	n=10	n=15
	SR=4.5	SR=4.5	SR=4.5

Figure 6.3: Light weight block design outcomes

SDC: B	n, Number of Stories, -		
SR, Slenderness Ratio, -	n=5	n=10	n=15
	SR=1.5	SR=1.5	SR=1.5
	n=5	n=10	n=15
	SR=3	SR=3	SR=3
	n=5	n=10	n=15
	SR=4.5	SR=4.5	SR=4.5
SDC: C			
SR, Slenderness Ratio, -	n=5	n=10	n=15
	SR=1.5	SR=1.5	SR=1.5
	n=5	n=10	n=15
	SR=3	SR=3	SR=3
	n=5	n=10	n=15
	SR=4.5	SR=4.5	SR=4.5

Figure 6.4: Normal weight block design outcomes

Conclusion

As displayed LW can save a considerable amount in the cost of materials in structures in high seismic zone that require slender and tall lateral force resisting systems.

CHAPTER SEVEN

SUMMARY AND CONCLUSIONS

This work validated the use of the commercially available software ATENA in conjunction with the meshing scheme proposed by Lotfi and Shing [26] later updated by Stravridis and Shing [27] for modeling the pre-peak and peak behavior of masonry models.

Using the validated modeling method. This work confirms proposed shear strength reduction factors found by Kessler through finite element analysis of the triplet tests and an analytical investigation of the failure modes.

The work described also tested the flexural bond strength of an additional LW grout mix made from ES aggregates and compared the reduction in flexural strength to NW assemblies found in literature. This work also expands on the previously proposed reduction factor for the EC mix flexural bond strength by calculating the equilibrium density of the EC and ES mixes and comparing the reduction factors to those presented in ACI 318 [15].

Using the validated and proposed reduction factors, this work demonstrated design examples where the use of LW grout would lead to significant cost savings as compared to designs with NW grout.

Future work includes:

- Additional design comparisons to further display the possible cost savings of LW grouted masonry systems. This includes: a large range of selected variable for the

displayed design, special reinforced masonry shear walls, out-of-plane lateral load designs, and multistory coupled walls using the limit design method.

- Additional shear triplet testing. The shear triplet tests exhibited significant variability. To provide an accurate reduction factor, cohesion, and friction angle approximations more samples should be tested at a wider range of normal compression stresses.
- Creation of an interface element that is better suited for the range of friction angles and cohesion values found by Kessler.
- Redesign of the flexural bond wrench device presented in Chapter 5 for ease of sample assembly or a study to determine if third point bending test can accurately model the flexural bond strength perpendicular to the bed joint in high strength fully grouted masonry assemblies.

Overall, it is recommended that a reduction factor is applied to design for LW grout to reduce the flexural bond and shear strengths. Even with this reduction in strength, design examples have shown that there is a possible material cost benefit to be taken advantage of given adequate provisions in TMS 402/602 can be developed.

REFERENCES

1. Clarke, J. L. *Structural Lightweight Aggregate Concrete* (1st ed.). CRC Press, 1993. (Silva, 2015)
2. Silva, Alexandre Daniel Antunes Almeida da. “Thermal Insulation Characteristics of Structural Lightweight and Normal Weight Concretes Produced with Different Types of Aggregates.” 2015.
3. Roufeal, G., Beaucour, A., Eslami, J., Hoxha, D., Noumowé, A., “Influence of lightweight aggregates on the physical properties of concrete subjected to high temperatures,” *Construction and Building Materials*, 268, 2021.
4. Ma, Xianwei, et al. “A Review on the Use of LWA as an Internal Curing Agent of High Performance Cement-Based Materials.” *Construction and Building Materials*, vol. 218, 2019, pp. 385–393., <https://doi.org/10.1016/j.conbuildmat.2019.05.126>.
5. Tanner, A. “Strength of Masonry Grout Made with Expanded Shale.” MS Thesis, Brigham Young University, USA, 2014.
6. Polanco, H. J. “Structural Lightweight Grout Mixture Design.” MS Thesis. Brigham Young University, USA. 2017.
7. Shrestha, R., Redmond, L., and Thompson, J., “Diagonal Tensile Strength and Lap Splice Behavior of Concrete Masonry Assemblies with Lightweight Grout,” *Construction and Building Materials*, 344, 2022.
8. Petty, P. B. and Nelson, M. R. “Structural Lightweight Masonry Grout.” Proc., 11th North American Masonry Conference, Minneapolis, USA, 2011.
9. Bane, D. K. “Material and Structural Properties of Lightweight Masonry Grout.” *Tennessee Technological University*, 2016.
10. Shrestha, R., Kessler, H., Redmond, L, and Rangaraju, P., “Behavior of Anchor Bolts in Concrete Masonry with Lightweight Grout,” *The ACI Materials Journal* (Published online, awaiting print), 2022.
11. Hiner, B. “Flexural Bond Strength of Masonry Assemblies with Lightweight Grout” *Clemson University*, 2022.
12. Shafigh, P., et al. “A comparison study of the fresh and hardened properties of normal weight and lightweight aggregate concretes.” *Journal of Building Engineering*, vol. 15, 2018, p. 252-260.

13. Nawaz, W., et al. "Experimental study on the shear strength of reinforced concrete beams cast with lava lightweight aggregates." *Archives of Civil and Mechanical Engineering*, vol. 19, No. 4, 2019, p. 981-996.
14. Bogas, J., Gomes, M., Real, S., "Bonding of steel reinforcement in structural expanded clay lightweight aggregate concrete: The influence of failure mechanism and concrete composition." *Construction and Building Materials*, vol. 65, 2014, p. 350-359.
15. *Building Code Requirements for Structural Concrete (ACI 318-19) and Commentary*, American Concrete Institute (ACI), Farmington Hills, MI, 2019.
16. Nahhab, A., Ketab, A., "Influence of content and maximum size of light expanded clay aggregate on the fresh, strength, and durability properties of self-compacting lightweight concrete reinforced with micro steel fibers," *Construction and Building Materials*, 233, 2020.
17. Wan, D., Aslani, F., Ma, G., "Lightweight Self-Compacting Concrete Incorporating Perlite, Scoria, and Polystyrene Aggregates," *Journal of Materials in Civil Engineering*, Vol. 30, Issue 8, 2018.
18. Elango, K., Vivek, D., Anandaraj, S., Saravanakumar, R., Sanfeer, J., Saravanaganesh, S., "Experimental study on self compacting concrete using light weight aggregate," *materialstoday: proceedings*, Vol. 60, Part 3, 2022, pp. 1362-1366.
19. Kumar, P., Pasla, D., Saravanan, J., "Self-compacting lightweight aggregate concrete and its properties: A review," *Construction and Building Materials*, 375, 2023.
20. C476-20 Standard Specification for Grout for Masonry, ASTM International, West Conshohocken, PA, 2020.
21. C39/C39M-21 Standard Test Method for Compressive Strength of Cylindrical Concrete Specimens, ASTM International, West Conshohocken, PA, 2021.
22. E518/E518M-18 Standard Test Methods for Flexural Bond Strength of Masonry, ASTM International, West Conshohocken, PA, 2018.
23. C469/C469M-22 Standard Test Method for Static Modulus of Elasticity and Poisson's Ratio of Concrete in Compression, ASTM International, West Conshohocken, PA, 2022.
24. C496/C496M-17 Standard Test Method for Splitting Tensile Strength of Cylindrical Concrete Specimens, ASTM International, West Conshohocken, PA, 2017.

25. Henderson, C., Mohr, B., Bennett, R., Rikili, D., Thompson, J., “Comparing Strength and Modulus of Elasticity Values for Prisms Constructed with Lightweight and Normal weight Grout,” *Journal of Materials in Civil Engineering*, 2023.
26. Lotfi and Shing (1991). Lotfi, H., and Shing, B. “Appraisal of Smeared Crack Models for Masonry Shear Wall Analysis” *Computers and Structures*, 41(3), 413-425. 1991.
27. Stravridis, A., and Shing, B. “Finite-Element Modeling of Nonlinear Behavior of Masonry-Infilled RC Frames” *Journal of Structural Engineering*, 136(3), 285-296. 2010.
28. Redmond, L. “Seismic Performance, Analysis, and Design of Hybrid Concrete-Masonry” Georgia Institute of Technology, 2015.
29. ATENA. “ATENA Program Documentation Part 1” CERVENKA CONSULTING, 2022.
30. KUPFER, H., HILSDORF, H.K., RUSCH, H. “Behavior of Concrete Under Biaxial Stress” *ACI Journal*, Proc. V.66, No. 8, Aug., 656-666.
31. HORDIJK, D.A. “Local Approach to Fatigue of Concrete” Delft University of Technology, 1991.
32. Bazant, Z.P., and OH, B.H. “Crack Band Theory for Fracture of Concrete” *Materials and Structures*, RILEM, Vol. 16, 155-177.
33. Papadrakakis, M., Papadopoulos, V., Georgioudakis, M., Hofstetter, G., and Feist, C., “Reliability Analysis of Plain Concrete Beam” IALAB Project Report, Austria.
34. ATENA HELP. “Personal communication with ATENA Help”, 2023.
35. Hillerborg, A. “Concrete Fracture Energy Tests Performed by 9 Laboratories According to a Draft RILEM Recommendation” Report to RILEM. Lund University. Sweden.
36. Bazant, Z.P., and Becq-Giraudon, E. “Statistical Prediction of Fracture Parameters of Concrete and Implications for Choice of Testing Standard” *Cement and Concrete Research*, 32, 529-556.
37. C1019-19 Standard Test Method for Sampling and Testing Grout for Masonry, ASTM International, West Conshohocken, PA, 2019.

38. Banks, C.; Redmond, L.; Hiner, B.; Wright, S.; Stoner, M.; “Flexural Bond Strength of Masonry Assemblies with Lightweight Grout”, *The Masonry Society Journal*, Vol. 41, No. 1, pp. 21-38, The Masonry Society, Longmont, CO, 2023.
39. Amadei, B., Strure, S., and Saeb, S. “An Evaluation of Masonry Joint Shear Strength in Existing Buildings” Report for the National Science Foundation. University of Colorado at Boulder. Boulder, CO. 1989.
40. Manzuri, T. “Nonlinear Finite Element Analysis and Experimental Evaluation of Retrofitting Techniques for Unreinforced Masonry Structures” PhD dissertation, University of Colorado Boulder. Boulder, CO. 1995.
41. Mehrabi, A. “Performance of Masonry-Infilled RC Frames Under In-Plane Lateral Loads” PhD dissertation, University of Colorado Boulder. Boulder, CO. 1994.
42. “DIN EN 1052-3: Methods for Test of Masonry - Part 3: Determination of Initial Shear Strength.”
43. Bazant, Z.P. “Mechanics of Distributed Cracking” *Applied Mechanics Rev*, 39(5), 1986.
44. Cheema, T., and Klinger, R. “Compressive Strength of Concrete Masonry Prisms” *ACI Journal*, Jan.-Feb., 88-97.
45. Drysdale, R., Hamid, A., and Baker, L. *Masonry Structures Behavior and Design*. Prentice Hall. Eaglewood Cliffs, New Jersey. 1994.
46. NCMA “TEK 14-7A Allowable Stress Design of Concrete Masonry” National Concrete Masonry Association. 2004.
47. Lotfi, H., and Shing, B. “Interface Model Applied to Fracture of Masonry Structures” *Journal of Structural Engineering*, 120(1), 63-80. 1994.
48. Lourenco, P. B. “Computational strategies for Masonry Structures” PhD dissertation, Delft University, Delft, The Netherlands. 1996.
49. Mojsilovic, N., and Marti, P. “Strength of Masonry Subjected to Combined Actions” *ACI Structural Journal*, 94(57), 633-641. 1997.
50. Schlegel, R., and Rautenstrauch, K., “Failure Analysis of Masonry Shear Walls” 1st International UDEC/3DEC Symposium on Numerical Modeling of Discrete Materials in Geotechnical Engineering, Civil Engineering, and Earth Science, Bochum, Germany. 2004.

51. Shrestha, Rumi. "Development of Lambda Factors for Masonry Design with Lightweight Grout." Clemson University, 2021.
52. Hamid, A., Dysdale, R., and Heidebrecht, A. "Shear Strength of Concrete Masonry Joints" *ACI Journal of the Structural Division*, 105(7), 1227-1240. 1979.
53. Redmond, Laura, Lawrence Kahn, and Reginald DesRoches. "Shear and Tensile Strength Equations for Analysis of Grouted Masonry." *The Masonry Society Journal* 34.1 (2016): 29–38.
54. Shrestha, Rumi, Laura Redmond, Jason J. Thompson, and Prasad Rangaraju "Investigation of Mix Designs for Lightweight Grout per ASTM C476.", *The Masonry Society Journal*, Vol. 40, No. 1, pp. 1-7, The Masonry Society, Longmont, CO, 2022.
55. Redmond, L., Kahn, L., and DesRoches, R. "Design and construction of hybrid concrete-masonry structures informed by cyclic tests," *Earthquake Spectra*, 32(4), 2016b.
56. Redmond, L., Stavridis, A., Kahn, L., and DesRoches, R. "Finite element modeling of hybrid concrete-masonry frames subjected to in-plane loads," *ASCE Journal of Structural Engineering*, 144(1), 2018.
57. Zhu, Jianyixian, Ahmed Ahmed, George Iskander, Nigel Shrive. "Size Effect on Concrete Masonry Shear Strength Under Various Grouting and Precompression Conditions" *14th North American Masonry Conference*. Omaha, 2023.
58. Montazerolghaem, Mahdi, and Wolfram Jäger. "A Comparative Numerical Evaluation of Masonry Initial Shear Test Methods and Modifications Proposed for EN 1052-3." *9th International Masonry Conference*. Guimarães, 2014.
59. TMS 402/602-16 (2016). TMS 402/602-22, "Building Code Requirements and Specification for Masonry Structures.", *The Masonry Society*, Longmont, CO, USA, 2022.
60. Brown, R. et al. (1999). Brown, R., Melander, J., "Flexural Bond Strength of Unreinforced Grouted Masonry Using PCL and MC Mortars." *Proc., 8th North American Masonry Conference*, Texas, USA, 1999.
61. Hamid, A., Dysdale, R., "Flexural Tensile Strength of Concrete Block Masonry." *J. Struc. Eng.*, ASCE, vol. 114, No. 1, 1988, p. 50-66.

62. Hamid, A., Chandrakeerthy, S., Elnawawy, O., “Flexural Tensile Strength of Partially Grouted Concrete Masonry” *J. Struc. Eng.*, ASCE, vol. 118, No. 12, 1992, p. 3377-3392.
63. Wood, S., “Flexural Bond Strength of Clay Brick Masonry”, *The Masonry Society Journal*, Vol. 13, No. 2, pp. 45-55. Longmont, CO, USA, 1995.
64. C90-22 Standard Specification for Loadbearing Concrete Masonry Units, ASTM International, West Conshohocken, PA, 2022.
65. C330/330M-17a Standard Specification for Lightweight Aggregates for Structural Concrete, ASTM International, West Conshohocken, PA, 2017.
66. C404-18 Standard Specification for Aggregates for Masonry Grout, ASTM International, West Conshohocken, PA, 2018.
67. C127-15 Standard Test Method for Relative Density (Specific Gravity) and Absorption of Coarse Aggregate, ASTM International, West Conshohocken, PA, 2015.
68. C128-15 Standard Test Method for Relative Density (Specific Gravity) and Absorption of Fine Aggregate, ASTM International, West Conshohocken, PA, 2015.
69. C567/C567M-19 Standard Test Methods for Determining Density of Structural Lightweight Concrete, ASTM International, West Conshohocken, PA, 2019.
70. Bennet, R. “The Masonry Society’s Masonry Designers’ Guide 2022” *The Masonry Society*, Longmont, CO, USA, 2022.
71. “Minimum Design Loads and Associated Criteria for Buildings and Other Structures” *American Society of Civil Engineers*, Reston, Virginia, USA, 2022.
72. NCMA “TEK 14-13B Concrete Masonry Wall Weights” National Concrete Masonry Association. 2008.

APPENDICES

Appendix A

Cost Comparison Calculations

Strength Design

Fully Grouted, 8 inch thick nominal units, fully grouted, type S Portland cement/lime mortar.
Use ordinary reinforced shear wall.

$$H_S := 15 \text{ ft} \quad n_s := 15 \quad SR := 3 \quad W_w := \frac{n_s \cdot H_S}{24} = 75 \text{ ft}$$

$$S_{DS} := 0.49 \quad \text{SDC: B}$$

$$BT := 1 \quad \text{Block type 0 clay and 1 CMU}$$

$$\gamma_{wg} := 75 \frac{\text{lb}}{\text{ft}^3} \quad \text{Grout density LW (76.2 - 97.2 lb/ft}^3\text{)}$$

Material Properties

$$f'_m := BT = 2000 \text{ psi}$$

$$\phi_w = 0.7$$

$$t_{sp} := BT = 7.625 \text{ in}$$

$$d_v := W_w = 900 \text{ in} \quad d_t := d_v - 4 \text{ in}$$

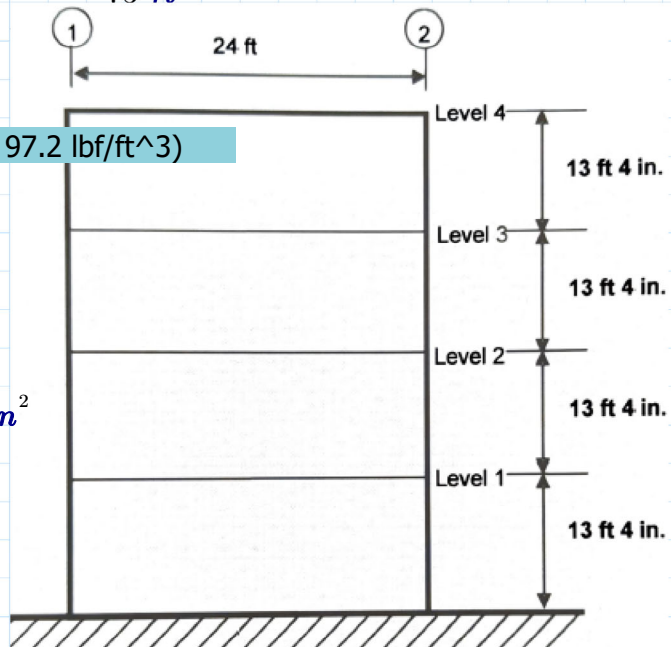
$$\phi := 0.9 \quad A_n := t_{sp} \cdot d_v = 6862.5 \text{ in}^2$$

$$f_y := 60 \text{ ksi} \quad E_s := 29000 \text{ ksi}$$

$$\varepsilon_{mu} := BT = 0.0025$$

$$\varepsilon_{ty} := 0.002$$

$$w_{sw} := w_{sw} (\gamma_{wg}) = 51.1786 \text{ psf}$$



Dead and Live Loads

$$DL_f := 40 \text{ kip}$$

$$DL_r := 30 \text{ kip}$$

$$LL_f := 36 \text{ kip}$$

$$LL_r := 15 \text{ kip}$$

$$DL_s := \begin{cases} \text{for } i \in 0, 1 \dots n_s - 1 \\ \text{if } i < n_s - 1 \\ \quad DL_{s_i} \leftarrow DL_f \\ \text{else} \\ \quad DL_{s_i} \leftarrow DL_r \\ \text{return } DL_s \end{cases} \quad DL_w := \begin{cases} \text{for } i \in 0, 1 \dots n_s - 1 \\ \quad DL_{w_i} \leftarrow w_{sw} \cdot W_w \cdot H_S \\ \text{return } DL_w \end{cases} \quad LL := \begin{cases} \text{for } i \in 0, 1 \dots n_s - 1 \\ \text{if } i < n_s - 1 \\ \quad LL_i \leftarrow LL_f \\ \text{else} \\ \quad LL_i \leftarrow LL_r \\ \text{return } LL \end{cases}$$

Level	Superimposed	Wall weight	Total	Superimposed	Wall weight	Total
(Top of Wall)	40	57.6	97.6	36	57.6	93.6
1	40	57.6	97.6	36	57.6	93.6
	40	57.6	97.6	36	57.6	93.6
	40	57.6	97.6	36	57.6	93.6
	40	57.6	97.6	36	57.6	93.6
$DL_s =$	40	57.6	97.6	36	57.6	93.6
	40	57.6	97.6	36	57.6	93.6
	40	57.6	97.6	36	57.6	93.6
$n_s = 15$	40	57.6	97.6	36	57.6	93.6
	40	57.6	97.6	36	57.6	93.6
	40	57.6	97.6	36	57.6	93.6

EQUIVALENT LATERAL FORCE (per ASCE 7-16 Section 12.8)

12.8.1 Seismic Base Shear

$$V = C_s \cdot W$$

$$S_{DS}$$

(per Section 12.8.1.3)

(per 12.7.2)

$$W := \left(\sum_{i=0}^{n_s-1} DL_{T_i} \right) + 0.25 \left(\sum_{i=0}^{n_s-2} LL_i \right) + 0.25 LL_{n_s-1} = 1583.4 \text{ kip}$$

$$C_s \text{ (per 12.8.1.1)}$$

$$C_s = \max \left(\max (0.044 \cdot S_{DS} \cdot I_e, 0.01), \min \left(\begin{array}{l} \text{if } T_a \leq T_L \\ \left\| C_s \leftarrow \frac{S_{D1}}{T_a \cdot \left(\frac{R}{I_e} \right)} \right\| \\ \text{else} \\ \left\| C_s \leftarrow \frac{S_{D1} \cdot T_L}{T_a^2 \cdot \left(\frac{R}{I_e} \right)} \right\| \end{array} \right), \left(\frac{S_{DS}}{\left(\frac{R}{I_e} \right)} \right) \right)$$

Table 1.5-2 Importance Factors by Risk Category of Buildings and Other Structures for Snow, Ice, and Earthquake Loads

Risk Category from Table 1.5-1	Snow Importance Factor, I_s	Ice Importance Factor—Thickness, I_i	Ice Importance Factor—Wind, I_w	Seismic Importance Factor, I_e
I	0.80	0.80	1.00	1.00
II	1.00	1.00	1.00	1.00
III	1.10	1.15	1.00	1.25
IV	1.20	1.25	1.00	1.50

Note: The component importance factor, I_p , applicable to earthquake loads, is not included in this table because it depends on the importance of the individual component rather than that of the building as a whole, or its occupancy. Refer to Section 13.1.3.

$$R := 2 \quad (\text{per Table 12.2-1})$$

$$I_e := 1.0 \quad (\text{per Section 11.5.1 and Table 1.5-2})$$

$$S_{D1} := 1 \quad (\text{per Section 11.4.5})$$

assume C_s doesn't exceed = $\frac{S_{D1}}{T_a \cdot \left(\frac{R}{I_e} \right)}$

$$T_a = C_t \cdot h_n^x \quad (\text{per equation 12.8-7})$$

$$C_t := 0.02$$

and (per Table 12.8-2)

$$x := 0.75$$

$$h_n := n_s H_S = 225 \text{ ft} \quad (\text{per Section 11.2})$$

$$T_a := C_t \cdot h_n^x \cdot \frac{s}{ft^{\frac{3}{4}}} = 1.162 \text{ s}$$

$$T_L := T_a \cdot 1.1 \quad \text{assume } T_L > T_a \quad \text{assume } S1 \text{ is less than } 0.6g$$

(per Section 11.4.6)

$$C_s := \max \left(\max (0.044 \cdot S_{DS} \cdot I_e, 0.01), \min \left(\frac{S_{D1}}{T_a \cdot \left(\frac{R}{I_e} \right)}, \frac{S_{DS}}{\left(\frac{R}{I_e} \right)} \right) \right) = 0.245$$

$$V := C_s \cdot W = 387.9 \text{ kip}$$

Table 12.2-1 Design Coefficients and Factors for Seismic Force-Resisting Systems

Seismic Force-Resisting System	ASCE 7 Section Where Detailing Requirements Are Specified	Response Modification Coefficient, R^a	Overstrength Factor, Ω^a	Deflection Amplification Factor, C_d^a
A. BEARING WALL SYSTEMS				
1. Special reinforced concrete shear walls ^{a,b}	14.2	5	2½	5
2. Ordinary reinforced concrete shear walls ^c	14.2	4	2½	4
3. Detailed plain concrete shear walls ^d	14.2	2	2½	2
4. Ordinary plain concrete shear walls ^d	14.2	1½	2½	1½
5. Intermediate precast shear walls ^e	14.2	4	2½	4
6. Ordinary precast shear walls ^f	14.2	3	2½	3
7. Special reinforced masonry shear walls	14.4	5	2½	3½
8. Intermediate reinforced masonry shear walls	14.4	3½	2½	2½
9. Ordinary reinforced masonry shear walls	14.4	2	2½	1½
10. Detailed plain masonry shear walls	14.4	2	2½	1½
11. Ordinary plain masonry shear walls	14.4	1½	2½	1½
12. Prestressed masonry shear walls	14.4	1½	2½	1½
13. Ordinary reinforced AAC masonry shear walls	14.4	2	2½	2
14. Ordinary plain AAC masonry shear walls	14.4	1½	2½	1½
15. Light-frame (wood) walls sheathed with wood structural panels rated for shear resistance	14.5	6½	3	4
16. Light-frame (cold-formed steel) walls sheathed with wood structural panels rated for shear resistance or steel sheets	14.1	6½	3	4
17. Light-frame walls with shear panels of all other materials	14.1 and 14.5	2	2½	2
18. Light-frame (cold-formed steel) wall systems using flat strap bracing	14.1	4	2	3½

Table 12.8-2 Values of Approximate Period Parameters C_t and x

Structure Type	C_t	x
Moment-resisting frame systems in which the frames resist 100% of the required seismic force and are not enclosed or adjoined by components that are more rigid and will prevent the frames from deflecting where subjected to seismic forces:		
Steel moment-resisting frames	0.028 (0.0724) ^a	0.8
Concrete moment-resisting frames	0.016 (0.0466) ^a	0.9
Steel eccentrically braced frames in accordance with Table 12.2-1 lines B1 or D1	0.03 (0.0731) ^a	0.75
Steel buckling-restrained braced frames	0.03 (0.0731) ^a	0.75
All other structural systems	0.02 (0.0488) ^a	0.75

^aMetric equivalents are shown in parentheses.

Vertical Distribution of Seismic Forces (per ASCE 7-16 Section 12.8.3)

$$F_x = C_{vx} \cdot V \quad (\text{Per Equation 12.8-11}) \quad C_{vx} = \frac{w_x \cdot h_x^k}{\sum_{i=1}^n w_i \cdot h_i^k} \quad (\text{Per Equation 12.8-12})$$

$k := 1$ (Per Section 12.8.3)

$$C_v := \begin{cases} \text{for } i \in 0, 1 \dots n_s - 1 \\ \quad \text{if } i < n_s - 1 \\ \quad \quad C_{v_i} \leftarrow \frac{(1 \cdot DL_{T_i} + 0.25 LL_i) \cdot ((i+1) \cdot H_S)^k}{\left(\sum_{i=0}^{n_s-2} (1 \cdot DL_{T_i} + 0.25 LL_i) \cdot ((i+1) \cdot H_S)^k \right) + (1 \cdot DL_{T_{n_s-1}} + 0.25 LL_{n_s-1}) \cdot (n_s \cdot H_S)^k} \\ \quad \text{else} \\ \quad \quad C_{v_i} \leftarrow \frac{(1 \cdot DL_{T_i} + 0.25 LL_i) \cdot ((i+1) \cdot H_S)^k}{\left(\sum_{i=0}^{n_s-2} (1 \cdot DL_{T_i} + 0.25 LL_i) \cdot ((i+1) \cdot H_S)^k \right) + (1 \cdot DL_{T_{n_s-1}} + 0.25 LL_{n_s-1}) \cdot (n_s \cdot H_S)^k} \\ \text{return } C_v \end{cases}$$

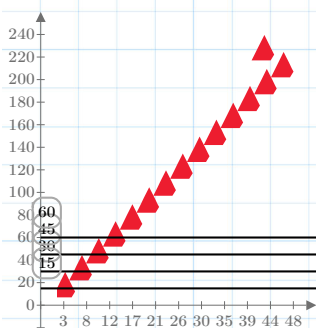
$$F := \begin{cases} \text{for } i \in 0, 1 \dots n_s - 1 \\ \quad F_i \leftarrow C_{v_i} \cdot V \\ \text{return } F \end{cases} \quad V_s := \begin{cases} \text{for } i \in 0, 1 \dots n_s - 1 \\ \quad V_i \leftarrow \sum_{s=i}^{n_s-1} F_s \\ \text{return } V \end{cases} \quad C_v = \begin{bmatrix} 0.01 \\ 0.02 \\ 0.03 \\ 0.03 \\ 0.04 \\ 0.05 \\ 0.06 \\ 0.07 \\ 0.08 \\ 0.08 \\ 0.08 \\ 0.1 \\ \vdots \end{bmatrix} \quad F = \begin{bmatrix} 26.33 \\ 29.62 \\ 32.92 \\ 36.21 \\ 39.5 \\ 338.6 \\ 318.8 \\ 295.8 \\ 269.4 \\ 239.8 \\ 206.9 \\ 170.7 \\ \vdots \end{bmatrix} \text{ kip}$$

Horizontal Distribution of Forces (per ASCE 7-16 Section 12.8.4)

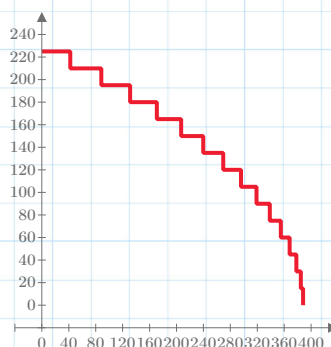
$$V_x = \sum_{i=x}^n F_i \quad (\text{Per equation 12.8-13})$$

$$V_s = \begin{bmatrix} 318.8 \\ 295.8 \\ 269.4 \\ 239.8 \\ 206.9 \\ 170.7 \\ \vdots \end{bmatrix} \text{ kip}$$

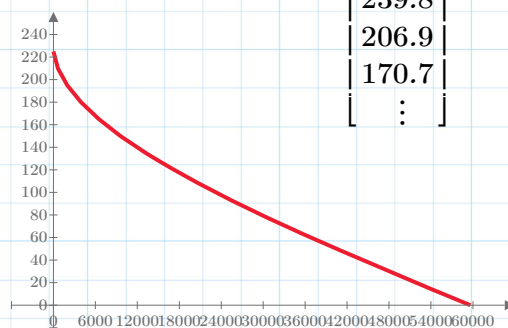
Lateral Loads



Story Shear



Moment



$$V_u := \max(V_g) = 387.9 \text{ kip} \quad M_u := \max(M_g) = 59634.6 \text{ kip} \cdot \text{ft}$$

Loads: (per Chapter 12 page 80 TMS Design Guide)

$$S_{DS} = 0.5$$

$$\rho := 1.0$$

$$D := \sum_{i=0}^{n_s-1} DL_{T_i} = 1453.6 \text{ kip} \quad L := \sum_{i=0}^{n_s-2} LL_i = 504 \text{ kip} \quad L_r := LL_{n_s-1} = 15 \text{ kip} \quad E_v := 0.2 \cdot S_{DS} \cdot D$$

$$E_h := \rho \cdot V_u$$

$$P_1 := 1.2 D + 1.6 L + 0.5 L_r = 2558.3 \text{ kip}$$

$$P_2 := 1.2 D + E_v + 0 \cdot E_h + L = 2390.8 \text{ kip}$$

$$P_3 := 0.9 D - E_v + 0 \cdot E_h = 1165.8 \text{ kip}$$

$$P_{u_a} := \max(P_1, P_2, P_3) \quad P_{u_l} := \min(P_1, P_2, P_3)$$

$$P_u := \text{if } P_1 \neq P_{u_a} \begin{cases} \text{if } P_1 \neq P_{u_l} \\ \text{return } P_1 \end{cases}$$

$$\text{else if } P_2 \neq P_{u_a} \begin{cases} \text{if } P_2 \neq P_{u_l} \\ \text{return } P_2 \end{cases}$$

$$\text{else if } P_3 \neq P_{u_a} \begin{cases} \text{if } P_3 \neq P_{u_l} \\ \text{return } P_3 \end{cases}$$

Check overturning: (per MDG Equations 12.4-42 to 12.4-47)

$$\beta := BT_2 = 2.3$$

$$A := (\beta - 1.0) \cdot 0.36 \cdot f'_m \cdot t_{sp} = 7137 \frac{\text{lbf}}{\text{in}}$$

$$B := 0.36 \cdot f'_m \cdot t_{sp} \cdot d_v - 0.5 \cdot \beta \cdot P_{u_l} = 3600309.3 \text{ lbf}$$

$$C := -M_u = -715615483.9 \text{ lbf} \cdot \text{in}$$

Try No. 4 bars @ 32 in.

$$a := \frac{-B + \sqrt{B^2 - 4 \cdot A \cdot C}}{2 \cdot A} = 152.6 \text{ in}$$

$$A_b := \left(\frac{5}{8} \text{ in} \right)^2 \cdot \frac{\pi}{4} = 0.3 \text{ in}^2 \quad S_s := 16 \text{ in}$$

$$\frac{a}{0.8 \cdot d_t} = 0.213 \leq 0.412 \quad \text{Tension controlled.}$$

$$A_{s_reqd} := \frac{0.8 \cdot f'_m \cdot a \cdot t_{sp} - \frac{P_{u_l}}{\phi}}{f_y \cdot (d_v - \beta \cdot a)} = 0.2063 \frac{\text{in}^2}{\text{ft}}$$

$$A_{s_prov} := \frac{A_b}{S_s} = 0.23 \frac{1}{\text{ft}} \cdot \text{in}^2$$

$$A_{st} := \frac{A_b}{S_s} \cdot W_w = 17.3 \text{ in}^2 \quad n_b := \text{floor} \left(\frac{d_v}{S_s} + 1 \right) = 57$$

Strength Design Interaction Diagram by Spreadsheet Clay Masonry Shear Wall:

Steel Properties

Wall Properties

Reduction Factor

Check Maximum Reinforcement Ratio

$$i := 1, 2 \dots n_b$$

$$b := t_{sp}$$

$$\phi(\varepsilon_t) := \text{if } \varepsilon_t < \varepsilon_{ty}$$

$$d_i(i) := \text{abs} \left((d_t - S_s \cdot (\text{abs}(i - n_b))) \right)$$

$$\parallel 0.65$$

$$\rho_{max} := \frac{0.64 \cdot f'_m}{f_y} \cdot \left(\frac{\varepsilon_{mu}}{\varepsilon_{mu} + 0.005} \right) = 0.$$

$$A_{si} := A_b$$

$$c := 1 \text{ in}, 2 \text{ in} \dots d_v$$

$$\text{else if } \varepsilon_t > \varepsilon_{ty} + 0.003$$

$$\varepsilon_t(c) := \frac{\sum_i^{n_b} \left(\frac{d_i(i) - c}{c} \right)}{n_b} \quad n_b = 57$$

$$\varepsilon_{ty} = 0.002$$

$$\parallel 0.9$$

$$\rho_{max} = 0.007111$$

$$\text{else}$$

$$\parallel 0.65 + 0.25 \cdot \left(\frac{\varepsilon_t - \varepsilon_{ty}}{0.003} \right)$$

$$\rho := \frac{A_{st}}{b \cdot d_t} = 0.00253$$

Compression

Tension

$$a(c) := c \cdot 0.8$$

$$C(c) := 0.8 \cdot f'_m \cdot a(c) \cdot b$$

$$T_i(i, c) := A_{si} \cdot \max \left(\min \left(f_y, E_s \cdot \varepsilon_{mu} \cdot \left(\frac{d_i(i) - c}{c} \right) \right), 0 \text{ ksi} \right)$$

$$M_{nI}(c) := \left(\sum_i^9 \left(T_i(i, c) \cdot \left(d_i(i) - \frac{d_v}{2} \right) \right) \right) + C(c) \cdot \left(\frac{d_v}{2} - \frac{a(c)}{2} \right) \quad P_{nI}(c) := C(c) - \sum_i^9 (T_i(i, c))$$

$$\phi M_{nI}(c) := \phi(\varepsilon_t(c)) \cdot M_{nI}(c)$$

$$\phi P_{nI}(c) := \phi(\varepsilon_t(c)) \cdot P_{nI}(c)$$

Check ductility requirements:

Since this is an ordinary reinforced masonry shear wall, there are no ductility requirements.

Check maximum axial load: $\phi := 0.65$

Radius of gyration, r : $r = \frac{I_n}{A_n} = \frac{t_{sp}}{\sqrt{12}}$ $r := \frac{t_{sp}}{\sqrt{12}} = 2.2 \text{ in}$

Slenderness ratio, h/r : $\frac{H_S}{r} = 81.8$

Nominal Axial Strength, P_n

$$P_n := 0.8 \cdot (0.8 \cdot f'_m \cdot (A_n - A_{st}) + f_y \cdot A_{st}) \cdot \left(\frac{70 \cdot r}{H_S} \right)^2 = 7027.2 \text{ kip}$$

$\phi P_n := \phi \cdot P_n = 4567.7 \text{ kip}$ > Check against factored axial load $P_{u_a} = 2558.3 \text{ kip}$

Check shear: $\phi := 0.8$

$\gamma_g := 1.0$ Reduction factor for partially grouted shear walls, 0.7 if partially grouted

Net shear area, $A_{nv} := t_{sp} \cdot d_v = 6862.5 \text{ in}^2$

Shear span ratio, $\frac{M_u}{V_u \cdot d_v} = 2.05$ Use a value of 1.0 if greater

Maximum design shear: $\phi V_{nmax} := \phi \cdot \left(4 \cdot \frac{A_{nv}}{\text{in}^2} \cdot \sqrt{\frac{f'_m}{\text{psi}}} \right) \cdot \gamma_g \cdot \text{lb}f = 982.1 \text{ kip}$

Nominal masonry shear strength, V_{nm}

$$V_{nm} := \min \left(\left(\left(4 - 1.75 \cdot \left(\min \left(1, \frac{M_u}{V_u \cdot d_v} \right) \right) \right) \cdot \frac{A_{nv}}{\text{in}^2} \cdot \sqrt{\frac{f'_m}{\text{psi}}} \cdot \text{lb}f + 0.25 P_{u_l} \right), \frac{\phi V_{nmax}}{\phi} \right) = 982 \text{ kip}$$

$V_{ns} := 0 \text{ kip}$

[Steel shear capacity]

Design shear strength, $\phi V_n := \phi \cdot (\phi_w \cdot V_{nm} + V_{ns}) \cdot \gamma_g = 549.9 \text{ kip}$

Check design shear versus factored force

$\phi V_n = 549.9 \text{ kip}$ > $V_u = 387.9 \text{ kip}$

No shear reinforcement required

Check shear friction:

$A_{sp} := n_b \cdot A_b$

cross-sectional area of reinforcement within the net shear area

$\frac{M_u}{V_u \cdot d_v} > 1$ $V_{nf} := 0.65 \cdot (0.75 \cdot A_{sp} \cdot f_y + \phi_w \cdot P_{u_l}) = 1042 \text{ kip}$

$\phi V_{nf} := \phi \cdot V_{nf} = 833.6 \text{ kip}$ > $V_u = 387.9 \text{ kip}$ OK!

Perscriptive reinforcement: Recheck

$$Minimum := 0.0007 \cdot b = 0.06405 \frac{\text{in}}{\text{ft}}$$

Perscriptive vertical reinforcement requirements for ordinary shear walls is met with No. 4 @ 36 in. Prescriptive horizontal reinforcement requirements can be met with joint reinforcement of two longitudinal wires of W6.3 (1 gage), spaced not more than 16 in. on center vertically. A bond beam would be required at the top of the wall, with at least 0.2 in.^2 of reinforcement. A No. 4 bar would meet code requirments.

$$A_{sv} := \left(\frac{4 \text{ in}}{16} \right) \cdot \pi \quad S_{sv} := 32 \text{ in} \quad \frac{A_{sv}}{S_{sv}} = 0.074 \frac{\text{in}^2}{\text{ft}} \quad V_{ns} := 0.5 \cdot \left(\frac{A_{sv}}{S_{sv}} \right) \cdot f_y \cdot d_v = 165.7 \text{ kip}$$

Strength Design Interaction Diagram by Spreadsheet Clay Masonry Shear Wall: